FERROELECTRIC THIN AND ULTRATHIN FILMS FOR MEMS APPLICATIONS

A Dissertation
Presented to
The Academic Faculty

By

Yaser Bastani

In Partial Fulfillment
Of the Requirements for the Degree
Doctor of Philosophy in Mechanical Engineering

Georgia Institute of Technology

December 2013

Copyright © Yaser Bastani 2013

Ferroelectric thin and ultrathin films for MEMS applications

Approved by:

Dr. Nazanin Bassiri-Gharb, Advisor
G.W. Woodruff School of Mechanical Engineering
Georgia Institute of Technology

Dr. Levent Degertekin
G.W. Woodruff School of Mechanical Engineering
Georgia Institute of Technology

Dr. Hamid Garmestani
School of Materials Science and Engineering
Georgia Institute of Technology

Dr. Peter Hesketh
G.W. Woodruff School of Mechanical Engineering
Georgia Institute of Technology

Dr. Kenneth Sandhage
School of Materials Science and Engineering
Georgia Institute of Technology

Dr. Todd Sulchek
G.W. Woodruff School of Mechanical Engineering
Georgia Institute of Technology

Date Approved: 10/24/2013

To my mother

and father.

ACKNOWLEDGEMENTS

I would like to thank my adviser Dr. Bassiri-Gharb. Without her continuous support and guidance, I would not have had the opportunity to learn and accomplish my project tasks. For this I am truly thankful. I hope the relationship that we built during my Ph.D. study continue well beyond graduate school.

I would like to extend my appreciation to my committee members: Dr. Garmestani, Dr. Degertekin, Dr. Hesketh, Dr. Sandhage, and Dr. Sulchek for providing valuable research advice and insightful comments for the improvement of this work.

I would also like to thank my past and present lab mates and undergraduate researchers especially Christine Taylor, Asia Wilson and Aida Yougley for their trainings and well-needed help in several parts of this work.

I appreciate all of the kind support provided to me over these years by my parents. Because of them, I am having this journey and I am blessed to enjoy their love and support most of the times. Special thanks go to my dear wife, Sima, whose continuous support encouraged me and occasional help saved me in some hard times during my studies. My appreciation is beyond words to you.

Dear friends, Milad, Arjang, Marmar, Kipp and Sina, I am grateful for your friendship and great times we spent together. I would also like to thank Glenda Johnson and Dr. Wayne Whiteman for their help and support during this time. I am sure I have forgotten many more, I thank you all!

TABLE OF CONTENTS

ACKNOWLEDGEMENTS .... **iii**

LIST OF TABLES .... **viii**

LIST OF FIGURES .... **ix**

NOMENCLATURE .... **xx**

SUMMARY .... **xxv**

Chapter 1: Background and Literature Review .... **.1**
1.1 Piezoelectricity and Ferroelectricity 1
1.2 Poling of Ferroelectric Materials 7
1.3 Intrinsic and Extrinsic Contributions 8
1.4 PZT and PMN-PT Material Systems 13
1.5 Ferroelectric Thin Films for MEMS Applications 17
1.6 Thesis Organization.......................................18

Chapter 2: Experimental Procedures **21**
2.1 Chemical Solution Deposition of Ferroelectric Oxide thin Films 21
2.1.1 Solution Preparation.. 22
2.1.2 Substrate Processing 24
2.1.3 Thin Film Deposition.. 26
2.2 Structural Characterization, X-ray Diffraction 27
2.3 Thickness Measurement.. 30
2.4 Microstructure Characterization 31
2.5 Chemical Characterization: X-ray Photoelectron Spectroscopy....................... 31
2.6 Dielectric Characterization 32
2.7 Piezoelectric Measurements.. 34
2.7.1 Double Beam Laser Interferometry 34
2.7.2 Piezoresponse Force Microscopy (PFM).. .36
2.8 Back-side Etching of the Si Substrate.. 38

Chapter 3: Processing of Highly (100)-Textured PZT Thin Films **41**
3.1 Chemical Solution Deposition.. 41
3.2 Precursor Solution.. 42
3.3 Substrate and Bottom Electrode Stack.. 44
3.4 Processing Conditions: Temperature and Environment 46
3.5 Microstructural Development of PZT Thin Films .... .51
3.5.1 Phase Purity 52
3.5.2 Texture and Crystallographic Orientation of the Films .... .56
3.5.3 Grain Size and Porosity .... .61

3.5.4 Chemical Homogeneity 65

Chapter 4: Effects of the Crystallite Size on the Functional Properties of PZT Ultrathin Films; Thickness Dependence 67
4.1 Introduction 68
4.1.1 Extrinsic Sources of Size Effects 69
4.2 Experimental Procedures 70
4.3 Results and Discussion 71
4.3.1 Film Microstructure and Texture 71
4.3.2 Dielectric and Piezoelectric Characterization 74
4.4 Summary and Conclusions 86

Chapter 5: Effects of Chemical Homogeneity on the Dielectric and Piezoelectric Response of Highly (100)-Textured PZT Thin Films; Superlattice Structure 88
5.1 Introduction 89
5.2 Experimental Procedures 91
5.3 Structural and Chemical Microanalysis 93
5.4 Dielectric and Piezoelectric Characterization 99
5.5 Effects of Stacking Periodicity on the SL Films Properties 106
5.6 Neutron Scattering Study 107
5.7 Conclusions 109

Chapter 6: Alternative Material System: Lead Magnesium Niobate-lead Titanate thin films 111
6.1 Introduction 111
6.2 Experimental Procedures 113
6.3 Results and Discussion 114
6.3.1 Film Microstructure and Texture 114
6.3.2 Dielectric and Piezoelectric Characterization 121
6.4 Summary and Conclusions 130

Chapter 7: Effects of the Substrate Clamping on the Dielectric and Piezoelectric Response of the Ferroelectric Thin Films 131
7.1 Introduction 132
7.2 Experimental Procedures 134
7.3 Results and Discussion; PZT Membranes 134
7.3.1 Macroscopic Dielectric Response 134
7.3.2 Macroscopic Piezoelectric Response 138
7.3.3 Effects of Applied Stress on the Membrane 142
7.3.4 Microscopic Piezoelectric Response 144
7.4 Results and Discussion; PMN-PT Membranes 149
7.5 Summary and Conclusions 150

Chapter 8: Conclusion and Future Work 152
8.1 Summary and Conclusions 152
8.2 Future Work 156

8.2.1 Piezo-MEMS Applications: Integration of Optimized Ferroelectric Thin Films in MEMS Transducers. 156
8.2.2 Supperlattice-like Thin Films; Study of the Effects of Film Thickness and Stacking Periodicit 159
8.2.3 Study of the Effects of Substrate Clamping on Relaxor-Ferroelectric Thin films……... 161

REFERENCES………………………………………………………..………162

LIST OF TABLES

Table 1.1: Piezoelectric and dielectric coefficient of various materials in thin film form 18

Table 2.1: Powder diffraction file numbers used for XRD scan (from ICDD PDF-4 2010) 30

Table 4.1: Thermal processing conditions for the samples characterized in this study.... 71

Table 5.1: Stacking periodicity as a function of solution concentration for SL films spun coated at 3000 rpm........ 93

Table 5.2: Atomic percentages of the constituent elements in the PZT films obtained from XPS quantitative depth profile analysis compared to nominal stoichiometric composition. All values are in (%), and XPS measured values are subject to ±2% instrumentation error. 98

Table 5.3: Low field dielectric permittivity (at 1 kHz, 20 mV_{rms}), reversible (ε'_{init}) and irreversible (α') Rayleigh parameters and their ratio ($\alpha'/\varepsilon'_{init}$) for ~200 nm-thick superlattice (SL), gradient free (GF), and gradient enhanced (GE) PZT films. Low-field dielectric loss values are below 1.7% for all films 100

Table 5.4: Low field dielectric permittivity (at 1 kHz, 20 mV_{rms}), coercive field (E_c), remanent, and maximum polarization (P_r, P_{max}) values measured for ~150 nm-thick superlattice (SL), films with different stacking periodicities. Low-field dielectric loss values are below 1.7% for all films 106

Table 7.1: Low field dielectric permittivity (ε_r @ 20mV_{rms} ,±3%), reversible (±3%) and irreversible (±5%) Rayleigh parameters, P-E ferroelectric hysteresis loop parameters (±5%) and effective piezoelectric coefficient (±10%) of clamped (substrate constrained, Virgin) vs. membrane (Released) PZT capacitors of different thicknesses........ 136

LIST OF FIGURES

Figure 1.1: Schematic illustration of direct and converse piezoelectric effect. 2

Figure 1.2: Schematic representation of the (a) 180° and the (b) non-180° domain wall in a tetragonal ferroelectric material. 5

Figure 1.3: Schematic representation of the (a) polarization-electric field (P-E) and the (b) d_{33}-E_{DC} hysteresis loop of a polycrystalline ferroelectric film. 7

Figure 1.4: (a) Intrinsic response of a single domain under the application of an electric field; (b) extrinsic contribution to the dielectric response via 180° domain wall motion; (c) extrinsic contribution to the dielectric and piezoelectric response via the motion of a non-180° domain wall. The dashed lines represent the configuration before the application of the electric field……………………..8

Figure 1.5: Schematic representation of the AC field dependence of dielectric permittivity in bulk $Pb(Zr,Ti)O_3$ ceramics. The low field region, (I), with relatively constant dielectric permittivity, the Rayleigh region, (II) where the dielectric permittivity increases linearly with the AC field amplitude and the high field region, (III) where a superlinear field-dependence of the dielectric permittivity is observed. 10

Figure 1.6: A schematic illustration of the potential energy landscape for interface (such as domain walls' or phase boundaries') motion with reversible and irreversible effects 12

Figure 1.7: (a) The temperature-composition phase diagram for PZT (b) Zoomed view of the temperature-composition phase diagram for PZT close to the MPB 14

Figure 1.8: (a) The temperature-composition phase diagram for PMN-PT, showing an MPB at 0.33 mole fraction of PT at room temperature. 15

Figure 1.9: Compositional dependence of piezoelectric coefficients of PZT in ceramic compared to theoretical calculation (a) and in thin film form (b). The maximum response is observed on the rhombohedral side of the MPB alon (100) direction. 16

Figure 2.1: Flow chart for preparation of PZT solution as described in Wolf et al. 23

Figure 2.2: Flow chart for preparation of PMN-PT solution as described in Park et al. .. 24

Figure 2.3: XRD pattern of a platinized silicon substrate. 25

Figure 2.4: A representative temperature profile of the rapid thermal anneal processing of the PZT thin films. 27

Figure 2.5: Schematic illustration of Bragg's law of diffraction for crystalline solids 29

Figure 2.6: X'Pert PRO Alpha-1 diffractometer with a CuK_a radiation and θ-2θ goniometer used in this work 29

Figure 2.7: Optical beam path of a typical double-beam laser interferometer. A darker beam color indicates two overlaying Beams. The patterned beam indicates interference of two beams. Lambda plates are used for polarization rotation and the isolator keeps reflected light from re-entering the stabilized beam source. 35

Figure 2.8: PFM setup to simultaneously acquire the topography and the in- and out-of-plane component of the surface displacement. A function generator is used to apply an alternating voltage V_ω between the tip and the bottom electrode of the ferroelectric. The voltage induced cantilever deflection is detected by a reflected laser beam on a four sector photodiode 37

Figure 2.9: BE-PFM setup for conducting piezoresponse measurements where A=response amplitude, Ψ=phase, $\omega_\circ$= resonance frequency, and Q=mechanical quality factor 38

Figure 2.10: Schematic viewgraph of the basic Bosch process…………………………..40

Figure 3.1: Schematic diagram of the free energies of a CSD derived amorphous film and a crystalline perovskite phase. ΔG_v is the thermodynamic driving force for crystallization. 47

Figure 3.2: SEM micrographs of typical thin film microstructures for BT and PZT films prepared by CSD on Si substrate. Top: The BT film displays both interfacial nucleation and nucleation within the bulk of the film, corresponding to a preferred homogeneous nucleation mechanism. Bottom: The PZT film displays only heterogeneous nucleation at the Pt bottom electrode interface (the white surface layer is the Pt top electrode) resulting in columnar grain structure.. 50

Figure 3.3: Secondary pyrochlore phase observed on the surface of a 200nm-thick PZT 53/47 film observed on SEM plain view image. Clustered small grains, mostly decorating the grain boundaries and/or on the film surface, typically of different contrast with respect to the larger perovskite grains represents the pyrochlore 53

Figure 3.4: PbO inclusions in small amounts observable as secondary phase with slightly lighter contrast in the SEM image, accumulated at the grain boundaries between PZT grains 54

Figure 3.5: XRD pattern of a 100 nm thick PZT film with some amount of secondary pyrochlore phase shown as a hump at ~30°. This is caused by insufficient Pb content in the precursor solution (only 10% excess lead was used here) 55

Figure 3.6: Dependence of the piezoelectric response of PZT ceramic and single crystal (Left) and thin films (Right) on the composition and crystallographic orientation 57

Figure 3.7: Effect of Pyrolysis temperature on the texture of PZT thin film prepared on platinized silicon wafer. All films are ~300nm-thick 58

Figure 3.8: Effect of pyrolysis temperature on the orientation of PZT 40/60 films after identical crystallization at 7001C and proposed mechanism(s) behind the texture development 59

Figure 3.9: Effect of crystallization environment on the texture of PZT thin film prepared on platinized silicon wafer. All films are ~300nm-thick and pyrolyzed at 400°C 60

Figure 3.10: Porosity observed between and within the grains in a 1μm thick CSD-derived PMN-PT film 63

Figure 3.11: Annealing temperature profile used for PZT thin films in rapid thermal annealer. Nominal crystallization time and temperature is 1 min and 700°C 64

Figure 3.12: Elimination of most of the porosity in PZT film on platinized Si substrate using the annealing temperature profile in Figure 3.8 65

Figure 4.1: XRD patterns of representative PZT films with different thicknesses in linear x-ray count (top) and logarithmic scale (bottom). Pt(111) peak is from the bottom electrode 73

Figure 4.2: Surface topography of (a) 36 nm, (b) 160 nm, and (c) 260 nm thick PZT films. (d) Cross sectional view of a 260 nm thick PZT film, showing columnar grain microstructure. 74

Figure 4.3: Polarization-electric field hysteresis loops for PZT films, with thicknesses of (a) 30, 37, 48, 62 and 107nm and (b) 107, 119, 161 and 207nm; the loops rotate counterclockwise with increasing thickness in (a) and coercive fields decrease with increasing film thickness in (b). Measurements performed at 1 kHz 75

Figure 4.4: Coercive field values of PZT films as a function of thickness...................... 76

Figure 4.5: Relative permittivity of the films plotted as a function of film thickness at room temperature, measured at 20mVrms and 1kHz 77

Figure 4.6: d/ε as a function of overall film thickness d for series A films .Dashed trendline is fitted to the data for films of d $\geq$60 nm, while the solid line is fitted to the thinner than 50nm films. The two trendlines have the same intercept with vertical axis, but different slopes. This suggests the existence of the same dead layer in all films, while the ferroelectric component has degraded dielectric response in the thinner samples. 79

Figure 4.7: Calculated permittivity of "bulk-like" ferroelectric component, ε_b, based on invariant dead layer characteristics (d_i/ε_i =0.16)... 80

Figure 4.8: Field dependence of the real component of the dielectric permittivity for the PZT films of different thicknesses. 81

Figure 4.9: (Top) Reversible, ε'_{init} and (Middle) irreversible, α' Rayeligh parameters, and (Down) $\alpha'/\varepsilon'_{init}$ ratio as a fuction of film thickness. Data for thicker films (0.27 to 6 μm) are shown from Bassiri-Gharb et. al, and Bintachitt et al. for comparison. 83

Figure 4.10 Effective longitudinal piezoelectric coefficient measured at 1kHz under dc electric bias fields of $2E_c$ 84

Figure 5.1: Schematic representation of the layers configuration for different PZT films used in this work 93

Figure 5.2: XRD patterns of superlattice (SL) and gradient enhanced superlattice (GE) PZT films with different numbers of crystallization steps and stacking periodicity reported for each pattern, along with the XRD pattern of an ideally gradient free (GF) PZT film with 5 crystallization steps, showing no satellite peaks (Top). Detailed views of the SL satellite peaks around {100} and {200} Bragg reflection peaks as a function of stacking periodicity (Bottom) 94

Figure 5.3: Field-emission, scanning electron micrographs of cross section and surface of a 1.2μm thick superlattice PZT film with Λ =60 nm (left and center), showing dense, layer by layer growth of columnar grains in the microatructure. Surface topography of a 190 nm thick (Λ =32 nm) superlattice PZT film (right)....... 96

Figure 5.4: Atomic percentages, as measured by XPS depth profiling of the constituent elements in (a) PZT SL with stacking periodicity, Λ =32 nm (6 annealed layers, 190 nm total thickness), and (b) Zr and Ti atomic percentage variations in SL, gradient enhanced (GE), multiple layer annealed (MLA), and gradient free (GF) PZT films, as a function of normalized etch time.......................... 97

Figure 5.5: schematic representation of tetragonal and rhombohedral crystal lattice 99

Figure 5.6: . Ac electric field dependence of the piezoelectric coefficient for ~200 nm-thick SL and GF films. Capacitors were under constant $2E_c$ bias field during the measurements. 101

Figure 5.7: Polarization-electric field hysteresis loops for ~200 nm-thick SL and GE films 104

Figure 5.8: Comparison of the piezoelectric response of the ~200 nm-thick PZT films with literature reported values for polycrystalline PZT films, with composition close to MPB, deposited on platinized silicon wafers. PZT films from references 16, 17 and 36 are (100)-oriented, those from reference 33 and 34 are (111)- and partly (111)-oriented and those from reference 37 are almost randomly oriented. Reference 35 reports values for both (100)- and (111)-oriented films with (100)-oriented film having higher piezoelectric response at similar film thickness. 105

Figure 5.9: Modeling of the neutron scattering length density in PZT SL thin film. There are six repeating crystallized layers and each one is consisting of three sub layers based on Zr/Ti composition gradient... 108

Figure 5.10: Comparison between the measured neutron reflectivity on the SL PZT thin film and the simulated values based on the model shown in figure 5.9 109

Figure 6.1 XRD patterns of (100)-oriented (a) and (111)-oriented (b), ~600 nm-thick PMN-PT films on both PT and PZT buffer layers compared to the diffraction pattern of a PMN-PT film, deposited without any buffer layer. Asterisk marks represent fluorite peaks in the PMN-PT film with no buffer layer.............. 116

Figure 6.2: FE-SEM surface morphology of 300 nm thick, PMN-PT films, crystallized at (a) 750°C, (b) 800°C, and (c) 800°C with a PbO cover coat on the surface prior to each crystallization step. (d) At higher film thicknesses, >600 nm, cracks and porosity are observed on the surface of the films processed at 800°C. (e) Intra-granular pores formed between grains beyond a critical film thickness (≥600 nm), and (f) inter-granular pores inside the grains are shown in the cross sectional views of the thick PMN-PT films.............................. 118

Figure 6.3: (a) Surface topography of a 600 nm thick, (100)-oriented PMN-PT film, consisting of dome-shaped grains. Slow growing (111) atomic planes surround small top (100) facets of the grains. (b) A 900 nm-thick, (001)-oriented PMN-PT film processed with faster annealing ramp rates (~100°C/s), longer pyrolysis time (3 minutes), crystallization at higher temperature (850°C), and use of PbO cover-coat prior to each crystallization, resulting in elimination of surface porosity. (c) Presence of a lower dwell temperature (700°C) in a multi-ramp annealing temperature profile led to an increase in the film porosity regardless of the 850°C final annealing temperature 119

Figure 6.4: Low-field dielectric permittivity of the PMN-PT films as a function of thickness (Top) for PMN-PT films with thin (30 nm) PT or PZT buffer layers, and (Bottom) for different preferential crystallographic orientation, when processed on thin PT buffer layer. Hollow symbols represent tanδ values, while filled symbols represent the dielectric permittivity. The measurements were carried out at 1 kHz and 20 mV_{rms}. 122

Figure 6.5: Polarization-electric field hysteresis loops for ~900nm-thick PMN-PT films on PT buffer layer, with different textures.................... 123

Figure 6.6: FE-SEM surface topography of the 30 nm-thick, sol-gel deposited (a) $PbTiO_3$, and (b) $Pb(Zr_{0.53}Ti_{0.47})O_3$ films used as seed/buffer layers for PMN-PT films 124

Figure 6.7: Thickness dependence of the coercive field for PMN-PT films on PT buffer layer.................... 125

Figure 6.8: The relative dielectric permittivity (C-V measurements) as well as $d_{33,f}$ piezoelectric coefficient as a function of bias electric fields, for (100) textured films for (a) 900 nm-thick PMN-PT film in, Pt/PZT/PMN-PT/Cr/Au configuration, and (b) 730 nm-thick PMN-PT film in, Pt/PZT/PMN-PT/Pt configuration. Piezoelectric measurements were conducted with $V_{ac} = 0.2V_c$ (coercive voltage) at 1 kHz under dc electric bias field of up to $2E_C$ 126

Figure 6.9: Thickness dependence of the built-in voltage (imprint) in (100)-oriented PMN-PT films on PT buffer layer with symmetric versus asymmetric electrode stack configurations. The values were calculated based on asymmetry in coercive fields in P-E hysteresis loops.................... 127

Figure 6.10: (a) Saturated, and (b) remanent effective d33,f piezoelectric coefficients of the PMN-PT films as a function of thickness and preferential crystallographic orientation of the films.................... 128

Figure 7.1: XRD patterns of (100)-oriented PZT (top) and PMN-PT (bottom) films used to prepare the membranes 135

Figure 7.2: $d_{33,f}$-E_{dc} hysteresis curves and (b): Capacitance-E_{dc} (C-E curve) for a 1 µm-thick PZT capacitor in clamped state (virgin) before Si etching, and after etch in membrane form (released). The inset in (a) shows a zoomed view of the $d_{33,f}$-E_{dc} hysteresis curve of the virgin capacitor.................... 137

Figure 7.3: Field dependence of the real component of the dielectric permittivity for the 1 µm PZT films in virgin and released states. The slope and intercept of the fitted trend line represent the irreversible and reversible Rayleigh parameters 138

Figure 7.4 Variation of the dielectric permittivity (ε_r) and piezoelectric response $d_{33,f}$ as a function of the residual Si thickness 139

Figure 7.5: Ac field amplitude and frequency dependence of the piezoelectric response as measured via double beam laser interferometry. (a): Dependence of the $d_{33,f}$-E_{dc} hysteresis curves on the ac amplitude at 1kHz and (b): Dependence of the $d_{33,f}$-E_{dc} hysteresis curves on the frequency of the ac field at the amplitude of 1V measured on a 900 nm-thick PZT membrane. 141

Figure 7.6: Local characterization of piezoresponse in PZT clamped capacitors when applied to the shown dc bias 145

Figure 7.7: Topography and local characterization of piezoresponse in PZT membrane capacitors (on the Pt top electrode) when applied to the shown dc bias....... 145

Figure 7.8: Proposed avalanche mechanism in specific single domain wide grains (left) compared to jamming and suppression in comlex domain configuration (right). 148

Figure 7.9: (a): $d_{33,f}$-E_{dc} hysteresis curves and (b): Capacitance-E_{dc} (C-E curve) for a 1 µm-thick 0.7PMN-0.3PT capacitor in clamped state (virgin) before Si etching, and after etch in membrane form (released). The inset in (a) shows a zoomed view of the $d_{33,f}$-E_{dc} hysteresis curve of the virgin capacitor. 150

Figure 8.1: Huge enhancement of the piezoelectric response in substrate-released highly (100)-textured PZT thin films compared to the piezoelectric response of some other piezoelectric materials in thin film and single crystal form 156

Figure 8.2: Schematic drawing of generic structures in bending actuators or sensors: (a) and (b) show bending actuation for parallel-plate and interdigitated electrodes, respectively; (c) visualize actuator and sensor modes for cantilevers and bridges, respectively. FE, ferroelectric; E, electric field; P, polarization 157

NOMENCLATURE

A	Area of the electrode
a_0 ,c_0	Lattice parameter, tetragonal
a_R	Lattice parameter, rhombohedral
AC	Alternating current
α_d	Irreversible piezoelectric Rayleigh coefficient
α_ε	Irreversible dielectric Rayleigh coefficient
AFM	Atomic force microscopy
BE-PFM	Band excitation piezoresponse force microscopy
λ	Wavelength of the x-rays
Λ	Stacking periodicity of the superlattice structure
γ	Interfacial energy
θ	Angle of incidence
χ	Dielectric susceptibility
C	Dielectric capacitance
d	Film Thickness
d_{space}	Interplanar spacing of the crystal atoms
d_{ij}	Longitudinal piezoelectric coefficients tensor (reduced format)
$d_{ij,f}$	Effective longitudinal piezoelectric coefficients tensor (reduced format)
D	Dielectric displacement
DC	Direct current
E	Electric field $E=E_o\sin(wt)$

e_{ij}	Transverse piezoelectric coefficients tensor (reduced format)
$e_{ij,f}$	Effective transverse piezoelectric coefficients tensor (reduced format)
ε	Dielectric permittivity
ε'	Real component dielectric permittivity
ε''	Imaginary component dielectric permittivity
E_c	Coercive field
E_d	Depolarizing field
EDS	Energy dispersive x-ray spectroscopy
E_o	Amplitude of AC electric field
ε_o	Permittivity of free-space
ε_r	Relativity permittivity
f	Lotgering Factor
$I_{(hkl)}$	Integrated peak intensity of the XRD patterns related tothe (hkl) planes
MPB	Morphotropic phase boundary
MEMS	Micro-electro-mechanical systems
NEMS	Nano-electro-mechanical systems
P	Dielectric polarization
P_r	Remanent dielectric polarization
Ψ	Piezoresponse phase angle
PFM	Piezoresponse force microscopy
PZT	Lead zirconate titanate
Q	Electromechanical quality factor
R	Rhombohedral phase

RIE	Reactive ion etch
RTP	Rapid thermal processor
s_{ij}	Elastic compliance tensor (reduced format)
σ_{ij}	Mechanical stress tensor (reduced format)
T	Temperature
$\tan\delta$	Dielectric dissipation factor
T_c	Curie temperature
TR	Tetragonal phase
ω	Frequency
x_{ij}	Mechanical strain tensor (reduced format)

SUMMARY

The advent of ferroelectric thin films with strong piezoelectric response has enabled the development of new nano- and micro-electromechanical systems (NEMS/MEMS) capable of large displacements at low voltage levels, aiming to be compatible with complementary metal oxide semiconductor industry. Key to all of these applications is the ability to process ferroelectric materials with maximized electromechanical coupling and to integrate them into the devices. With the continuous drive towards miniaturization of devices for piezoelectric and electronic applications, processing of ultrathin ferroelectric films with maintained large electromechanical coupling is essential to the development of high performance NEMS and MEMS.

The piezoelectric response of ferroelectric thin films is profoundly affected by the texture and microstructural characteristics of the material and is severely reduced at sub-micron thickness ranges. For the first time, reproducible synthesis of dense, highly textured and phase-pure PZT thin films was achieved via chemical solution deposition. The consistent processing of ferroelectric thin films resulted in the elimination of the coupling effects of crystallographic anisotropy, porosity and in general microstructural characteristics on the functional properties of the films. This enabled effective study of the key parameters influencing the electromechanical response of the ferroelectric thin films, such as crystallite size (thickness dependence), chemical heterogeneities and substrate clamping.

Reproducible synthesis of highly (100)-textured PZT ultrathin films enabled the study of the size effects on the dielectric and piezoelectric response of these films in the

thicknesses ranging from 20 up to 260nm. Dielectric and piezoelectric responses of the films monotonically decreased in thinner films. For PZT films at MPB, a critical thickness, ~50nm was observed below which the extrinsic contributions to the dielectric responses of the films are heavily suppressed.

After the study and acknowledgment of the severe reduction of the piezoelectric response in ferroelectric ultrathin film, several factors affecting piezoelectric response of ferroelectric films were studied in order to maximize the response especially at low film thickness ranges: chemical homogeneity, residual stresses and substrate clamping as well as using alternative material systems; relaxor ferroelectrics. In particular, a major part of the piezoelectric (and dielectric) response of the PZT has extrinsic sources such as domain or phase boundary motion and vibrations. Special attention was paid throughout this investigation into understanding extrinsic origins in PZT thin films and different approaches was utilized to further activate and enhance their contributions.

Focusing on the chemical homogeneity of the ferroelectric films, Different routes were used to process ultrathin films (<200nm) with maintained functional properties. Superior piezoelectric properties - 40% higher piezoelectric response than in conventionally processed films - were achieved in highly (100)-oriented PZT superlattice-like films with controlled compositional gradient centered around MPB composition on Si substrates. Superlattice (SL) or heterolayered ferroelectric thin films consist of alternate layers of ferroelectric materials, or phases, with a compositional gradient normal to the substrate. The dynamic motion of “artificially created” phase boundaries between layer to layer tetragonal and rhombohedral phases participated in the extrinsic contributions to the films’ dielectric and piezoelectric response. This approach

led to processing of 200 nm SL films with $d_{33,f}$ values as high as some of the best previously reported data for 1 to 2 µm-thick PZT films.

Furthermore, comprehensive processing optimization was carried out on relaxor-ferroelectric PMN-PT thin films. Dense, highly (100)-textured PMN-PT films were synthesized exhibiting the highest $d_{33,f}$ coefficients reported so far in the literature (210pm/V) for corresponding thickness ranges. Control of the microstructural characteristics - texture and density – throughout the whole film thickness was necessary to obtain films with maximized functional properties.

To study the effect of substrate clamping on the piezoelectric performance of the films, the Si substrate in PZT and PMN-PT films were back-side etched via dry etching in an inductively coupled plasma reactor. This approach is similar the final state of the films for MEMS applications, where the Si substrate is mostly removed in order to have a free-standing or semi-free standing ferroelectric membrane or cantilever. A giant enhancement in the piezoelectric $d_{33,f}$ coefficient of the substrate-released samples was observed with respect to the films on the virgin substrate. The response increased by at least one order of magnitude from ~75-200 pm/V (for different PZT film thicknesses ranging from 300nm to 1µm) to ~1500 to 4500 pm/V at reduced Si thickness. Experimental observations in macroscopic dielectric and piezoelectric characterization and microscopic piezo-response force microscopy of the samples indicate larger extrinsic contributions, -possibly with domain dynamic source- to the functional responses of the films in back-side etched samples. A fundamental change in the pattern of the electromechanical activity of the grains between the released and clamped films was observed in the band-excitation piezo-force microscopy investigations; A breakdown of

the clustered pattern in the electromechanical activity of the grains in the PZT film. This giant enhancement promises a new pathway for greatly improved electromechanical properties which has a huge potential to enable high performance future device applications.

Chapter 1

Background and Literature Review

This chapter aims at giving background information regarding the literature relevant to the current investigation. A discussion of piezoelectric and ferroelectric phenomena and domain formation in ferroelectric materials is followed by the introduction of relevant material systems (lead zirconate-titanate and lead magnesium niobate-lead titanate) examined in this work. Intrinsic and extrinsic sources of the dielectric and piezoelectric response of the ferroelectric materials are discussed. Furthermore, the influential factors on the functional responses of these materials are noted and several approaches used in this study to maximize the piezoelectric coefficient of the material are introduced.

1.1 Piezoelectricity and Ferroelectricity

Piezoelectrics are materials that generate an electrical charge density, D_i in response to an applied stress, σ_{jk} (Eq. 1), and conversely develop a strain, x_{ij} due to an applied electric field, E_k (Eq.2 and Figure 1.1).[1,2] The piezoelectric effect is present in crystal lattices with asymmetric charge surroundings. Among the 32 crystallographic point groups, the piezoelectric effect is absent in all 11 centro-symmetric point groups and in point group 432 where the addition of symmetry elements leads to the absence of piezoelectricity.[3]

The electromechanical relationship between the stimuli and response in piezoelectric materials is described by the piezoelectric tensor, d_{ijk}, or e_{ijk} which is identical for the direct and converse effects due to thermodynamic relations. [1] This is shown in as:

$$D_i = d_{ijk}\sigma_{jk} \quad \text{or} \quad D_i = e_{ijk}x_{jk} \qquad \text{Equation 1.1}$$

$$x_{ij} = d_{kij}E_k \quad \text{or} \quad \sigma_{ij} = e_{kij}E_k \qquad \text{Equation 1.2}$$

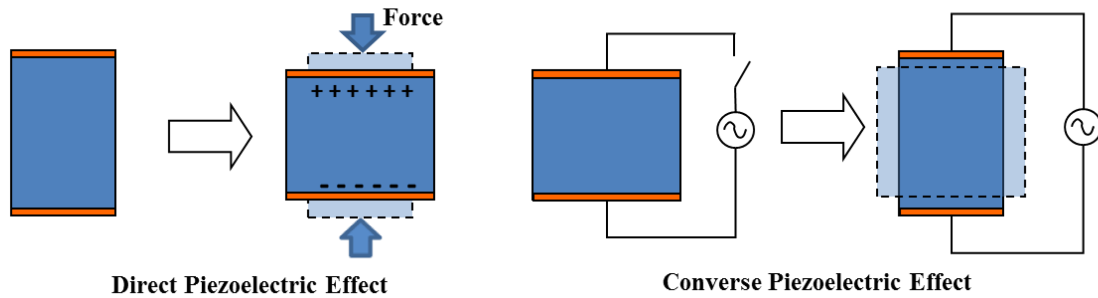

Figure 1.1: Schematic illustration of direct and converse piezoelectric effect.

The same equations can be expressed in reduced notation as:

$$D_i = d_{ij}\sigma_j \quad \text{or} \quad D_i = e_{ij}x_j \qquad \text{Equation 1.3}$$

$$x_i = d_{ij}E_j \quad \text{or} \quad \sigma_i = e_{ij}E_j \qquad \text{Equation 1.4}$$

in which, σ_{ii} and x_{ii} are reduced to σ_i and x_i respectively, and shear stresses, τ_{12}, τ_{13} and τ_{23} are replaced with σ_4, σ_5 and σ_6 (and likewise for strain tensor). For example, for a piezoelectric thin film in parallel plate capacitor configuration where the electric field is applied along the thickness direction, E_3, depending on the strain being characterized along the thickness direction, x_3, or in-plane direction, $x_1 = x_2$, d_{33} or d_{31} are

relevant piezoelectric coefficients, respectively. d_{33} is referred to as the longitudinal piezoelectric coefficient and d_{31} is the transverse piezoelectric coefficient.

The above equations hold for unconstrained piezoelectric materials, and are only valid for small signal excitations. At higher driving (ac) fields the piezoelectric coefficients are no longer constant but rather dependent on the amplitude of the applied electric field[1].

For piezoelectric thin films, the piezoelectric material is in a composite structure, clamped to a substrate which is generally much thicker than the film itself. At the interface along the in-plane directions (indices 1, 2), the piezoelectric thin film and the substrate have identical strains. Perpendicular to the film plane, (in the thickness direction) the thin film is free to move, i.e., $\sigma_3 = 0$. As a consequence, there is no deformation mode in which only one piezoelectric coefficient is involved. The complete equation of state needs to be analyzed.[1] For a thin film clamped to a much thicker substrate, the in-plane strains stay at zero ($x_1 = x_2 = 0$) when an electric field, E_3 is applied. Therefore, in-plane stresses and an out-of-plane strain are developed. The equation of state using the compliance tensor, s_{ij} and piezoelectric coefficients will be (no shear components):

$$\begin{aligned} x_1 &= (s_{11} + s_{12})\sigma_1 + d_{31}E_3 = 0 \\ x_3 &= 2s_{13}\sigma_1 + d_{33}E_3 \end{aligned} \qquad \text{Equation 1.5}$$

The first equation allows evaluation of in-plane stresses, which can be used to obtain the expression for the “effective” piezoelectric coefficients, as defined by:

$$d_{33,f} = \frac{x_3}{E_3} = d_{33} - \frac{2s_{13}}{s_{11}+s_{12}} d_{31}$$
$$e_{31,f} = \frac{\sigma_1}{E_3} = \frac{d_{31}}{s_{11}+s_{12}}$$
Equation 1.6

Effective coefficients can be measured directly depending on the characterization configuration. In this work, $d_{33,f}$ was measured by characterizing the change in the film thickness (x_3) in response to the applied E_3 using double beam laser interferometry. The system is discussed in detail in section 2.7.1.

A sub-category of piezoelectric materials is represented by ferroelectric materials, which possess strong piezoelectric response. A ferroelectric material shows two or more equivalent spontaneous polarization directions for a given temperature range. Additionally, the polarization direction is reorientable between at least two equilibrium states by application of an appropriate electric field of reasonable strength.[4] The material's crystal structure changes from paraelectric cubic into distorted ferroelectric phase below the ferroelectric transition temperature (Curie temperature, T_C). Domains form in this transition to minimize the elastic and electrostatic energy of the system; Domains are volumes of material where the spontaneous polarization direction is nearly uniform.[2] The boundaries between domains are referred to as domain walls, which are named according to the angle formed between the spontaneous polarization directions in adjacent domains, e.g. 180° domain walls are formed between two domains of opposite polarization direction. Similarly, non-180° domain walls refer to the boundary between domains whose polarization directions make a non-180° angle as illustrated in Figure 1.2.

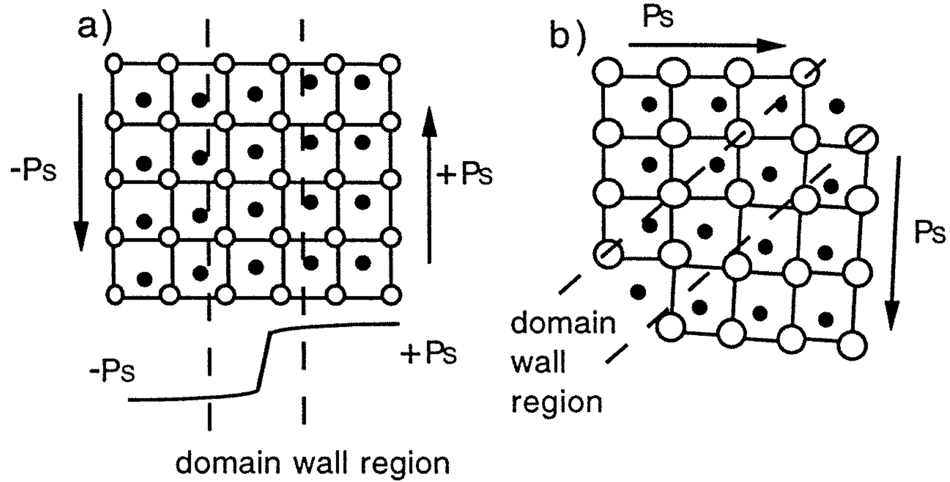

Figure 1.2. Schematic representation of the (a) 180° and the (b) non-180° domain wall in a tetragonal ferroelectric material.[3]

The dielectric susceptibility, χ_{ij}, relates the electrical polarization vector P to the electric field vector E:

$$P_i = \chi_{ij} E_j \quad \text{Equation 1.7}$$

A polarization - electric field (*P-E*) hysteresis loop is the signature feature of ferroelectric materials and represents the nonlinear polarization response to appropriately large AC voltage excitations (Figure 1.3a).[5] This loop exhibits the switching behavior of the collective domains in response to the external electric field. The hysteretic behavior in the loop stems from the nonlinearity associated with the domain nucleation and domain wall motions phenomena. Saturation results from growth and eventually merging of the domains in an ideally single domain final state at appropriately large electric fields.

Starting from the virgin state in a polycrystalline ferroelectric (point O), a small electric field initially leads to a linear increase in the polarization (constant dielectric susceptibility). At higher electric fields, the polarization response becomes nonlinear due to domain walls motion. Further increase in the electric field results in domain switching in order to increase alignment of their spontaneous polarization direction with respect to the applied electric field until saturation occurs (point A). As the field strength is then decreased, some of the domains will switch back but a remanent polarization exists at zero field (point B) which is called "positive remanent polarization" P_r^+. As the electric field is increased in opposite direction, eventually a zero net polarization is achieved (point C) corresponding to negative coercive field ($-E_c$). Larger negative electric fields result in appearance and growth of small nuclei of domains with reverse polarization directions. Eventually these domains merge until saturation is reached with ideally a single domain in the reversed polarization direction (point D). As the negative field is decreased and then increased with opposite polarity, the material undergoes nucleation of new domains with an opposite spontaneous polarization direction. The process continues until the hysteresis loop is completed with another saturation (point A).

The reorientation of the spontaneous polarization with the application of a (DC) bias electric field (E_{DC}) generates a nonlinear hysteretic d_{33}-E_{DC} response known as the "piezoelectric hysteresis" loop (Figure 1.2b).[6] To obtain this loop, a constant ac field is superimposed on a varying bias field, and the piezoelectric response is measured and recorded at each dc bias level.

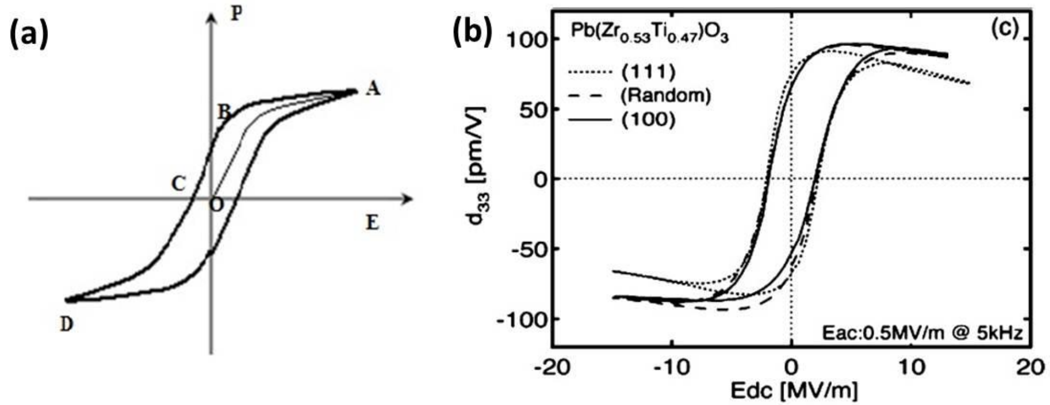

Figure 1.3. Schematic representation of the (a) polarization-electric field (P-E) and the (b) d_{33}-E_{DC} hysteresis loop of a polycrystalline ferroelectric film.[4,7]

1.2 Poling of Ferroelectric Materials

As mentioned before, ferroelectric materials develop domains upon cooling below T_c to minimize the overall energy of the system with respect to the electrostatic and elastic effects. Usually the initial direction of the spontaneous polarization in different domains through the material is random or distributed in such a way as to lead to very small or zero net polarization. In this case, the electromechanical response of individual domains will cancel which results in zero or very small overall piezoelectric response. Application of a strong electric bias field (which depends on the material and its form, thin film, bulk or ceramic, etc), sometimes at elevated temperatures, reorients the polarization direction along the applied field. This process which is called poling, cannot change the crystal structure of the material or orient grains, but can reorient domains within individual grains in the direction of the field. After removal of the field, some part of the material will be again reoriented into more random distribution. However, the

material maintains some remanent polarization. A poled polycrystalline ferroelectric exhibits piezoelectric properties, even if many domain walls are still present.[3]

The effect of poling in the ferroelectric material deteriorates with time (ageing), and when exposed to higher temperatures or strong alternating electric fields (especially greater than coercieve field).

1.3 Intrinsic and Extrinsic Contributions

The dielectric and piezoelectric responses of ferroelectric materials are comprised of both intrinsic and extrinsic components.[7] The intrinsic component is due to the dielectric/piezoelectric response as a direct consequence of the ferroelectric distortion in the unit cell. Accordingly, this is the response obtained from an ideal single domain in the ferroelectric material (Figure 1.4a). Extrinsic contributions include other sources such as that resulting from domain walls' and eventual phase boundaries' motion (Figure 1.4) and realignment of defect dipoles.

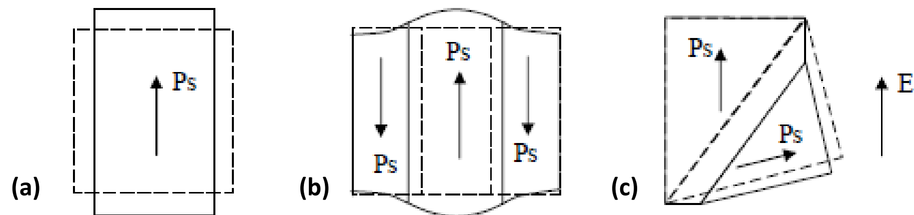

Figure 1.4. (a) Intrinsic response of a single domain under the application of an electric field; (b) extrinsic contribution to the dielectric response via 180° domain wall motion; (c) extrinsic contribution to the dielectric and piezoelectric response via the motion of a non-180° domain wall. The dashed lines represent the configuration before the application of the electric field. [8]

While both 180° and non-180° domain walls contribute to the dielectric and piezoelectric response and are ferroelectrically active, the non-180° domain walls are more strongly ferroelastically active and have major contribution to the piezoelectric response of the material. Analysis in the framework of Rayleigh law - which was originally developed for ferromagnetic materials- is often used to separate and quantify the intrinsic and extrinsic contributions to the dielectric and piezoelectric response of ferroelectrics.[9] Before discussing the Rayleigh analysis, dependence of the dielectric and piezoelectric response on the amplitude of the electric field will be explained.

For materials that show Rayleigh-like behavior, the dependence of the piezoelectric and dielectric response on the ac field can be usually separated in three different regions: a low field region, a Rayleigh region, and a high field region (Figure 1.5). At low AC field amplitudes, the relative dielectric permittivity and piezoelectric coefficient are almost constant, therefore the dielectric permittivity and piezoelectric response increase linearly with electric field amplitude (according to equations 1.8 and 1.9).

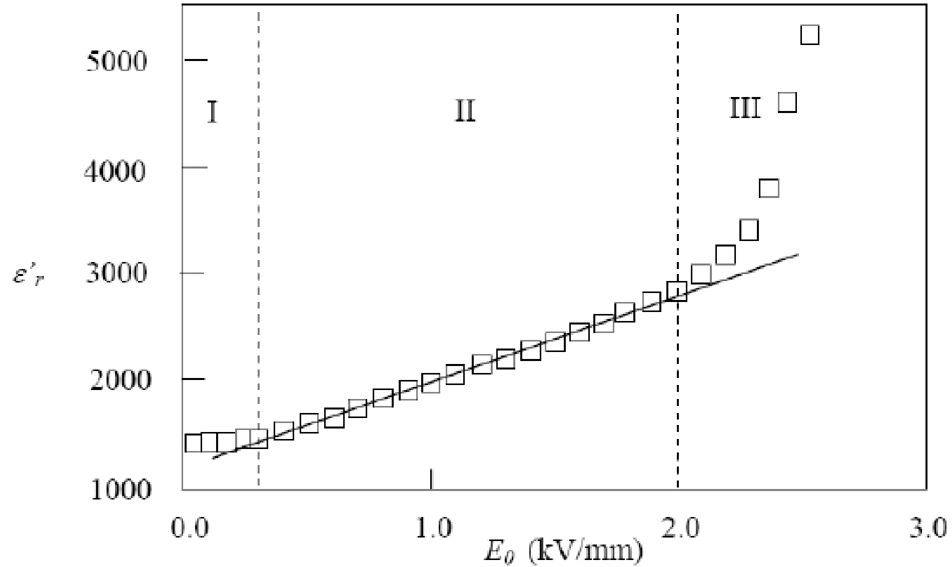

Figure 1.5. Schematic representation of the AC field dependence of dielectric permittivity in bulk $Pb(Zr,Ti)O_3$ ceramics. The low field region, (I), with relatively constant dielectric permittivity, the Rayleigh region, (II) where the dielectric permittivity increases linearly with the AC field amplitude and the high field region, (III) where a super-linear field-dependence of the dielectric permittivity is observed.[8]

At intermediate fields, the relative permittivity and piezoelectric coefficient are no longer constant. They change almost linearly with the AC field amplitude, resulting in a nonlinear dielectric and piezoelectric responses in the ferroelectric material. Rayleigh Law can be employed to analyze and quantify the intrinsic and extrinsic elements of the response in this region as will be further discussed. [7] Further increase in the amplitude of the electric field (i.e. high field region) leads to domain switching. In this region the Rayleigh law no longer applies and the field dependence is no longer linear but becomes sub- or super-linear.

The Rayleigh law applied to ferroelectrics describes the hysteretic response of domain wall motion from one potential energy well to another, under application of a

sufficiently high electric field to overcome the initial energy barrier (Figure1.5).[9] The Rayleigh law also assumes that there is a random distribution of pinning centers that comprise the domain wall energy profile [9]. It describes the response in sub-switching conditions where the dielectric (Equation 1.8) and piezoelectric (Equation 1.9) coefficients depend linearly on the applied electric field's amplitude:[10]

$$\varepsilon' = \varepsilon'_{init} + \alpha'_{\varepsilon} E_o \qquad \text{Equation 1.8}$$

$$d = d_{init} + \alpha_d E_o \qquad \text{Equation 1.9}$$

ε'_{init} and d_{init} are field-independent terms, dominant at low fields, and represent intrinsic ionic response as well as reversible domain wall vibration and motion. These parameters are usually referred to as the reversible Rayleigh parameters. The α_d and α'_ε terms represent irreversible domain wall or phase boundary motion (Figure 1.6) [11], and are usually referred to as irreversible Rayleigh parameters. Therefore, the ratios of the irreversible to reversible Rayleigh parameters, $\alpha'_\varepsilon/\varepsilon'_{init}$ and α_d/d_{init} , are considered as a quantitative measure of the extrinsic contributions to the dielectric and piezoelectric response, respectively, under the assumption that the extrinsic contributions to the reversible Rayleigh parameters are minimal. The prime sign equation 1.8 shows that the real part of the dielectric permittivity is being considered in this equation, which is calculated based on the dissipation factor, tanδ.

Other experimental approaches in order to distinguish between the intrinsic and extrinsic contributions to the dielectric and piezoelectric response include studying frequency [12-14], temperature [1,15], and aging time dependence [16,17] of the materials' response; however, all of these methods are only qualitative.[18] Rayleigh analysis is now

routinely used for quantitative measurements and has proved to work for direct dielectric/piezoelectric measurements as well as X-ray assisted and piezo-response force microscopy characterizations.[19] Therefore, Rayleigh analysis is used throughout this investigation for quantitative study of the extrinsic and intrinsic contributions to the dielectric and piezoelectric response of ferroelectric thin films.

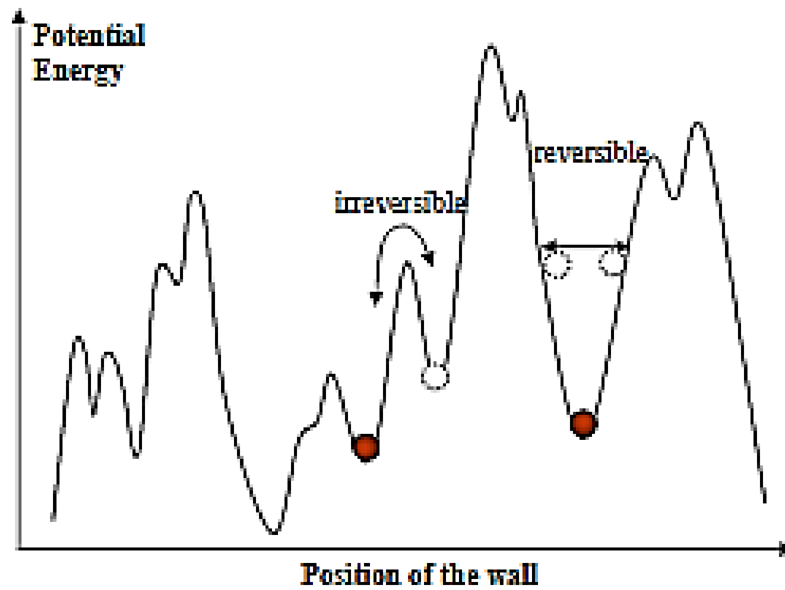

Figure 1.6. A schematic illustration of the potential energy landscape for interface (such as domain walls' or phase boundaries') motion with reversible and irreversible effects.[14]

Domain walls' motion and hence extrinsic contributions can comprise a major part of the piezoelectric and dielectric response of some ferroelectric materials such as PZT.[20] However, they are drastically suppressed in thin films with respect to bulk counterparts. This is due to the lower crystalline quality and larger concentrations of defects due to processing at lower temperature, smaller grain size and substrate clamping effects in thin films. Specifically, substrate-induced, long-range strain fields hinder non-180° domain wall motions, as it causes strain in the substrate-constrained direction.

Additionally, in a material with larger average grain size, population, variety and mobility of domain walls are increased leading to increased extrinsic contributions. Various factors affecting the dielectric and piezoelectric response of the film are discussed in detail in this investigation and special attention is paid to the role of extrinsic contributions throughout this work.

1.4 PZT and PMN-PT Material Systems

One of the most technologically relevant piezoelectric materials (especially in ceramic form) is lead zirconate-titanate, $Pb(Zr_xTi_{1-x})O_3$ (PZT) owing in part to its large dielectric and piezoelectric response at compositions close to x~ 0.52 (Table 1) [1,21,22]. PZT is a solid solution between anti-ferroelectric lead zirconate ($PbZrO_3$, PZ) and ferroelectric lead titanate ($PbTiO_3$, PT), and has a prototype perovskite (ABO_3) structure. Above T_c, PZT has a paraelectric cubic phase, but when cooled below T_c it transforms into ferroelectric rhombohedral ($x>0.52$), or tetragonal ($x<0.48$) phases depending on the composition (Figure 1.7). [9] Existence of another phase, monoclinic ($0.46<x<0.52$), has been also argued in some literature as shown in Figure 1.7 (b), which is still subject of debate between researchers, as if it is a new phase or a combination of the two other phases.[23]

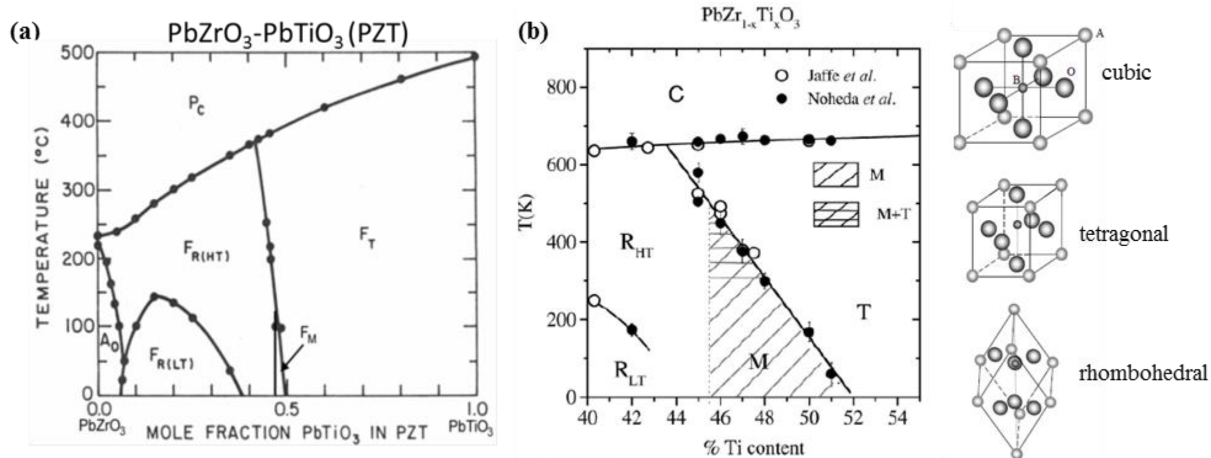

Figure 1.7. (a) The temperature-composition phase diagram for PZT[23] (b) Zoomed view of the temperature-composition phase diagram for PZT close to the MPB [24,25]

The tetragonal phase has six equivalent spontaneous polarization directions along the principal directions, while the rhombohedral distortion has eight degenerate spontaneous polarization directions along body diagonals. The piezoelectric coefficients rapidly increase at the phase boundary between the tetragonal and rhombohedral phase (i.e. morphotropic phase boundary, MPB) corresponding to x~0.52 (Fig. 1.7) [26]. This increase is in part due to an increased availability of polarization directions from both the rhombohedral and tetragonal distortions due to almost equal Gibbs free energies of the two phases. This allows for better and easier alignment and switching of the ferroelectric dipoles under applied electric field.

Peaking of the materials response close to the MPB composition also occurs in other ferroelectric solid solutions such as lead magnesium niobate-lead titanate, (1-x)$Pb(Mg_{1/3}Nb_{2/3})O_3$-x$PbTiO_3$ (PMN-PT). PMN-PT is a solid solution between anti-ferroelectric lead magnesium niobate, $Pb(Mg_{1/3}Nb_{2/3})O_3$ and ferroelectric lead titanate, $PbTiO_3$. Similar to PZT, it also has a morphotropic phase boundary between ferroelectric

tetragonal and rhombohedral phases at x~0.33 as shown in Figure 1.8. In bulk form, [001]-cut and -poled lead titanate-based relaxor-ferroelectric single crystals (at the compositions close to MPB) show several times higher piezoelectric response compared to PZT ceramics.[27,28] Therefore, integration of [001]-oriented relaxor-ferroelectric thin films, such as lead magnesium niobate-lead titanate on Si promises enhancement of the sensing and actuating capabilities of the MEMS devices (see section 1.5). However, there are challenges associated with the processing of textured and dense PMN-PT thin films that has hindered their application in thin film form so far. Chapter 6 discusses this material system in more detail.

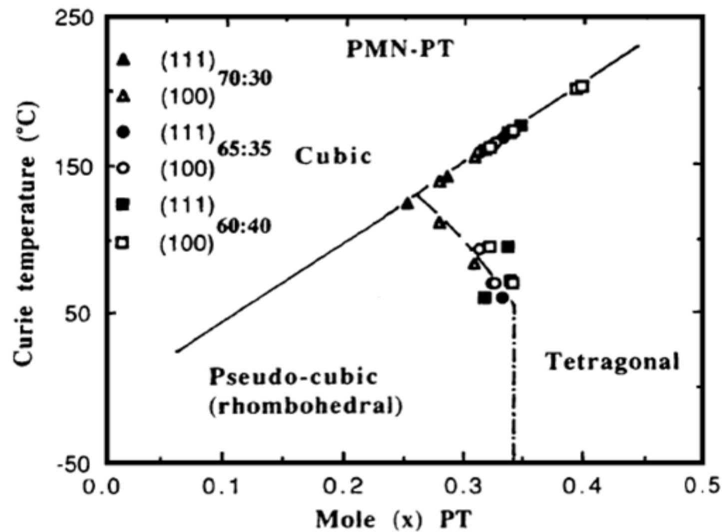

Figure 1.8. (a) The temperature-composition phase diagram for PMN-PT, showing an MPB at 0.33 mole fraction of PT at room temperature.[3]

In addition to the composition, dielectric and piezoelectric response of PZT and PMN-PT depend also on the crystallographic orientation along which the material is poled and characterized. However, an isotropic response is expected for ferroelectric materials in polycrystalline form with randomly oriented grains. In order to optimize the

dielectric or piezoelectric response, it is vital to control ferroelectric thin films' crystallographic texture. In single crystal, ferroelectric $PbTiO_3$-based solid solutions such as lead magnesium niobate-lead titanate, (PMN-PT) the largest piezoelectric response (d_{33}) is observed on the rhombohedral side of the morphotropic phase boundary (MPB), when the crystal is cut and poled along the <001> direction (pseudo cubic indices, see Figure 1.9). Similarly, in textured thin films of comparable composition, larger piezoelectric response are observed for films with (001) texturing with respect to (111) or randomly textured films.[1]

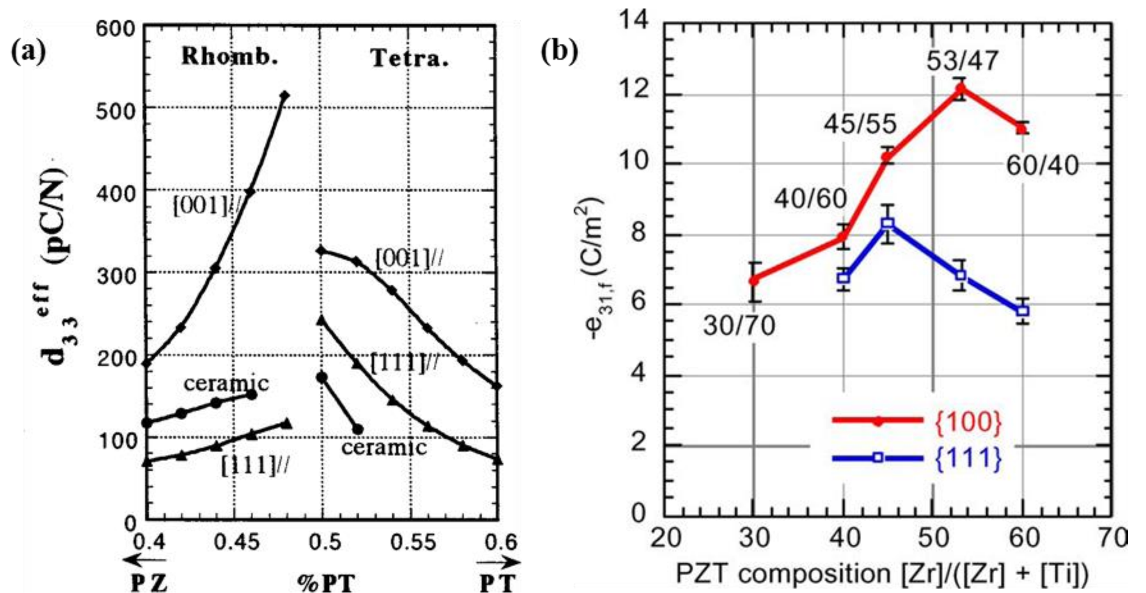

Figure 1.9. Compositional dependence of piezoelectric coefficients of PZT in ceramic compared to theoretical calculation (a) and in thin film form (b). The maximum response is observed on the rhombohedral side of the MPB along (100) direction.[1]

1.5 Ferroelectric Thin Films for MEMS Applications

The study of ferroelectric materials at small dimensions has been of increasing interest due to their many applications such as ferroelectric random access memory (FeRAM), multilayer capacitors, and micro-electromechanical systems (MEMS). In particular, due to the strong piezoelectric response, they are excellent candidate for MEMS sensor, actuator and relay applications. Non-ferroelectric piezoelectrics, such as AlN and ZnO are also extensively used and incorporated as active materials in MEMS devices.[1] However, the higher piezoelectric response of ferroelectric thin films enables fabrication of devices with superior performance, i.e. actuators capable of exerting higher forces and larger deformations or sensors with higher sensitivity. Hence, integration of ferroelectric materials with large piezoelectric coefficient into MEMS devices can not only enhance their performance, but also potentially decrease the required operating voltage level of the devices below the CMOS compatibility limits, allowing true miniaturization of these systems. Among ferroelectric materials, lead zirconate titanate (PZT) is one of the most studied compositions for piezoelectric MEMS applications. This is in part due to its large piezoelectric response, represented by d_{31} and d_{33} in the Table 1.1.[1,28]

Dielectric and piezoelectric properties of ferroelectric materials are influenced by their chemical composition and homogeneity, microstructure, crystalline size and quality and crystallographic orientation. Study of the fundamental science and processing-structure-properties relationship of ferroelectric thin films with enhanced piezoelectric response towards integration into micro- and nano-electromechanical systems is the focus of this work. Accordingly, different variables have been examined in this study to

influence the piezoelectric response of the Pb-based ferroelectric oxide thin films with respect to the mentioned factors. The optimized ferroelectric films with enhanced piezoelectric response were then released from the Si substrate to mimic MEMS device configuration and further investigate the substrate clamping effects on the functional performance of the film.

Table 1.1 Piezoelectric and dielectric coefficient of various materials in thin film form [1,29]

Material	Composition	d_{31} (pC/N)	d_{33} (pC/N)	ε_{33}
PZT (composition dependent)	Ferroelectric	-94 to -274	80 to 593	425 to 1900
$BaTiO_3$	Ferroelectric	78	190	1700
PVDF	Ferroelectric	23	-35	4
ZnO	non-ferroelectric	-4.7	6 to12	8.2
AlN	non-ferroelectric	-3	5	10

1.6 Thesis Organization

Based on the above overview, the rest of this thesis is organized as follows:

Experimental Procedures (Chapter 2)

This chapter details the processing and characterization of PZT and PMN-PT thin films and membranes as investigated in this work. This includes preparation of the substrate and bottom electrode stack, film deposition, top electrode processing, and procedures for microstructural, chemical, dielectric and piezoelectric characterizations.

Processing of (100)-Textured PT-solid solution Ferroelectric Thin Films (Chapter 3)

This chapter describes the fundamentals steps of chemical solution deposition and discusses the optimization of the processing of PZT and PMN-PT thin films with respect to texture and microstructure.

Critical Thickness in Extrinsic Contributions in (100)-oriented PZT Films (Chapter 4)

The focus of this chapter is the study of the effects of crystal size on the dielectric and piezoelectric response of ferroelectric films. The severity and sources of the degradation of the functional responses in PZT thin and ultra-thin films are investigated in terms of films' thickness.

Chemical Heterogeneities in Ferroelectric Thin Films, Superlattice-Like PZT Films (Chapter 5)

Formation of compositional gradients through the film thickness in PZT films was studied and exploited towards maximization of the dielectric and piezoelectric response of the material in small thickness ranges. Careful control of the processing conditions resulted in superlattice-like thin films with superior functional properties.

Alternative Material System: Relaxor-Ferroelectric, PMN-PT Thin Films (Chapter 6)

The focus of this chapter is processing optimization for lead magnesium niobate-lead titanate, PMN-PT thin films. Microstructural characteristics such as texture, phase content and density of thin films proved to be critical in order to achieve the highest piezoelectric response.

Substrate Clamping Effects, PZT membranes (Chapter 7)

This chapter discusses the importance of the substrate-induced long range strain fields on the dielectric and piezoelectric response of the ferroelectric oxide films. A giant piezoelectric response was obtained after removal of the Si substrate from the film via back-side etching. A change in the paradigm of the electromechanical activity of the grains in the film was observed in PFM investigations.

Conclusions and Future Work (Chapter 8)

Overall results and findings of this study are summarized in this chapter and also suggestions for future works are provided.

Chapter 2

Experimental Procedures

This chapter details the processing and characterization procedure of Pb-based ferroelectric oxide thin films and membranes studied in this work. These include lead zirconate-titanate, $Pb(Zr_{0.53}Ti_{0.47})O_3$ (PZT) and lead magnesium niobate-lead titanate, $(0.7)Pb(Mg_{1/3}Nb_{2/3})O_3$–$(0.3)PbTiO_3$ (PMN-PT) thin films and membranes, which were processed on platinized silicon substrate via chemical solution deposition. Characterization of the films' properties, including film thickness, crystallographic phase and microstructure, dielectric permittivity and nonlinearity, polarization–electric field (P-E) hysteresis loops and $d_{33,f}$ piezoelectric coefficients will be discussed.

2.1 Chemical Solution Deposition of Ferroelectric Oxide thin Films

Chemical solution deposition offers a number of advantages over other deposition methods. These include comparatively low capital investment costs, good homogeneity and thickness uniformity over a large area with minimal variations (≤3%),[30] as well as enhanced compositional control.[31]

The fabrication of ferroelectric oxide thin films through CSD is achieved through four basic steps: (i) synthesis of the precursor solution; (ii) deposition by spin or dip coating; (iii) a low-temperature heat treatment (typically 300-400°C) for removal of the solvent and most of the organic components, resulting in formation of an amorphous

film; (iv) densification and crystallization of the amorphous film into the desired phase via a high temperature heat treatment (typically 600 to 850°C, although the actual range is much wider and material dependent). Step (iii) is usually referred to as “pyrolysis”, due to the fact that it results in the thermal (pyro) decomposition (lysis) and in large part removal of the organic components of the film.[32] Careful control of deposition and heat treatment condition is necessary to obtain dense and textured thin films as will be discussed in more details in the next chapter.

2.1.1 Solution Preparation

The PZT and PMN-PT precursor solutions used in this work were synthesized with 2-methoxyethanol (2MOE) as solvent and following the routes described by Wolf and Trolier-McKinstry[27] and Park and Trolier-McKinstry,[33] respectively. Synthesis steps for the PZT precursor solution are schematically shown in Figure 2.1. Zirconium (IV) propoxide solution, $Zr(OCH_2CH_2CH_3)_4$ 70 wt.% in 1-propanol (Sigma-Aldrich, Inc.), and titanium (IV) propoxide, $Ti[OCH(CH_3)_2]_4$ 97% (Sigma-Aldrich, Inc.) were dissolved in 2MOE, $CH_3OCH_2CH_2OH$ 99.9% (Sigma-Aldrich, Inc.) and stirred at room temperature for 30 minutes in Argon environment. In a separate flask, lead acetate tri-hydrate, $Pb(CH_3CO_2)_2 \cdot 3H_2O$ 99.99% on a trace metals basis (Sigma-Aldrich, Inc.) was dissolved in 2-methoxyethanol and vacuum distilled at 120°C until a white fluffy matter is obtained. After that, the mixture of Zr and Ti precursors was added to the Pb flask and the entire solution was stirred for 2 hours at 120°C. Finally, the solution was adjusted to the desired concentration by adding 2MOE or vacuum distillation. PZT solutions with 0.1M, 0.2M and 0.4M concentrations were used in this work.

The precursor solutions for Pb-based ferroelectric compositions are often over-batched for Pb content with respect to stoichiometric requirements to compensate for the Pb loss at elevated processing temperatures. The specific amount of over-stoichiometric Pb is dependent on the thickness of the single layer being pyrolized, the number of layers crystallized together, as well as the thermal treatment conditions. The PZT precursor solutions used in this work were synthesized with 20 M% excess lead for solutions of 0.2M and 0.4M concentrations and 40 M% excess lead for solutions of 0.1M concentration.

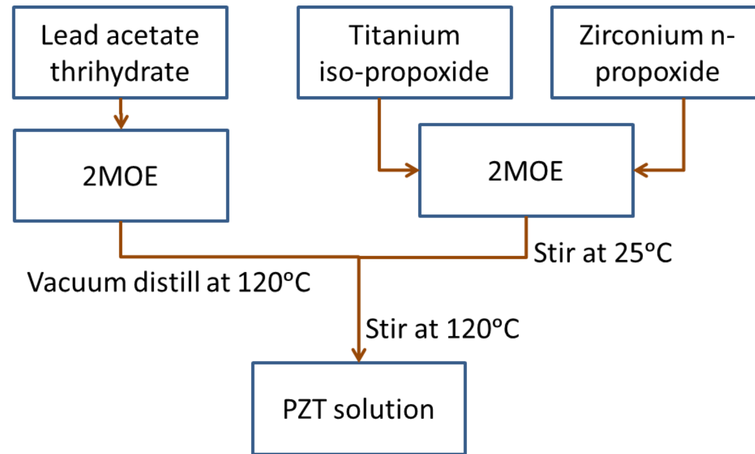

Figure 2.1: Flow chart for preparation of PZT solution as described in Wolf. et al.[27]

Similarly, 2MOE-based PMN-PT precursor solutions were prepared as shown in Figure 2.2 after the route described by Park and Trolier-McKinstry.[33] Lead acetate trihydrate, $Pb(CH_3CO_2)_2 \cdot 3H_2O$, (99.99% purity) magnesium ethoxide, $Mg(OC_2H_5)_5$, (97% purity, Sigma-Aldrich, Inc.) niobium ethoxide, $Nb(OC_2H_5)_5$, (99.99% purity, Sigma-Aldrich, Inc.) and titanium (IV) Isopropoxide, $Ti[OCH(CH_3)_2]_4$ (97% purity) were

used as starting materials. PMN–PT solution was synthesized with a 70:30 PMN to PT ratio, on the rhombohedral side of the morphotropic phase boundary composition.

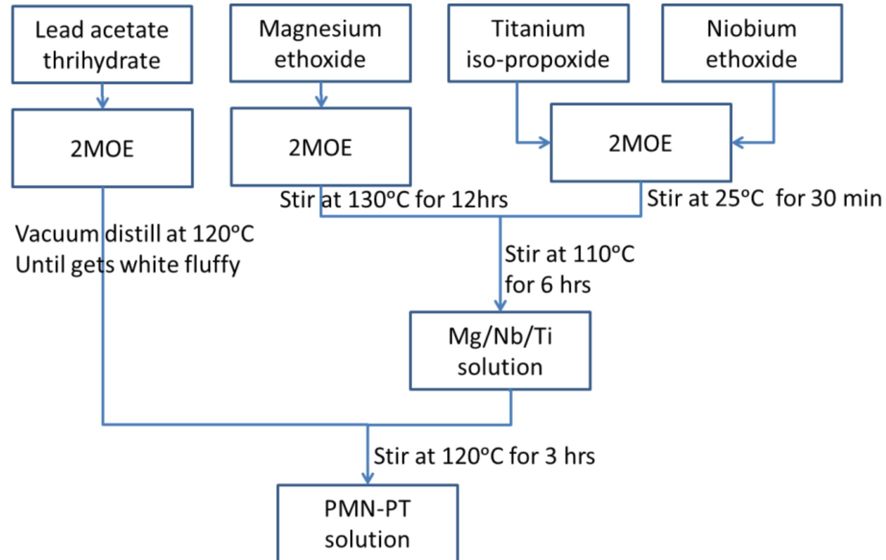

Figure 2.2: Flow chart for preparation of PMN-PT solution as described in Park et al.[33]

2.1.2 Substrate Processing

The substrates used in this work were platinized silicon, (111) Pt (1500 Å)/ Ti (200 Å) /SiO_2 (1μm) /(100) Si. Bare Si substrates were first cleaned via standard CMOS cleaning procedure. They were submerged into Piranha solution at 90-120ºC for 10 minutes and rinsed with water, then dried in a spin dryer. 1 micron of silicon oxide was thermally grown in an oxidation furnace at 1100 ºC for ~48.5 hours. Calculations of the required time in the furnace can be obtained from:

http://www.cleanroom.byu.edu/OxideTimeCalc.phtml

A 20 nm Ti, as an adhesion layer, and a 150 nm of Pt, as a bottom electrode were then sputter deposited on the oxide buffer layer in a Unifilm sputtering tool, one after the other and without breaking the vacuum. To ensure uniformity of the deposition, wafers were held spinning and placed at various positions with respect to the target in the sputterer during deposition. Ti and Pt layers were deposited at the rates of 100 Å/min and 200 Å/min respectively. The Pt layer thus obtained is highly (111) oriented as observed in XRD pattern (Figure 2.3), and can withstand the crystallization time and temperatures needed for the ferroelectric films processed in this work.

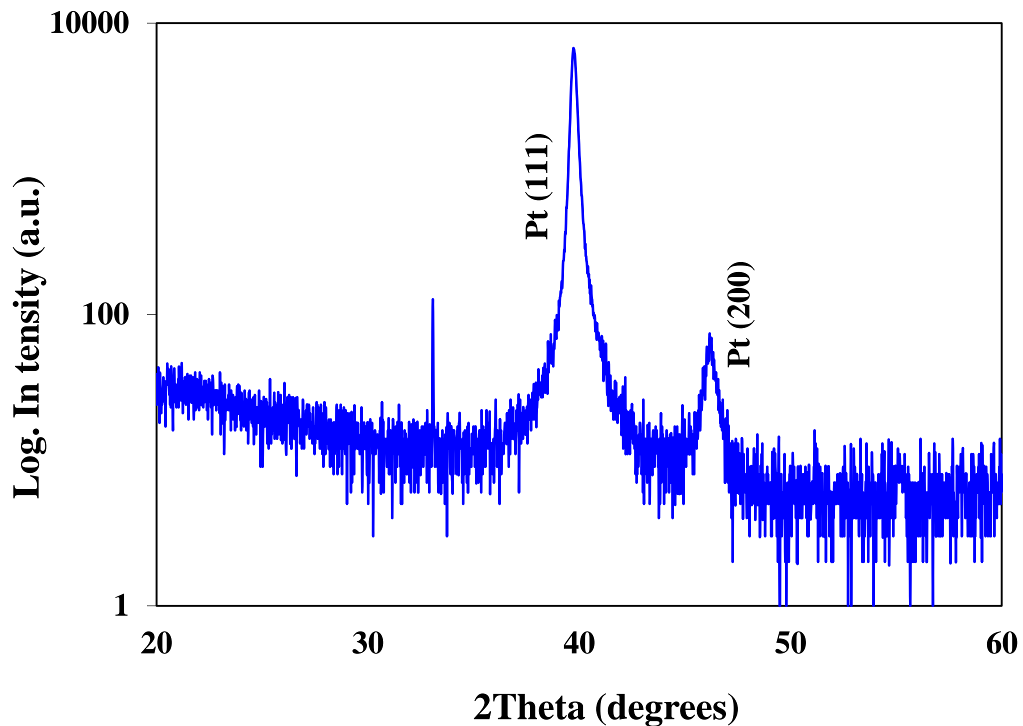

Figure 2.3 XRD pattern of a platinized silicon substrate. (see section 2.2)

2.1.3 Thin Film Deposition

Platinized silicon substrates, (111) Pt (1500 Å)/ Ti (200 Å) /SiO2 (1µm) /(100) Si, purchased from Nova Electronic Materials Inc. or prepared in-house as described in the previous section, were used in this work. Before deposition, the wafer was squirt-washed by acetone and isopropyl alcohol (IPA) and dried with a nitrogen gun. The surface was further dried by placing it on a hot plate at ~200°C for 1 min. Precursor solution was then spun onto the substrate at 3000 rpm for 30 s. Dispensing the solution on the substrate is a very important step, since small air bubbles might form during the process at the interface of the substrate and the solution. Later during spinning, the eventual bubbles can burst and form defective discontinuities, pinholes, in the film. The viscosity and the speed of the front of the dispensed sol are the key parameters in formation of the bubbles.[34] To provide an estimate of the solution front advancement speed, dispensing of the sol on a 1 $inch^2$ sample takes about 5 seconds. This phenomenon has been studied in other applications such as the coating of liquid polymers on the membrane substrates in the polymer electrolyte membrane (PEM) fuel cell manufacturing process.[35]

As-deposited films were pyrolyzed on a hot plate at temperatures ranging from 300°C to 400°C, for 1 min, unless otherwise specified. A simple COMSOL thermal analysis (considering conduction and convection from the surface of the film) of a 1 inch square sample with platinized Si substrate on a 400°C hot plate shows that the PZT layer reaches the steady state temperature of ~375°C in less than a second after placing it on the hot plate in air at room temperature. The sample is then crystallized in a Rapid Thermal Annealer (RTA) at temperature equal to or higher than 700°C for 1 min in air

(See Chapter 3). A heating rate of 60°C/s in the RTA was used in this work. Cooling starts by the shut off of the radiation lamps and the subsequent cooling temperature profile is not further controlled. The temperature profile during crystallization in RTA is shown in Figure 2.4. The desired thickness was achieved by repeating the deposition steps. Each deposition and anneal yields a ceramic layer of about 30 to 60 nm in thickness for a 0.2 or 0.4 M solution, respectively.[36]

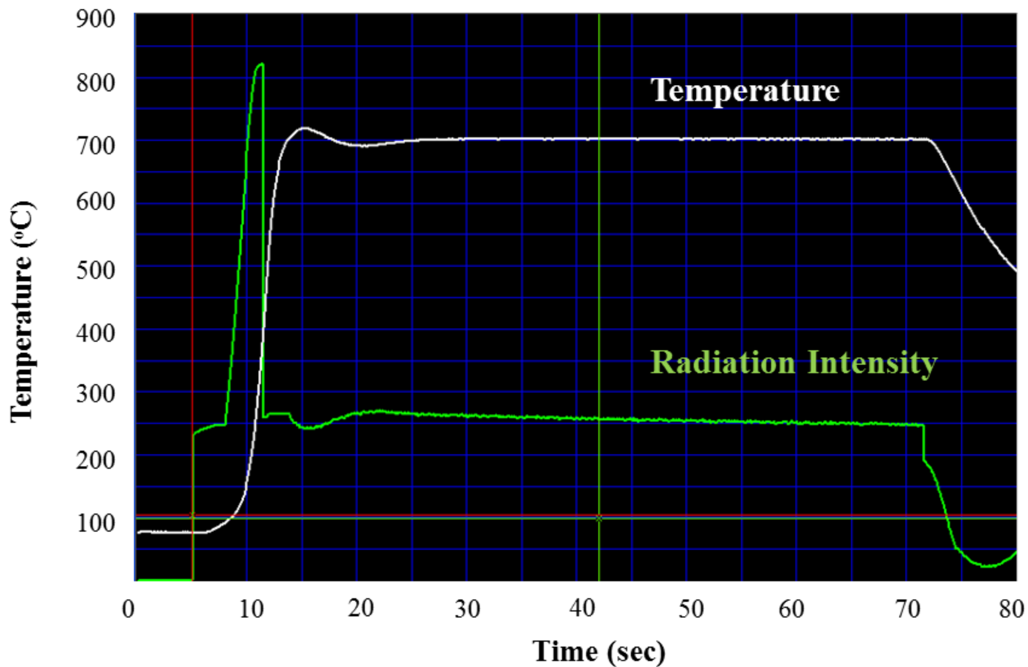

Figure 2.4: A representative temperature profile of the rapid thermal anneal processing of the PZT thin films.

2.2 Structural Characterization, X-ray Diffraction

X-ray diffraction (XRD) is a versatile, non-destructive technique (assuming limited x-ray exposure during the scan[37] which is a correct assumption for the laboratory x-ray setting) that provides information regarding chemical composition and crystallographic structure of the material using x-ray emission. A monochromatic (single

wavelength) x-ray incident beam is emitted upon the sample and scanned at a range of incident angles, such that diffraction (i.e. constructive interference) occurs at some specific incident angles. In θ-2θ scans, the diffracted beam intensity is collected at an angular position of twice the incident beam. High intensity peaks result when the Bragg diffraction condition (Equation 2.1) is satisfied, thereby providing information regarding the crystallographic planes present. The position of the peaks in the plot of the diffracted x-rays collected by the x-ray detector represent the incidence angle corresponding to a specific family of atomic planes in the sampled crystal (Figure 2.3). The relationship between the x-ray wavelength and interatomic spacing to the angle of diffracted beam is described via Bragg's law (Equation 2.1) and is illustrated in Figure2.5.

$$n\lambda = 2d_{space}\sin\theta \qquad \text{Equation 2.1}$$

In Equation 2.1, n is an integer, λ is the wavelength of the incident x-ray, d_{space} is the interplanar spacing of the crystal, and θ is the angle of incidence.

Standard θ-2θ scans with X-Ray diffraction, XRD, were performed for crystallographic phase and texture identification of the films. A PANalytical X'Pert PRO diffractometer (Almelo, Netherlands) with Cu-Kα radiation was used (Figure 2.6). The X-ray generator was set at 45 kV and 40 mA. PZT films were scanned in 2θ from 20 to 70 degrees, with a step size of 0.02° at the rate of 10 s/deg. The incident beam optics included a 10 mm mask (providing a vertical slot with 10mm width) and an anti-scatter slit fixed at 1°. The diffractive beam optics included a 5.0 mm antiscatter slit. The Si (004) peak at 2θ =69.6° was used to calibrate the obtained XRD patterns.

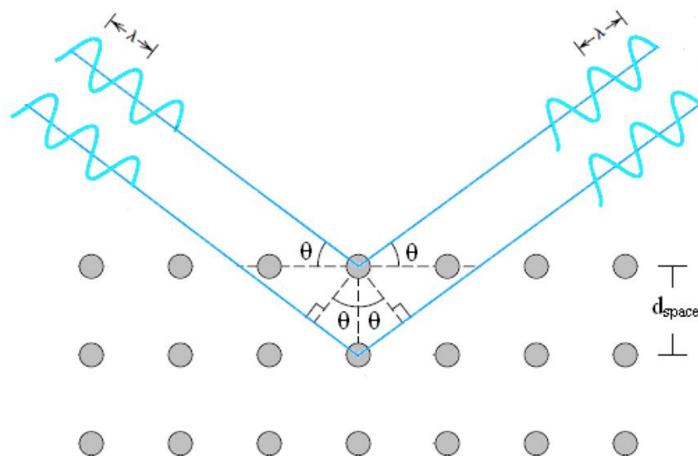

Figure 2.5. Schematic illustration of Bragg's law of diffraction for crystalline solids.[18]

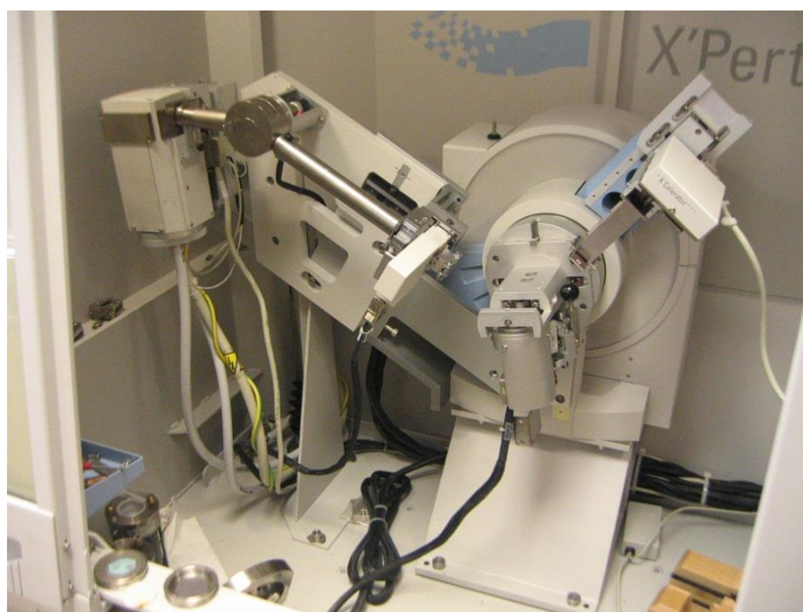

Figure2.6: X'Pert PRO Alpha-1 diffractometer with a CuK_a radiation and θ-2θ goniometer used in this work.[18]

Lotgering factor[38] calculations were used to characterize the degree of crystallographic texturing of the films: measured peak intensities from the films were compared to the powder diffraction data from the corresponding PDF card (shown in Table 2-1).

Table 2-1: Powder diffraction file numbers used for XRD scan (from ICDD PDF-4 2010)

Material	PDF #
$Pb(Zr_{0.53}Ti_{0.47})O_3$	01-070-4264
$PbTiO_3$	00-040-0099
$0.7Pb(Mg_{1/3}Nb_{2/3})O_3$–$0.3PbTiO_3$	01-076-9082
Pt	01-087-0640

The Lotgering factor calculation for (100)-orientation was based on the following equation[39] (2-1):

Eq. (2-1): $$f = \frac{P-P^0}{1-P^0} \quad \text{where} \quad P = \frac{I_{(100)}+I_{(200)}}{\sum I_{(hkl)}}$$

where $I_{(100)}$ is the intensity (integrated peak intensity) of the (100) PZT peak, $I_{(200)}$ is the intensity of the (200) PZT peak, and $\Sigma I_{(hkl)}$ is the sums of the intensities of all of the PZT peaks. P was used for the film under texture evaluation and P^0 for the standard powder profile as reported in the PDF file. The Lotgering factor can be likewise calculated for the degree of (111) orientation of the film by replacing the (h00) peak intensities with that of the (111) peaks.

2.3 Thickness Measurement

The film thickness was characterized using a Dektak 150 contact profilometer (Veeco Instruments, Plainview, NY). A step was created via wet etching of a corner of the film. A solution of Buffered Oxide Etchant (BOE, ammonium fluoride (HN_4F)/hydrofluoric acid (HF), J.T. Baker) in water (1:6 ratio) was used for lead titanate,

($PbTiO_3$, PT) or PZT films. This approach provides a high etch selectivity of PZT over bottom electrode Pt. The remainder of the film was protected with Kapton tape. However, etching PMN-PT turned out to be quite difficult and very slow, even with HF. Cross sectional imaging with Scanning Electron Microscopy (SEM) was used to determine the thickness of the PMN-PT films, and also to verify the thickness of PZT films.

2.4 Microstructure Characterization

The cross sectional grain morphology was examined using field emission scanning electron microscopes, SEM (S-4700 FE-SEM Hitachi, Hitachi Instruments, San Jose, CA and Ultra 60 Zeiss, Carl Zeiss Microscopy, LLC North America, Peabody, MA). Plain view SEM images were used to characterize the average grain size of the films based on average intercept length method.[40] SEM imaging was performed at an accelerating voltage of 5KV and current of 10µA. Atomic Force Microscopy, AFM, was used for additional surface microstructure characterization (Nanoscope Microscope, Digital Instruments Veeco Metrology Group, Chadds Ford, PA). The tapping mode was used to examine the grain size and surface roughness of PZT films. Silicon cantilevers, 160 µm long with a 300 kHz resonance frequency were used.

2.5 Chemical Characterization: X-ray Photoelectron Spectroscopy, XPS

X-ray photoelectron spectroscopy (XPS) is a semi-quantitative surface chemical analysis technique used to detect the chemical composition and chemical bonding state of the elements present on the surface of a sample as well as their abundance. XPS spectra are obtained by irradiating the material with a monochromatic beam of X-

rays while simultaneously measuring the kinetic energy and number of electrons that escape from the surface (depth of 1 to 10 nm) of the material being analyzed. To obtain depth profile chemical characterization, ion-beam etching is used to access and expose the bulk of the sample to the X-ray beam. XPS requires ultra-high vacuum (UHV) conditions.

In this work, XPS data has been collected at a 400 μm spot size diameter, under a vacuum of 10^{-7} to 10^{-10} Torr. Depth profiling was conducted by Ar etching generating a circular crater of 2 mm radius, with an etch rate of ~2 nm/min for PZT. A measurement was obtained after each etching period of 20 to 40s. The sample was rotating during ion-etching to ensure a flat and symmetrical etched surface in the crater.

2.6 Dielectric Characterization

To perform dielectric and piezoelectric characterization, 70 nm-thick circular Pt top electrodes with three different diameter sizes, 100 μm, 500 μm and 1 mm were sputter-deposited via the lift off method. NR9-1500PY negative photoresist (Futurrex Inc. Franklin , New Jersey 07416) was spun onto the film surface at 2000 RPM for 40 sec and then dried at 150°C on a hot plate for 1 min. Ultra violet (UV) exposure was performed in a mask aligner (Karl Suss MA6, Suss MicroTec Lithography GmbH, Garching, Germany) with UV light of 365 nm wavelength, at the dose of 300mJ/cm^2. Following a post-bake at 100°C for 1 min on a hot plate, the resist was developed in RD6 developer for ~10 sec, and then rinsed with deionized (DI) water. Pt was then sputter deposited on the patterned sample, resulting in 70 nm-thick Pt top electrodes after the lift-off process

in the acetone. After electroding, samples were heated on a hot plate at 350°C for 20 min to enhance the contact between top electrode and the film.

The films' dielectric response was measured using an Agilent 4284A Precision LCR meter (Agilent Technologies, Santa Clara, CA). Low field measurements were made at 1 kHz and 0.02 Vac (rms), unless otherwise specified. Micromanipulator probes (Micromanipulator Co., Carson City, NV) were used throughout this study for making contacts to the top and bottom electrodes. The capacitances were used to calculate the relative dielectric permittivity, ε_r based on parallel plate capacitor model, assuming a uniform electric field between the electrodes, constant thickness and a uniform material:

$$C = \frac{\varepsilon_0 \varepsilon_r A}{t} \qquad \text{Equation 2-2}$$

where C = Capacitance (F), ε_0 = permittivity of vacuum (8.85 x 10^{-12} F/m), A = electrode area (m^2), and t = thickness (m) of the PZT film.

Polarization-electric field hysteresis loops (P-E loops) were obtained using a P-PM2 Radiant ferroelectric test setup (Radiant Technologies Inc. Albuquerque NM). The P-E loops were used to determine the remanent polarization (P_r), maximum polarization (P_{max}) and coercive field (E_c) of the films. All polarization-electric field measurements were made at 1 KHz.

The electric field dependence of the dielectric response was studied to quantify the intrinsic and extrinsic contributions to the room temperature dielectric response. The capacitance and dissipation factor of the electrodes were measured at ac fields ranging from ~2 kV/cm up to the films coercive field (~40-80 kV/cm for PZT films) at 1 kHz.

The sub-coercive, linear, Rayleigh region was identified, and the intercept and the slope of the linear dependence were calculated as reversible and irreversible Rayleigh parameters. This was confirmed by predicting the P-E hysteresis loop and obtaining a close match between the predicted and measured loop.

2.7 Piezoelectric Measurements

Two approaches based on the direct (charge measurement) or the converse (strain or displacement) piezoelectric effect can be used to characterize the electromechanical response of the ferroelectric thin films. In this research, the effective longitudinal $d_{33,f}$ piezoelectric coefficient has been measured via high resolution displacement measurement (converse effect). Double beam laser interferometery and piezoresponse force microscopy were used for piezoelectric characterization in this work as described below.

2.7.1 Double beam laser interferometry

A custom-made aixACCT DBLI double beam laser interferometer system, (aixACCT Systems GmbH, Aachen, Germany) was used to characterize the macroscopic electromechanical response of the piezoelectric thin films (collective piezoelectric response of the film beneath the electrode area).

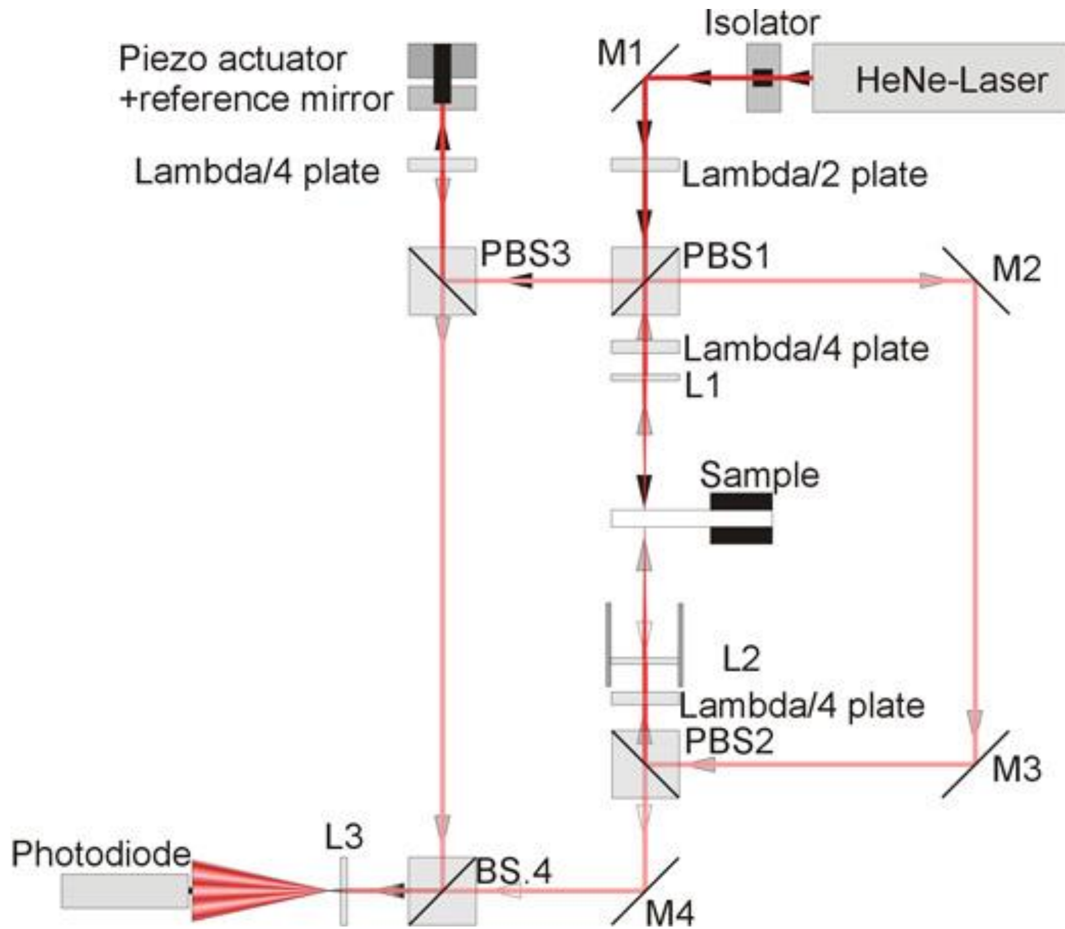

Figure 2.7. Optical beam path of a typical double-beam laser interferometer. A darker beam color indicates two overlaying Beams. The patterned beam indicates interference of two beams. Lambda plates are used for polarization rotation and the isolator keeps reflected light from re-entering the stabilized beam source.[41]

A double beam laser interferometer measures the differential displacement of the two major surfaces of the sample (i.e. top electrode and bottom Si surface), resulting from an applied electric field to the piezoelectric capacitor. Figure 2.7 shows the optical path of a typical double beam laser interferometer, where the interference pattern is detected at the photodiode, between a reference beam and another beam reflecting on the both sides of the sample to measure the change in the film thickness.[41,42] Such a setup, as compared with a single beam interferometer measuring only the top surface displacement, effectively eliminates contributions from the bending of the substrate as a

side-effect of the piezoelectric response of a thin film constrained to a thicker substrate as shown in Figure 2.7. $d_{33,f}$ –E_{DC} hysteresis loops were collected by sweeping the DC bias voltage from 0 to ±2X-3X of E_c, while having the ac amplitude of ~$0.2E_c$ at frequencies ranging from 100 Hz to 10KHz. Strain (displacement) versus the ac field amplitude can also be used to characterize the piezoelectric response of the films, however it requires further analysis to obtain the piezoelectric response from the measured displacement and it doesn't show the effects of the bias field on the piezoelectric response.

2.7.2 Piezoresponse Force Microscopy (PFM)

Piezoresponse Force Microscopy (PFM) characterizes the local piezoelectric response (versus collective volume response) of the film at the point of the contact of the AFM (Atomic Force Microscope) tip. In this scanning probe microscopy technique, the displacement of the surface of the film in contact with the AFM tip is measured and used to characterize the piezoelectric response with respect to the applied ac voltage at the tip of a cantilever. However, PFM is not an accurate quantitative characterization method as the tip/film contact is heavily affected by the film topography and also the electric field distribution is not uniform. The underlying Pt layer is grounded and used as bottom electrode. The amplitude and the phase of the measured response yield information about the piezoelectric coefficient and the polarization status of the ferroelectric film.[18]

In PFM scans, an AC voltage is applied between the conductive tip and the bottom electrode located underneath the ferroelectric thin film being tested. The application of the time varying voltage results in an oscillating surface displacement due to the converse piezoelectric effect. This change in surface displacement results in the

cantilever being driven into oscillation (Figure 2.8). As shown in Figure 2.8, the in-plane and out-of-plane components of the electromechanical response of the film in addition to topographical information of the surface can be obtained. If the driving frequency of the PFM approaches contact resonance, then the recorded deflection of the cantilever can increase by orders of magnitude, which results in an increase in sensitivity (i.e. increase in signal-to-noise ratio).[18] However, due to topographic variations, the resonant frequency can often change during a measurement.

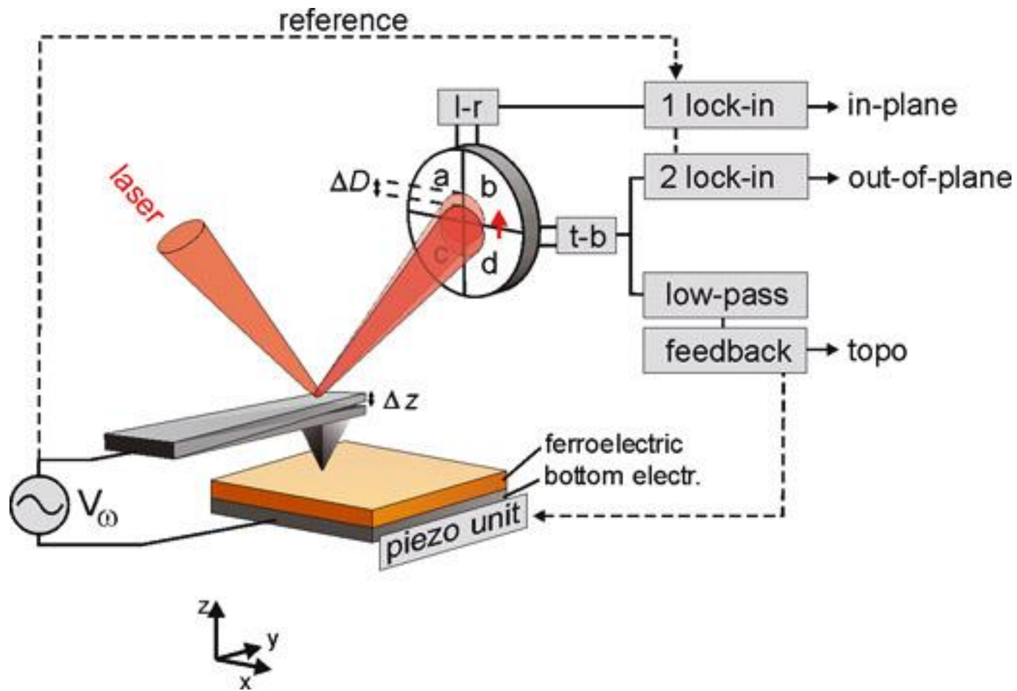

Figure 2.8. PFM setup to simultaneously acquire the topography and the in- and out-of-plane component of the surface displacement. A function generator is used to apply an alternating voltage V_ω between the tip and the bottom electrode of the ferroelectric. The voltage induced cantilever deflection is detected by a reflected laser beam on a four sector photodiode.[43]

Band-Excitation Piezoelectric Force Microscopy (BE-PFM) as shown in Figure 2.9, has been developed by S. Jesse et al.[44] to ensure maintaining the enhanced sensitivity throughout the scan. In this technique, the input signal excites the cantilever with a band

of frequencies. The frequency band is chosen such that the resonance frequency of the system is captured for all points along the sample's scanned area. Analysis of the measured displacement yields the actual resonant frequency and displacement amplitude at each point. PFM studies in this work were carried out on a commercial AFM system (Asylum Cypher) at 1 V_{pp} (peak to peak) ac field applied to a Pt/Cr-coated probe (Budget sensors Multi75E-G) in addition to the DC envelope.

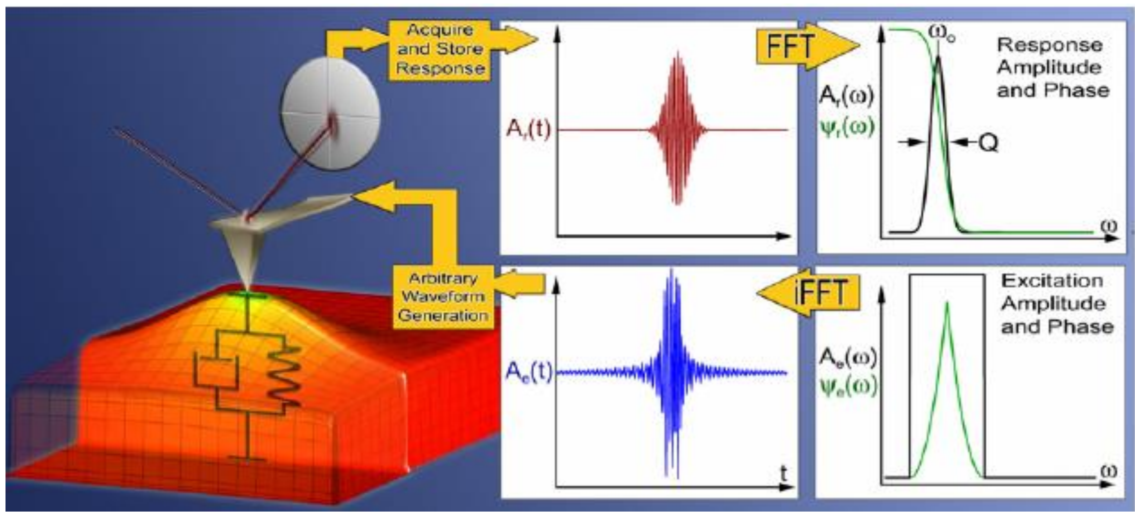

Figure 2.9: BE-PFM setup for conducting piezoresponse measurements where A=response amplitude, Ψ=phase, ω_o= resonance frequency, and Q=mechanical quality factor.[44]

2.8 Back-side Etching of the Si Substrate

The effects of substrate clamping on the dielectric and piezoelectric response of the (100)-oriented PZT thin films on platinized Si substrate were investigated by back-side etching of the Si substrate from the original ~500 μm to a residual Si thickness of ~10-20 μm. A squared area of ~1cm^2 in the middle of the sample was ion-etched, while the rest of the sample was protected by thick photoresist (SPR 220, MicroChem, Newton, MA) or Kapton tape. Bosch® Si etching process was used to back-side etch the substrate

in multiple steps, using an inductively coupled plasma etcher, (STS-ICP, Surface Technology Systems, Newport, UK). The Bosch process[45] also known as pulsed or time-multiplexed etching alternates repeatedly between two operation modes to achieve almost vertical etching, as shown in Figure 2.10:

1. A standard, nearly isotropic plasma ion etch. Sulfur hexafluoride SF_6 was used in this tool.
2. Deposition of a chemically inert passivation layer, such as Teflon.

Each phase lasts for several seconds. The passivation layer protects the entire substrate from further chemical attack and prevents further etching. However, during the etching phase, the directional ions that bombard the substrate attack the passivation layer at the bottom of the trench (but not along the sides). They collide with it and sputter it off, exposing the substrate to the chemical etchant. These etch/deposit steps are repeated many times over, resulting in a large number of very small isotropic etch steps taking place only at the bottom of the etched pits. Each cycle in the process used in this work included 8 sec of passivation and 10 sec of etching, resulting in an etch rate of 0.6 ±0.05 μm/cycle.

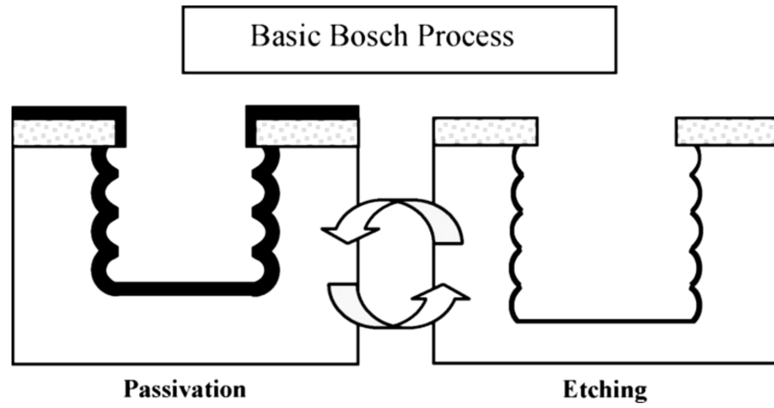

Figure 2.10: Schematic viewgraph of the basic Bosch process.[46]

Chapter 3

Processing of Highly (100)-Textured PZT Thin Films

This chapter is dedicated to optimizing the processing of CSD-derived PZT thin films. Specific attention has been paid to the factors affecting the microstructural development of the films, including synthesis of the precursor solution, preparation of the substrate and bottom electrode stack, and heat treatment conditions. Elements of the films' microstructure; phase content, crystallographic texture, grain size and density and chemical homogeneity will be discussed as well.

3.1 Chemical Solution Deposition

Pb-based Ferroelectric oxide thin films (such as PZT) are synthesized through both physical and chemical deposition methods. Sputtering, pulsed laser deposition, ion beam deposition and laser ablation are among the physical deposition methods utilized.[47,48] Chemical deposition methods include chemical vapor deposition (CVD), and chemical solution deposition (CSD) methods such as sol-ge1[26] and metal-organic decomposition (MOD).[49,50] CSD offers a number of advantages over other methods of thin film fabrication, and is used in this work for processing the ferroelectric thin films. Comparatively low capital investment costs, good homogeneity and thickness uniformity over a large area with minimal variations (≤3%),[30] as well as enhanced compositional control[51] are some of the advantages of CSD.

As discussed in chapter 2, two separate heat treatment steps are typically used in this processing method to transform the amorphous as deposited film into final multi-grain crystallized form; pyrolysis and annealing. Development of the film microstructure takes place via nucleation and growth processes during these heat treatment steps. Nucleation events often start during pyrolysis, while complete crystallization is achieved only with the higher thermal treatment temperatures.[51] Hence, three major factors can be considered to contribute to the creation of the film's final microstructure: the precursor solution, the substrate used, including the eventual bottom electrode stack, and the thermal treatment conditions, including thermal profile and processing atmosphere. The following sections will discuss in detail each of these elements and their correlation with the development of the film's microstructure.

3.2 Precursor Solution

The precursor solution used in CSD usually consists of a solvent and other metal-organic compounds for each of the cations in the final material. The solvent and the chemical precursors used for the various cations, as well as the steps employed in the preparation of the precursor solution, dictate the specific procedures for handling and storage of the solution. Even more importantly, they affect the final microstructure and properties of the produced films. Specifically, the deposition and thermal processing conditions need to be fine-tuned to obtain the microstructures that will result in the desired material properties. The tuning of these processing conditions is directly dependent on the specific chemistries and routes employed.

The specific solvent used in the precursor solution and the synthesis route affect the extent of intermixing of the species, the carbon content, the temperature at which the pyrolysis of the organic content will occur, the densification and crystallization behavior, and in part stress development within the film.[51] 2-methoxyethanol (2MOE), methanol, and modifying ligands such as acetic acid have been used in reported CSD routes for processing of PZT thin films.[51] When appropriately synthesized, 2MOE-based solutions offer excellent stability, control and reproducibility of process chemistry, and exhibit minimal aging effects.[51] On the other hand, these solutions have rather long synthesis time, and the toxicity of the solvent is a major health concern.

The other prominently used chemical solution processing route is chelate-based; it is developed by Assink and Schwartz.[31] Better known as inverted mixing order "IMO", this method is based on the use of methanol as solvent, and acetic acid or acetylacetone as chelating agents. Ferroelectric thin and ultrathin films with excellent dielectric properties have been processed for a number of chemistries (e.g. lead zirconate-titanate $Pb(Zr,Ti)O_3$ (PZT) and barium titanate, $BaTiO_3$, (BT) with both the above-mentioned routes.[49] 2MOE-based route was used throughout this investigation to prepare precursor solutions for ferroelectric films, as explained in chapter 2. The main advantages of this route are its stability and simplicity with relatively short processing times.

Almost independently from the precursor solvent, CSD-fabricated film thickness varies almost linearly with the precursor solution's concentration and the number of deposited layers. Film thickness can also be tuned by the duration and speed of the spinner in the spin coating method (refer to Chapter 2 for more details). Diluting the precursor solution enables fabrication of ultrathin layers. However, ultrathin layers

deposited in a single step often result in self-assembled nanostructures, or continuous films that present a large density of pinhole defects, resulting in large leakage currents or electrical shorts. Often, increasing the number of deposited layers can result in a higher quality film (by reduction of pinhole defects) and therefore enhanced functional device yield.[52] Through at least two depositions of dilute (below 0.1M) precursor solution, functional PZT films as thin as 20 nm have been processed on platinized Si substrate as will be discussed in the next chapter.[52]

3.3 Substrate and Bottom Electrode Stack

Pb-based ferroelectric oxide thin films have been fabricated on a variety of substrates including Si, base metals (e.g. Cu, Ni), stainless steel, and single crystal oxides such as MgO, $LaAlO_3$, Al_2O_3 and $SrTiO_3$.[53-55] The choice is in part dictated by compatibility with the desired application of the thin film. The specific substrate used determines also in part the choice of the eventual bottom electrode material stack to be used. Furthermore, the substrate has also a substantial effect on the state of the residual stresses and the domain structure of the ferroelectric film, and therefore its final dielectric and piezoelectric response.[55]

A large majority of the current literature on ferroelectric oxide thin films including this work is based on platinum-coated silicon substrates. The selection of Si wafers as a substrate is in part due to the low cost and easy availability of Si wafers, as well as the ubiquity of this material in CMOS and MEMS applications.

The relatively high temperatures required for processing ferroelectric oxides require that inert materials be used as the bottom electrodes, in order to minimize substrate oxidation and interface reactions during crystallization of the ferroelectric film. Therefore, common choices include Pt among metals, or conductive oxides such as iridium oxide (IrO_2), strontium ruthenate ($SrRuO_3$) and indium-tin oxide (In_2O_3-SnO_2).[56,57] Pt was used in this work as bottom electrode material.

To date, many of the technologically relevant ferroelectric oxides, especially for electromechanical applications, are Pb-based perovskite compositions.[32] However, the high reactivity of Pb with silicon can result in formation of lead silicate in the substrate and fluorite or pyrochlore type secondary phases in the film; it can also cause delamination from the substrate, and cracking of films thicker than a couple of hundred nanometers.[58] Hence Pb diffusion barriers are introduced in the bottom electrode stack; the most common such barrier is a SiO_2 layer of 400 nm to 1µm thickness. However, adhesion problems between Pt and SiO_2 require that intermediate layer(s) be introduced in order to improve adhesion and to avoid Pt delamination from the substrate as a result of the thermal treatment processes. The most common such adhesion layer is a thin layer (20 to 40 nm thick) of partially or fully oxidized Ti. The resulting Pt/Ti/SiO_2//Si structure is commonly referred to as ‘‘platinized silicon’’. Unfortunately, while TiO_2 is a good adhesion layer, Ti is prone to diffusion at high processing temperatures. Alternative materials such as wurtzite-structured ZnO have been also suggested for use as an adhesion layer.[59]

Platinized Si wafers are also prone to show Pt abnormal grain growth (Pt hillocks) when they are used for relatively longer periods at higher crystallization temperatures

resulting in larger local stresses. For example Pt hillocks have been observed for thermal treatment at above 900°C for longer than a few minutes. These defects create local electric field concentration spots (local reduction in ferroelectric film thickness), and therefore result in reduction of the overall functional device yield, especially in thinner ferroelectric films.

3.4 Processing Conditions: Temperature and Environment

CSD processing typically involves two heat treatment steps: pyrolysis and crystallization. Depending on the material system and the concentration and type of the solvent used in the precursor solution, pyrolysis requires exposure to temperatures from 200°C to 450°C for periods ranging from 30 seconds up to a few minutes. Organic removal accompanied by major volume shrinkage (up to 50% to 70% in thickness direction) in the deposited gel occurs during this step.[51] Pyrolysis temperature and environment can strongly affect the final texture of the film (see section 3.5.2), as partial nucleation of crystallized (desired and secondary including intermediate) phases can start during pyrolysis.

Full crystallization takes place during annealing at higher temperatures (700°C for PZT) following the pyrolysis step. In most cases, one to four film layers are deposited and each is pyrolyzed separately, before a single crystallization step is performed, in order to obtain an approximate thickness of up to 250 nm (with a 0.4M precursor solution).[37,49] The multiple layers' concomitant crystallization is implemented both for the sake of reducing processing times and in order to avoid large removal of cationic

species (such as Pb for PZT and PMN-PT) that might be highly volatile at crystallization temperatures.

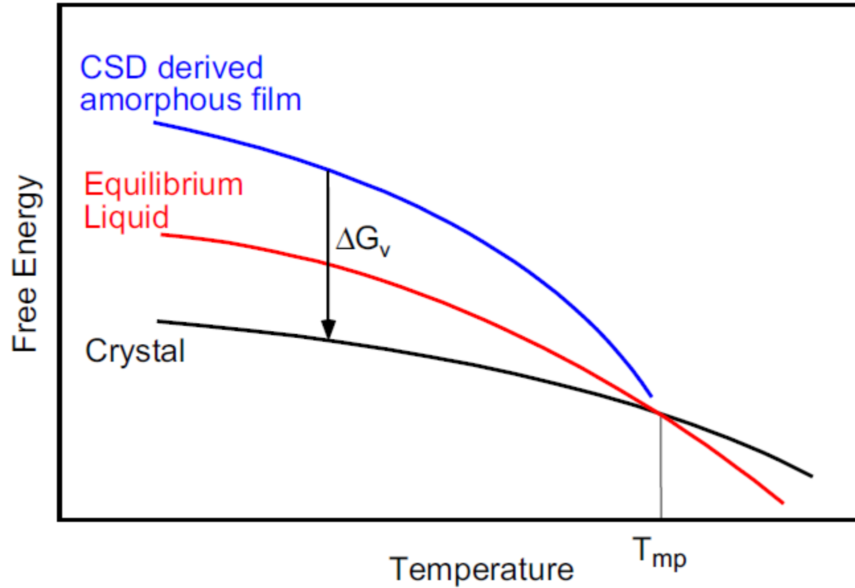

Figure 3.1 Schematic diagram of the free energies of a CSD derived amorphous film and a crystalline perovskite phase. ΔG_v is the thermodynamic driving force for crystallization.[51]

The heat treatment profile directly affects the grain size and film densification (section 3.5.3), as well as the thermal residual stress development in the films. This profound impact can be understood in the framework of the thermodynamic driving force for crystallization. The thermodynamic driving force, ΔG_v, for transformation of the amorphous (as pyrolyzed) film into crystalline ceramic is provided by the difference in free energy between the two phases as shown in Figure 3.1.[51] This driving force plays a significant role on the type of the nucleation events that will be active and dominant, which in turn affects the final microstructure of the film. While this information does not necessarily provide the transformation pathway the amorphous film undergoes, it is useful in understanding the role that the driving force can have on the transformation

process. For example, crystallization at higher temperatures (closer to the melting point) results in a lower driving force for the transformation, as the free energies of amorphous and crystallized phases are closer to each other.[51]

The energy barrier for both homogeneous and heterogeneous nucleation events conversely depends on the thermodynamic driving force:

$$\Delta G^*_{homo} = \frac{16\pi\gamma^3}{3(\Delta G_v)^2} \qquad \text{Equation 3.1}$$

$$\Delta G^*_{hetero} = \frac{16\pi\gamma^3}{3(\Delta G_v)^2} f(\theta) \qquad \text{Eqaution 3.2}$$

$$f(\theta) = (2 - 3cos\theta + (cos\theta)^3)/4 \qquad \text{Equation 3.3}$$

where γ is the interfacial energy, ΔG_v is the driving force for crystallization, i.e., the free energy difference per unit volume for the amorphous film-crystalline film transformation, and $f(\theta)$ is a function related to the contact angle, θ, according to equation 3.3 for a hemispherical nucleus.

The energy barrier for heterogeneous nucleation (i.e. nucleation at the interface or on the surface) is lower than that for homogeneous nucleation (nucleation in the bulk of the film) by a factor dependent on the contact angle between the film and the heterogeneous nucleation site. Considering all the above factors, during heat treatment, the thermal energy made available at each temperature defines which nucleation events will take place, and thus directly influences the film's microstructure.

In thin films where the crystallization temperature is only a fraction of the ceramic melting point, the crystallization driving force is large (see Figure 3.1), and

therefore homogeneous nucleation is as probable as heterogeneous or interface nucleation, usually leading to polycrystalline, equi-axial grains. Such is, for example, the case of many barium titanate, BT, films processed on platinized Si substrate (Figure 3.2).[60] However, intermediate flourite (pyrochlore) phase formation reduces the thermodynamic driving force by introduction of an intermediate step in the free energy gap.

For films that transform with small driving forces, the energy barrier heights for different nucleation events are large and are separated to a greater extent. This leads to interface nucleation for PZT film on platinized Si substrates, where interfacial nucleation is preferred to bulk nucleation, resulting in columnar assembly of grains (Figure 3.2).[26,61] Heterogeneous nucleation can, however, occur also at the film's surface under appropriate heat treatment conditions. In films that are heat treated in conventional furnaces or by rapid thermal processing tools, competing interface and surface nucleation can result in a reduction of crystallographic texturing at higher film thicknesses and therefore lower dielectric and piezoelectric response (See section 3.5.2). For a well-processed precursor solution, the absence of large defects in the pyrolyzed film means there are not many heterogeneous or bulk nucleation sites.

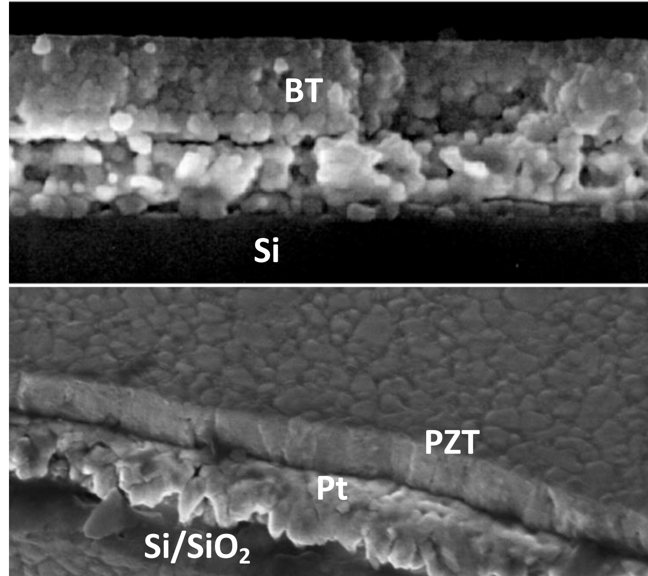

Figure 3.2 SEM micrographs of typical thin film microstructures for BT and PZT films prepared by CSD on Si substrate. Top: The BT film displays both interfacial nucleation and nucleation within the bulk of the film, corresponding to a preferred homogeneous nucleation mechanism.[51] Bottom: The PZT film displays only heterogeneous nucleation at the Pt bottom electrode interface (the white surface layer is the Pt top electrode) resulting in columnar grain structure.

It is important to emphasize that the annealing ramp rate is also particularly important for materials with a wide range of nucleation energies, especially at lower crystallization temperatures. In rapid thermal annealing, the physical processes leading to densification and crystallization of the film are delayed to higher temperatures compared to conventional low ramp rate methods such as annealing in conventional furnaces. Conversely, in low ramp rate annealing methods, nucleation and growth start at lower temperatures and continue as the temperature rises. This wide processing temperature window often results in more than one type of nucleation, in different grain growth rates that govern the final microstructure of the film, and ultimately leads to randomly textured films.[51] In addition to the texture, the crystallization ramp can affect the density of the film as well, through other factors such as completion of organic removal or densification

influence the film density as well. More discussion on this subject can be found in section 3.5.3.

The crystallization atmosphere also has a strong effect on the crystallographic texture and phase purity of the PZT thin films. Phase content is particularly affected for materials such as PZT, where crystallization is mediated by an intermediate phase formation. For example, a recent study showed that exposure to an oxidizing atmosphere during crystallization of PZT thin films can mitigate formation of intermetallic Pt_3Pb and can promote the formation of pyrochlore phase.[62] Conversely, exposure to reducing atmospheres can stabilize Pt_3Pb and stabilize the formation of the perovskite phase.[62]

For material systems containing volatile cations such as Pb, intense gas flow might also promote increased evaporation of the volatile species, resulting in secondary phase formation in proximity of the film surface. Careful control of Pb content is critical to the phase purity of the PZT thin films, which in turn drastically affects the films' dielectric and piezoelectric performance.

3.5 Microstructural Development of PZT Thin Films

With a strong tie between microstructural characteristics and functional properties, it is vital to control phase purity, film density, crystallographic texture, and chemical homogeneity of the ferroelectric oxide thin films in order to achieve the best properties. Crystallization of ferroelectric oxide films, specifically those with perovskite structure such as PZT, is usually nucleation limited, as growth processes are typically extremely fast (one to a few seconds).[61,63] Hence the final microstructure of the films is often determined by the processing conditions during the lower temperature, and ramp-up

part of the thermal treatment (see section 3.4). The following sections discuss in detail the development and control of some of the most common microstructural characteristics of PZT thin films processed by CSD.

3.5.1 Phase purity

Phase content and distribution play a critical role in determining the final properties of ferroelectric oxides. For example, presence of secondary paraelectric phases is detrimental to both the dielectric and piezoelectric responses of PZT thin films. The crystallization pathway and the formation of intermediate phases, the stoichiometric control of the volatile species (Pb) and chemical interactions between film and substrate during the heat treatment are the major factors determining the final phase content of the PZT thin films.[51,64]

In perovskite-structured, $PbTiO_3$-based, solid solution ferroelectric films such as PZT, crystallization often proceeds through an intermediate disordered fluorite phase, which in the case of sufficient cation ordering, sometimes exhibits pyrochlore structure.[49] This intermediate phase subsequently transforms into the thermodynamically stable perovskite phase at higher temperatures.[49] However, the fluorite phase can become stabilized in proximity of surfaces and interfaces where the loss of high-volatility cations (Pb) is more accentuated. Ferroelectric compositions with such highly volatile cations are often over-batched for these elements with respect to stoichiometric requirements. The specific amount of over-stoichiometric Pb is dependent on the composition, the thickness of the single layer being pyrolyzed, the number of layers crystallized together, as well as the thermal treatment conditions. These variables determine not only the diffusion length-

scale for the cations but also the amount of surface cation volatility; they therefore determine the surface Pb loss during thermal treatment processes.[49] Pb excess content of 20 mol% was used for 0.2M and 0.4M PZT 53/47 precursor solutions, and 40 mol% for 0.1M solutions.

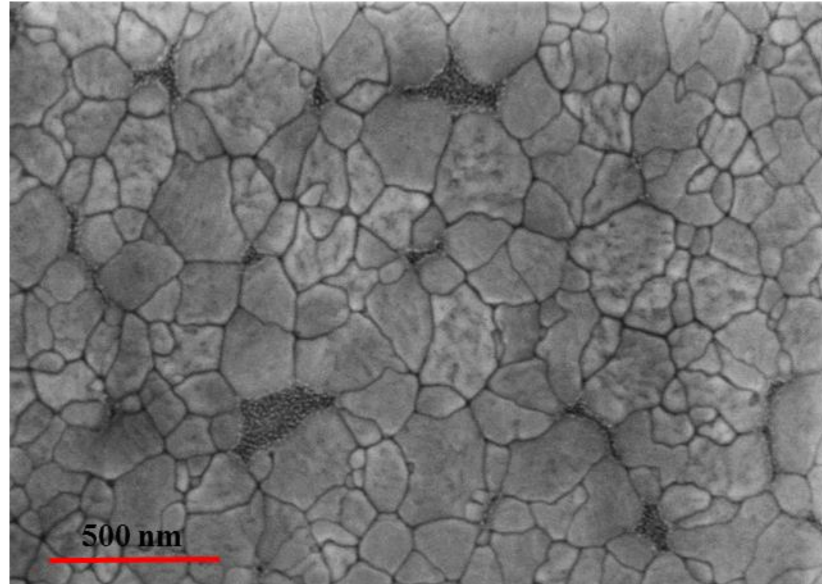

Figure 3.3 Secondary pyrochlore phase observed on the surface of a 200nm-thick PZT 53/47 film observed on SEM plain view image. Clustered small grains, mostly decorating the grain boundaries and/or on the film surface, typically of different contrast with respect to the larger perovskite grains represents the pyrochlore.

Pb deficiency generally leads to unwanted secondary fluorite phases (e.g. $A_2B_2O_{7-x}$) remaining in the final microstructure of the film (Figure 3.3) The presence of such secondary phases severely degrades the final dielectric and piezoelectric response of PZT films.[49] This is due to the relative ease with which intermediate fluorite phases can accommodate greater deviation from stoichiometry with respect to the perovskite structure. Conversely, excess Pb can result in the PbO accumulation at the grain boundaries or on the surface, as shown in Figure 3.4; this adversely affects the films'

breakdown field and resistivity. Surface PbO_x is often removable with a quick acetic acid etch.

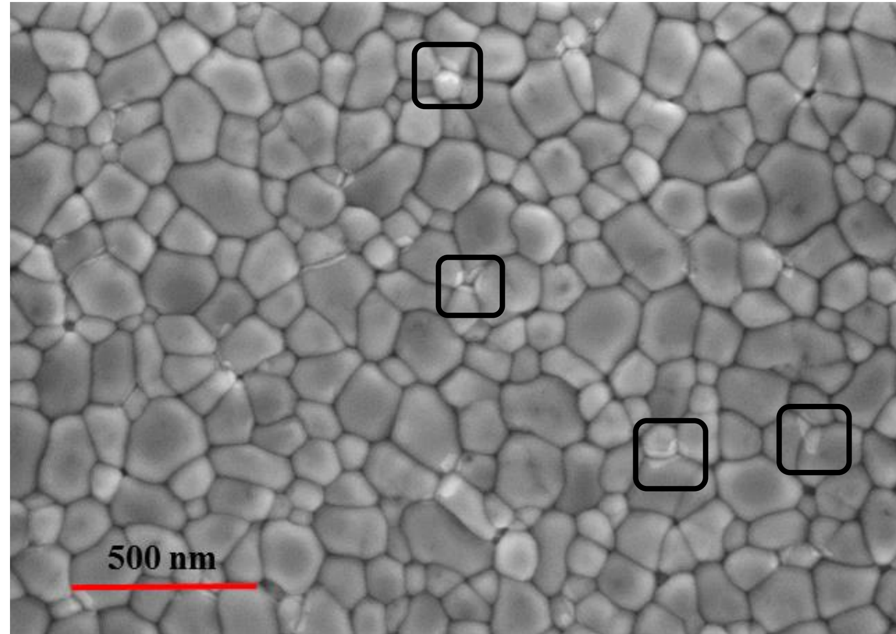

Figure 3.4 PbO inclusions in small amounts observable as secondary phase with slightly lighter contrast in the SEM image, accumulated at the grain boundaries between PZT grains.

Secondary phases are not always easy to identify. They are often identified via a combination of X-ray diffraction (see Figure 3.4), electron microscopy and characterization of the dielectric and/or piezoelectric responses of the films. Specifically, X Ray diffraction is inadequate for identification of fluorite phase or PbO inclusions,[65] if they are of low crystallinity, or if they are present in small volumes (approximately <5%). The existence of clustered small grains, mostly decorating the grain boundaries and/or on the film surface, typically of different contrast with respect to the larger perovskite grains, is often an indication of secondary phases in scanning electron microscope (SEM) images (Figure 3.3). Degradation in the dielectric and piezoelectric properties is expected

to occur at the same time. Secondary phases, such as lead oxide, can also result in increased conductivity and dielectric loss, especially when present at grain boundaries throughout the film thickness.

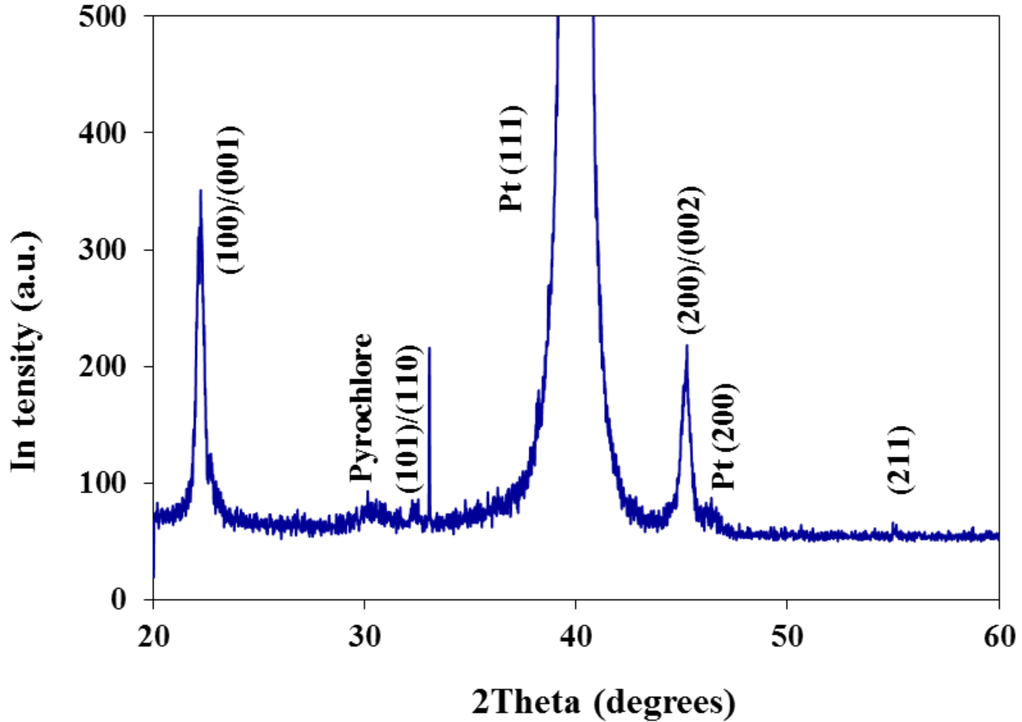

Figure 3.5 XRD pattern of a 100 nm thick PZT film with some amount of secondary pyrochlore phase shown as a hump at ~30°. This is caused by insufficient Pb content in the precursor solution (only 10% excess lead was used here).

Chemical interactions between the film and the bottom electrode stack also play an important role in the phase content and texture development of ferroelectric films. Pb diffusion through the Pt bottom electrode and into the adhesion layer in platinized silicon substrates results in additional Pb depletion; in severe cases this can lead to cracking and/or delamination from the substrate.[49] $Pt_{5-7}Pb$ is a metastable intermetallic phase that can form under reducing conditions, such as those often experienced at the film–electrode interface during heat treatment. Although this intermetallic phase disappears at higher

temperatures during annealing, it can affect the films' texture development.[64,66] Similarly, Ti from the adhesion layer can diffuse through the Pt electrode to form a Pt_3Ti intermetallic phase at the electrode–film interface, affecting the chemical composition as well as the texture development of the film.

3.5.2 Texture and Crystallographic Orientation of the Films

Dielectric and piezoelectric response of ferroelectric materials are often strongly anisotropic. As a result, in order to optimize dielectric or piezoelectric response it is vital to control ferroelectric thin films' crystallographic texture. In single crystal $PbTiO_3$-solid solutions (e.g. PZT or lead magnesium niobate-lead titanate, PMN-PT), the largest piezoelectric response (d_{33} or e_{31}) is observed on the rhombohedral side of the morphotropic phase boundary (MPB), when the crystal is cut and poled along the [001] direction (pseudo cubic indices) as shown in Figure 3.6. Similarly, in textured thin films of comparable composition, larger piezoelectric response are observed for films with [001] texturing with respect to [111] or randomly textured films.[1]

Crystallographic texturing in thin films is a direct consequence of nucleation and growth during the heat treatment process, and therefore depends on many factors influencing the competing heterogeneous and homogeneous nucleation energies, as well as the preferential growth directions. Such factors include but are not limited to the substrate and bottom electrode materials, the presence of eventual seed layers, the formation of possible intermediate phase/s, the heat treatment profile, the local and global chemical composition, the oxygen and organic content in the amorphous film, and the crystallization environment.[62-64,66]

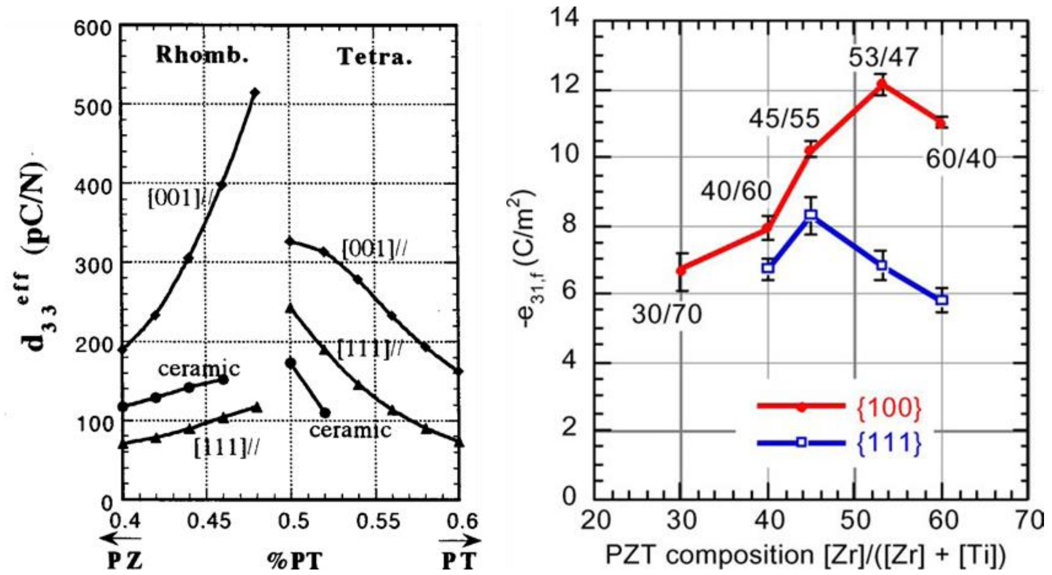

Figure 3.6 Dependence of the piezoelectric response of PZT ceramic and single crystal (Left) and thin films (Right) on the composition and crystallographic orientation.[1]

CSD processing of many ferroelectric oxides is strongly nucleation controlled, due to fast growth kinetics.[1] Therefore a careful control of the nucleation processes can result in textured, columnar grains. Choosing a single crystalline oxide substrate and/or textured electrode that has a good lattice match with the ferroelectric perovskite can result in wide processing windows for textured ferroelectrics. (100)-textured PZT thin films have been processed by CSD, leveraging thin sputter-deposited $PbTiO_3$ (PT) or PbO seed layers.[1] Similarly, the use of TiO_x seed layers can enhance nucleation of (111) textured PZT films,[1] by further reducing the heterogeneous nucleation activation energy.

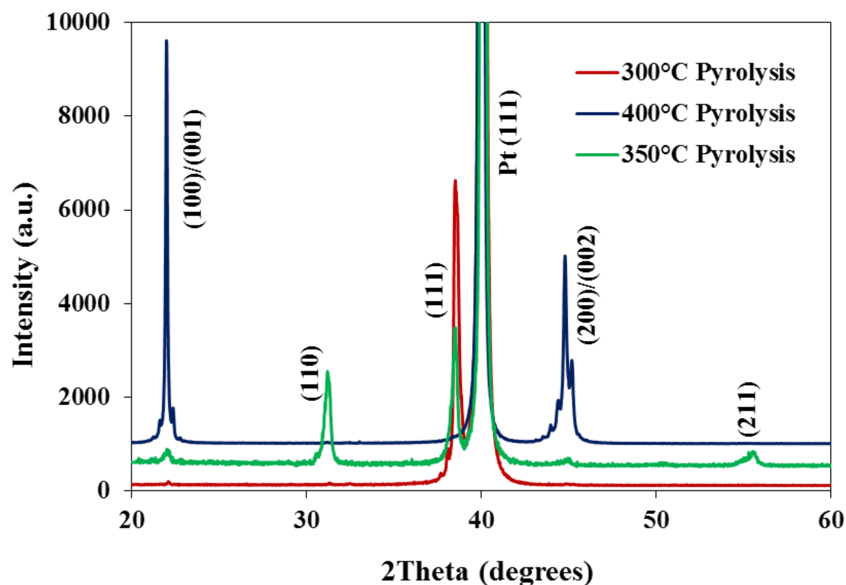

Figure 3.7. Effect of Pyrolysis temperature on the texture of PZT thin film prepared on platinized silicon wafer. All films are ~300nm-thick.

Ferroelectric oxides such as PZT on platinized silicon substrate often acquire the texture of the underlying electrode (i.e. (111)PZT on (111) Pt), through heterogeneous nucleation at the interface.[1] In general, the texture of PZT films on platinized silicon substrate is strongly correlated with the pyrolysis temperature, as shown in Figure 3.7. Pyrolysis at 300°C for 1 min. on a hotplate in the air results in highly (111)-oriented films, while pyrolysis at a temperature of 400°C yields highly (100)-textured film when similar annealing time and temperature are used (700°C in the RTA, 60°C/sec ramp rate for 1 min. in air atmosphere). Mixed orientation was observed for pyrolysis temperatures between this range (~350°C) or higher than 450°C.

Almost similar dependence of the crystallographic texture on the pyrolysis temperature was observed for CSD-derived PZT films based on an IMO precursor solution (Figure 3.8); there were some temperature range discrepancies, possibly due to

temperature measurement error or to different amounts of solvent being removed in various solutions during pyrolysis. At lower pyrolysis temperatures, texture development is controlled by heterogeneous nucleation (lower activation energies), resulting in (111)-oriented films for films on (111) platinized Si (Region 1 in the figure). Formation of fluorite crystallites at higher pyrolysis temperatures results in a growth-controlled final texture, leading to highly (100)-textured films when <100> is thermodynamically the fastest growth direction[61] (Region II).

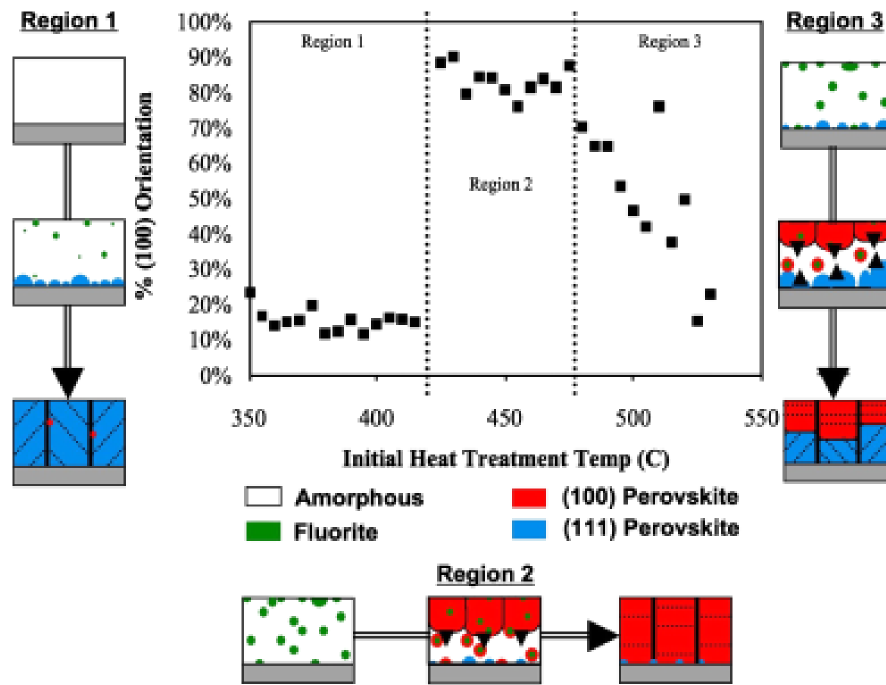

Figure 3.8 Effect of pyrolysis temperature on the orientation of PZT 40/60 films after identical crystallization at 7001C and proposed mechanism(s) behind the texture development.[49]

At even higher pyrolysis temperatures, wide-spread nucleation at the electrode surface as well as within the bulk of the film results in randomly oriented grains (Region III).[49] Such pyrolysis temperature control can be used to texture thin PZT films (up to 60 nm thick for each crystallized layer). Such thin and highly oriented layers can be used as

templates to texture thicker films through subsequent layer deposition and heat treatment.[26,37]

As mentioned earlier in section 3.4, the crystallization atmosphere also has a strong effect on the texture development in PZT films. The presented results are all obtained in air atmosphere. A small amount of reducing environment such as N_2 drastically reduces the level of (100) orientation in the film as shown in Figure 3.9.

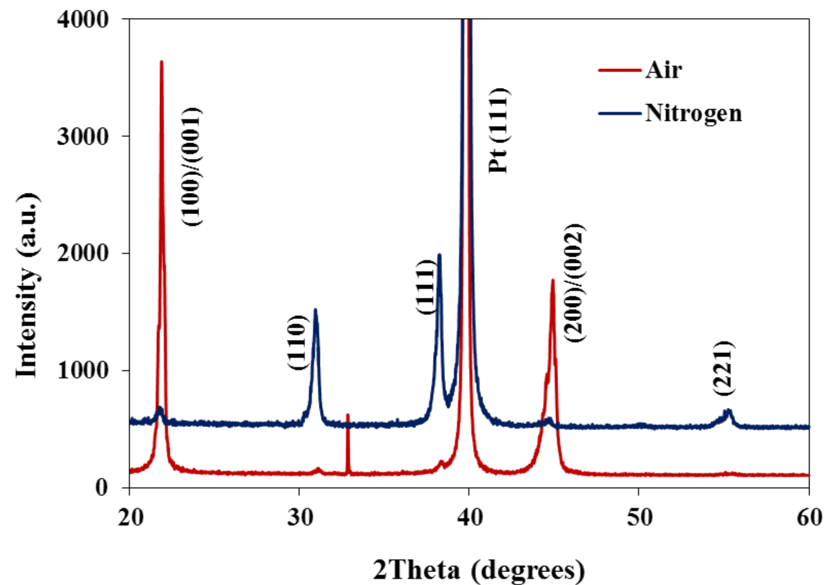

Figure 3.9. Effect of crystallization environment on the texture of PZT thin film prepared on platinized silicon wafer. All films are ~300nm-thick and pyrolyzed at 400°C.

Another important factor in the development of the texture in PZT films is the thickness of the crystallized layer in each annealing step. Depending on the number of deposition/pyrolysis steps before annealing and also the molarity of the precursor solution, this thickness varies from ~30 nm for single layer 0.2M 2MOE-based solution, up to ~240 nm for a stack of 4 deposited layers with 0.4M solution. Control of the film texture via control of the pyrolysis process is most effective for thinner films up to 60nm.

Such a thin and textured PZT film can be then used as a seed layer to template the texture of the rest of the film up to desired final thickness,[26] or even to control the texture in other perovskite ferroelectric oxide films such as PMN-PT.[61]

Additionally, heterogeneous seed layers can also be used as templates to control the texture of the film. Ideally, the use of homogeneous seed layers, i.e. of the same composition or a subset composition of the ferroelectric material is preferred: for example, PT and TiO_x are easily incorporated into PZT or PMN-PT films after crystallization of the ferroelectric films. As CSD is a layer-by-layer processing method, a careful composition selection for the precursor solution/s can result in very limited chemical composition variation of the final film, even locally. For example, in order to compensate for the presence of additional PT, a slightly more Zr-rich (with respect to the target PZT composition) and over-stoichiometric Pb-content PZT precursor solution can be used for the first processed layer/s. The composition of the precursor solution used for the subsequently deposited layers is then stoichiometric with respect to the desired Zr/Ti ratio.

3.5.3 Grain Size and Porosity

The average grain size of ferroelectric oxide thin films processed by chemical solution processing is typically between 50 and 200 nm, which is well below those observed in bulk ceramics.[1] In fact, the grain size of ceramic materials is strongly affected by the nucleation rate and the mass transport characteristics during crystallization. As mentioned earlier in section 3.4, typical crystallization temperatures employed in thin film processing are significantly lower than ceramic sintering

temperatures. At these lower temperatures, the slow solid-state diffusion mechanisms cannot provide the transport needed to obtain crystalline quality and grain growth that is similar to those available in bulk ceramic processing. The resulting disorder associated with smaller average grain size, i.e. higher percentage of disordered, grain boundary volume, often results in reduced electromechanical and dielectric response of the film.[60] Similarly, the lower processing temperatures in thin films can also affect densification.

In general, different mechanisms can contribute to the formation of pores in thin films. The presence of residual organic material after pyrolysis, followed by rapid crystallization or rapid grain growth (i.e. without sufficient time for densification) and also air entrapment between the grains, may result in formation of porosity between or within the grains, as seen in Figure 3.10. This will be discussed in more detail in chapter 6.

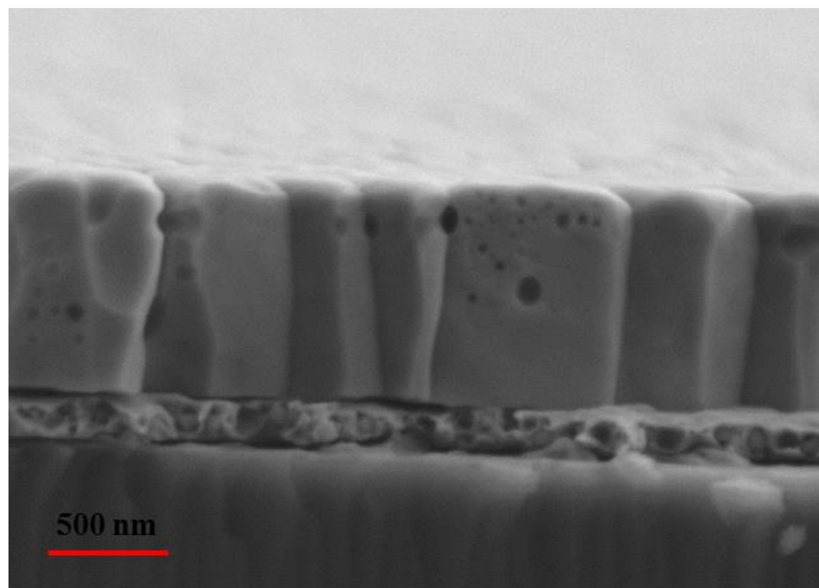

Figure 3.10 Porosity observed between and within the grains in a 1μm thick CSD-derived PMN-PT film.[61]

Different approaches have been used to increase the grain size and density of the CSD processed films. The appropriate choice of the bottom electrode or seed layer, the use of higher annealing temperatures, the incorporation of dopants that promote material flux (liquid phase-assisted growth), as well as better control of the film stoichiometry have been successfully used in increasing the average grain size in PZT- and BT-based thin films.[28,60,61] In the following paragraphs we briefly discuss each of these methods.

In many polycrystalline films, the lateral grain size is controlled by the grain size of the underlying electrode or seed layer, especially when these represent heterogeneous nucleation sites. For example, the average grain sizes for ferroelectric oxide films (such as PZT or PMN-PT) grown on platinized Si substrates is often in the range of 50 to 200 nm, and has been shown to directly correlate to the fine grain size (~50 nm) of the Pt bottom electrode.[1] Textured PMN-PT films show a seed layer dependence on the average grain size, with larger grains obtained on PT than on the PZT seed layer (see chapter 6).[61] Similarly, it is possible to grow quasi-single crystalline quality films on single crystalline oxide substrates via CSD, as discussed in section 3.4.

Increasing annealing temperature facilitates mass transport, and therefore has been leveraged for grain growth in thin films.[28] However, higher processing temperatures result also in higher in-plane thermal residual stresses in thin films, with thermal expansion coefficient mismatch with respect to the substrate. The maximum processing temperature for platinized Si substrates is approximately 850°C: higher processing temperatures often result in cracking, delamination and/or excessive curvature of released structures in the case of patterned films for MEMS devices.[61,67] Platinized Si substrates using ZnO adhesion layers have also been reported for annealing processes up to 1000°C;

however, problems pertaining to the Si substrate, such as those caused by TEC mismatch with film, can persist. This is in part circumvented by use of base metal substrates, which allow processing temperatures in excess of 1100°C. As discussed in section 3.3, such substrates require a close control of processing atmosphere in order to avoid interfacial phase formation.

The temperature profile during annealing, and especially in the ramp up section, also affects the formation of porosity in PZT thin films. As it was discussed in section 3.4, higher ramp rates, and a slight overshoot in the ramp up temperature profile, delays the grain growth process into higher temperatures (Figure 3.11). This in turn makes more diffusion and cation mobility available during these processes, which leads to the elimination of pores and to higher film density as shown in Figure 3.12.

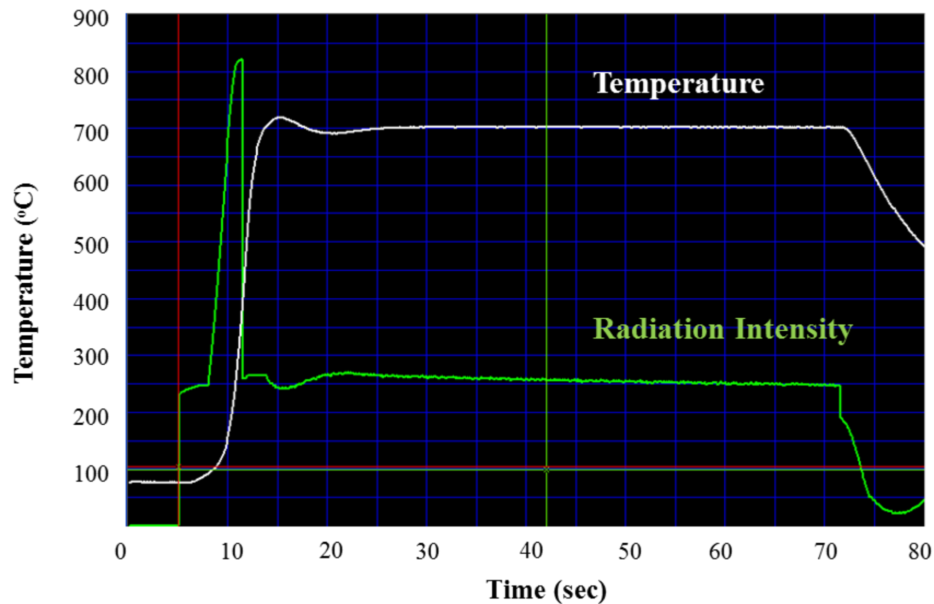

Figure 3.11. Annealing temperature profile used for PZT thin films in rapid thermal annealer. Nominal crystallization time and temperature is 1 min and 700°C.

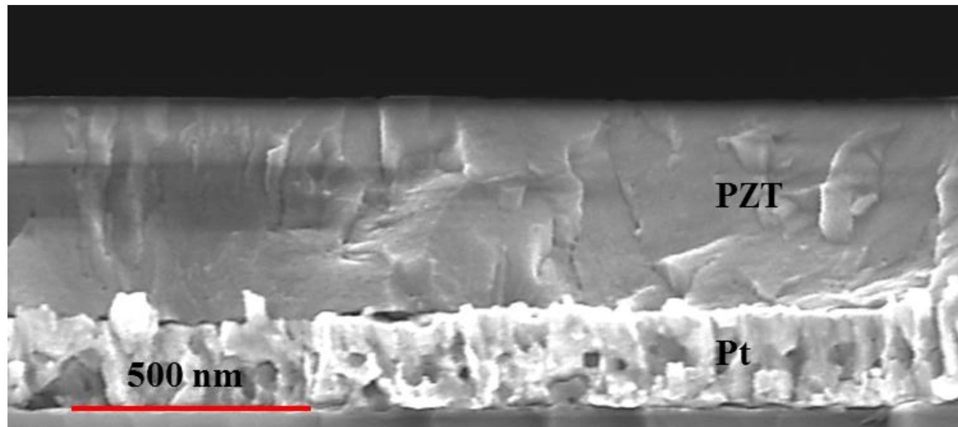

Figure 3.12 Elimination of most of the porosity in PZT film on platinized Si substrate using the annealing temperature profile in Figure 3.8.

Incorporating dopants that promote diffusion and/or material flux is another approach to attain grain growth and to avoid porosity. The presence of a slight amount of liquid phase during annealing dramatically enhances grain growth, densification, and overall crystalline quality of the film.[60] A limited concentration (<5%) of barium-borate, for $BaTiO_3$ thin films, and larger amount of NiO and PbO for PZT films have been shown to result in grain growth and densification due to the liquid phase formation during crystallization. Additionally, larger grain sizes can be obtained by better control of Pb content and by reduction in grain boundary drag associated with excess PbO at the grain boundaries, for Pb-based compositions.[28]

3.5.4 Chemical Homogeneity

Ferroelectric oxides have complex chemical composition, often with 3 or more cation species. Homogeneous cation distribution is critical in achieving large dielectric and piezoelectric responses in ferroelectric thin films.[59,68] However, due to the sensitivity

and the sampling volume limitations of available characterization techniques, homogeneity in thin films is often routinely assumed rather than confirmed.[49]

A variety of phenomena may lead to chemical heterogeneities in CSD-derived ferroelectric films, and in fact, local chemical compositions within PZT films are far from stoichiometric. For example, cation clustering is common in precursor solutions and/or after organic removal (pyrolysis) in the amorphous phase.[69] Furthermore, the nucleation process in many solid solution ferroelectric films, such as PZT or PMN-PT, induces compositional heterogeneity.[70] This is in part due to the relatively low diffusion rates of many cations under practical annealing conditions for thin films, combined with different driving forces associated with various chemical reactions especially in ferroelectric solid solutions.[49]

Specifically for PZT films with composition close to MPB, such cation gradients lead to local phase switching (e.g. between rhombohedral, R, and tetragonal, T, for PZT53/47). This effectively translates into only a small portion of the film at the target MPB composition with maximized functional properties. Further investigation on this subject is referred to chapter 5 of this thesis, where the chemical homogeneity in PZT films is further investigated and is used toward processing of superlattice-like films with strong piezoelectric and dielectric response.[36]

Chapter 4

Effects of the Crystallite Size on the Functional Properties of PZT Ultrathin Films; Thickness Dependence

This chapter is dedicated to the investigation of the effects of the film thickness (crystallite size) on the dielectric and piezoelectric response of PZT ultrathin films. Highly (100)-textured PZT films (Lotgering factors ≥ 90%) with thicknesses ranging from 20 to 260 nm were grown on platinized Si substrates were examined. Due to the columnar microstructure of these films the critical dimension of the ferroelectric is represented by the thickness rather than the lateral grain size, where the latter is invariant across the samples. Ferroelectric hysteresis, low field dielectric permittivity and nonlinear dielectric response as well as converse longitudinal piezoelectric response, $d_{33,f}$, of the ultrathin films were studied at 1 kHz. The measurements revealed the existence of a critical film thickness, ~50 nm, below which the extrinsic contributions to the dielectric response are almost completely suppressed. Piezoelectric response of the films also showed a significant (~50%) drop at the same critical thickness. Suppressed extrinsic contributions are attributed to significant reduction in domain wall population and mobility. In addition to the strong substrate clamping, absence of ferroelastic domain walls below a certain grain size due to elastic energy minimization, are proposed as the main contributors to the existence of such a critical film thickness.

4.1 Introduction[1]

Dielectric and piezoelectric properties of ferroelectric materials in thin film and micro- and nano-structure form are influenced by their microstructure, crystalline quality and orientation. Furthermore, the material response is strongly dependent on the physical size. In fact, ferroelectric thin (thickness < 1μm) and ultrathin (thickness < 200nm) films on rigid substrates have often inferior properties compared to the bulk ceramics and suffer from severe thickness-dependent property degradation.[28,71] Grain size variation,[28,29,71-74] existence of interfacial "dead layers",[75-80] high field space charge depletion layers,[81] stoichiometric defects and variations,[68,82] and residual stress induced by substrate clamping[8384-88] are reported as causes of the "size effects" in ferroelectric thin films. However, presence of a low permittivity interfacial layer, and high levels of residual stress clamping domain wall motion are recognized as some of the most significant contributors to the reduced dielectric and electromechanical response in submicron-thick ferroelectric films.[89]

Dielectric and piezoelectric response of the ferroelectric material are comprised of the average response of the single domains present (intrinsic response) and the contributions from the motion of the domain walls and eventual phase boundaries (extrinsic response).[9] There are size effects associated with both intrinsic and extrinsic contributions to the response of the ferroelectric thin films. Intrinsic size effects are limited to thicknesses of a few nanometers, and have been extensively studied both by theoretical and experimental approaches.[90] At larger thickness values (tens to hundreds of

---

[1] The content of this chapter is mainly based on work published in the Journal of Applied Physics.

nanometers) the concept of “interfacial dead layer” has been proved particularly successful to describe another intrinsic source of dielectric degradation. Interfacial “dead layer” is referred to as a low permittivity layer parallel to the electrodes and at the interface of the film and the electrode(s), usually modeled as a parasitic capacitance acting in series with the “bulk-like” remainder of the film.[91-94] This can lead to a reduction of the overall dielectric and piezoelectric response of the metal/ferroelectric oxide/metal structure. The origin of the dead layer has been for long debated to be intrinsic or extrinsic, and most recently has been shown to be an intrinsic feature of the electrode-dielectric boundary, dependent on the specific ferroelectric and electrode material combination as well as surface termination of the ferroelectric at the interface.[91,95]

4.1.1 Extrinsic Sources of Size Effects

Extrinsic size effects have been much less studied and have been mostly limited to film thicknesses ranging from hundreds of nanometers to well above 1 micron. In general, for thickness $\leq 1\mu m$, decreased extrinsic contributions due to the reduced population and mobility of the domain walls can be very significant. Domain density and domain wall mobility are strongly affected by the size of the ferroic phase.[71,96] In particular, formation of ferroelastic domain walls are not energetically favorable in grains below a critical size.[97] Ferroelastic domain walls have been reported to disappear in perovskite ferroelectrics at grain sizes $\lesssim 100nm$[71]. Minimum calculated grain size of 21 nm is reported for twinning in PZT ceramics, based on geometrical considerations. Higher values are expected if further interfacial or strain energy terms are to be included.[98] Nagarajan and coworkers[99] for example, have documented the presence of

ferroelastic domains in 60 nm thick epitaxial PZT films (Zr/Ti=20/80) on $LaAlO_3$ substrate, while they were absent in thinner PZT films (~30 nm).

This chapter focuses on extrinsic size effects and their influence on the dielectric and piezoelectric responses of the films at such a thickness range, as this would shed some light on the performance limitations in small scale ferroelectric thin film applications. Specifically, low-field and nonlinear dielectric response, ferroelectric hysteresis, as well as piezoelectric measurements are used to study the thickness-dependent dielectric response of highly (100)-oriented, $Pb(Zr_{0.53}Ti_{0.47})O_3$ (PZT) films of thickness ranging between ~20 and 260 nm.

4.2 Experimental Procedures

Sol-gel precursor solutions of PZT nominal composition with 10 and 20 mol% excess lead ($Pb_{1.1}(Zr_{0.53}Ti_{0.47})O_3$ and $Pb_{1.2}(Zr_{0.53}Ti_{0.47})O_3$) were prepared based on a 2methoxyethanol(2MOE)-route, as described in Chapter 2. The solutions were adjusted at 0.1M or 0.2M concentration, and dispensed through a 0.1μm filter onto platinized silicon wafers.

To study the thickness effects on the material properties, it is imperative to obtain films with similar microstructural characteristics such as grain size distribution and crystallographic texture in the required thickness range. To achieve this goal, several processing conditions were used, as summarized in table 4.1. The best yield was obtained employing the processing conditions specified as series A, in which the solution with 10% excess Pb was spun at 3000 rpm for 30 s. The samples were then pyrolyzed on a hot plate at 400˚C for 30 s and subsequently crystallized in a rapid thermal annealer (Solaris

75, Surface Science Integration, El Mirage, AZ.) at 700˚C for 1 minute. Additional, multiple deposition and pyrolysis steps (from 1 up to 10 layers, depending on the final thickness of the film), followed by a single, final annealing at 700˚C for 5 min were used to obtain films of 50 nm or higher thickness. Successful processing of uniform films thinner than 50 nm required higher number of deposition steps with at least 2 annealing steps to avoid pinhole defects. More deposition steps can increase the electrode yield due to the reduction of defects and pinholes in the resulted film, as also reported by Brennecka et al.[52] Therefore, for films thinner than 50 nm, a 0.1M solution was used in a procedure similar to the one described for series A.

Table 4.1 Thermal processing conditions for the samples characterized in this study.[26]

Series	Solution Concentration/Excess PbO	Pyrolysis	Final Crystallization
A	0.1-0.2M/10 mol%	400°C×30s	700°C×5min
B	0.2M/20 mol%	400°C×30s	700°C×5min
C	0.2M/ 10 mol%	400-450°C×1-3min	700°C×1min

4.3 Results and Discussion

4.3.1 Film Microstructure and Texture

Crystallographic orientation and grain size can affect both intrinsic and extrinsic dielectric response in ferroelectric materials.[8,14,28,100] In order to limit the sources of size effects in our films, we strived to keep the films' microstructural characteristics and texture invariant within the thickness range studied. This was achieved by controlling the amount of excess lead, pyrolysis temperature, crystallization atmosphere and ramp rate.

As discussed in chapter 3, all the above factors have been previously reported to influence the orientation, as well as the final properties of sol-gel derived PZT films.[63,66,101]

A thin layer of highly (100)-oriented PZT film, as explained in section 3.5, was first deposited on the substrate. This layer was used as a nucleation layer to texture the rest of the film in a single and final crystallization step. Using a "homogeneous seed layer" eliminates possible stoichiometric deviations caused by heterogeneous seed layers such as PbO or $PbTiO_3$. Furthermore, use of a very thin PZT layer limits the amount of Pb in proximity of the Pt electrode during crystallization. This reduces deleterious interactions between the Pb and bottom electrode stack, including intermetallic secondary phase formation[102] and local delamination[103] as discussed in chapter 3.

A typical X-ray diffraction spectrum of a representative of the films in series A is shown in Figure 1. Pseudo-cubic indices are used to label the peaks. X-ray data showed perovskite structure, with strong (100) preferential orientation. Lotgering factors of all of the series A films calculated for {100} texture ranged from 90% to 95%. All other films had (100) Lotgering factors above 88.5% and up to 95.6%. Absence of (00l) peaks and concomitant strong intensity of (h00) peaks in the XRD patterns is an indication of either limited tetragonal phase material, or mostly a-domain tetragonal components due to strong tensile stress in the PZT films. In-plane tensile stress is expected to develop in PZT films chemically deposited on platinized Si wafers, on cooling from the crystallization temperature.[27,104]

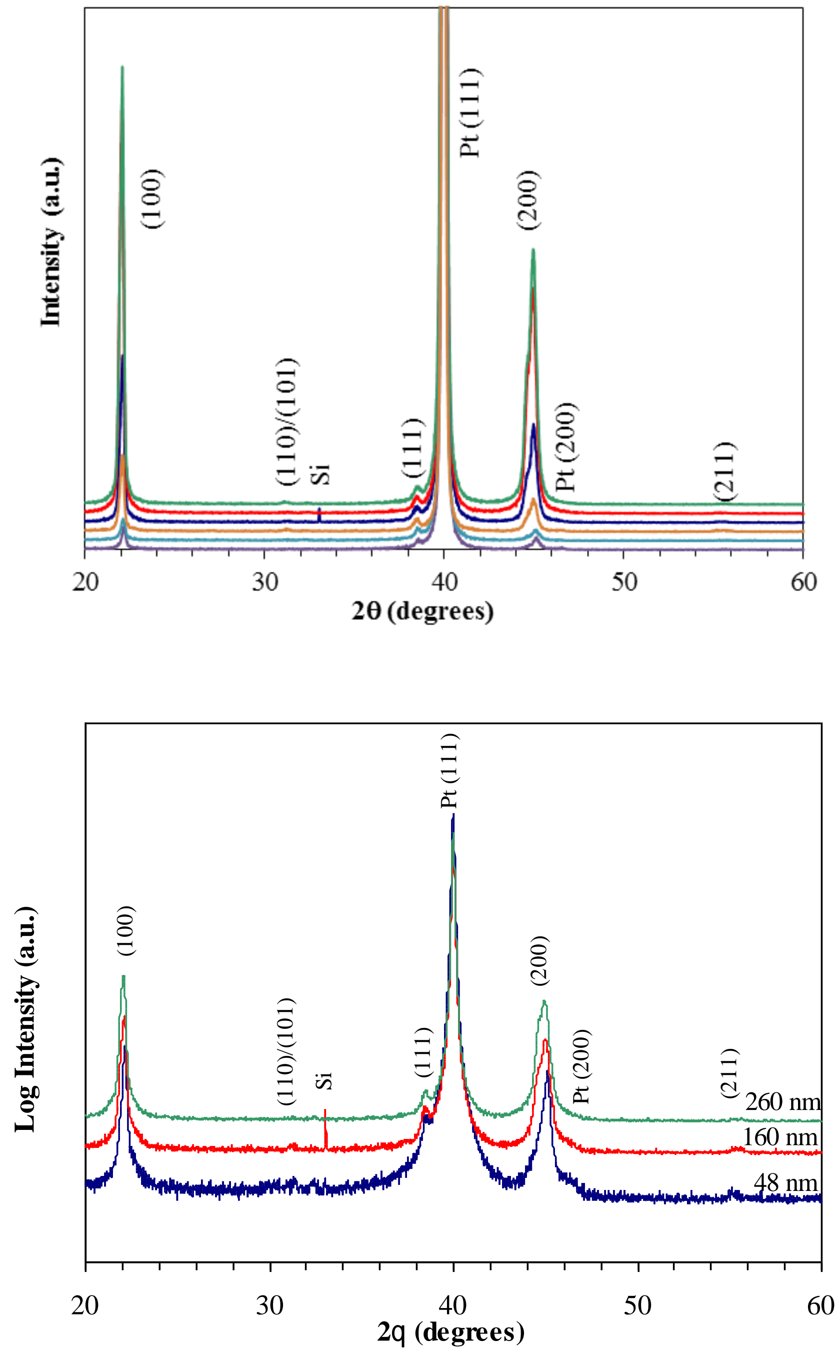

Figure 4.1. XRD patterns of representative PZT films with different thicknesses in linear x-ray count (top) and logarithmic scale (bottom). Pt(111) peak is from the bottom electrode.[26]

SEM studies (Figure 4.2) showed similar morphological features in all films: a bimodal (lateral) grain size distribution, 20 to 50 nm and 100 to 200 nm in diameter

respectively, was observed in the studied range of film thicknesses. Cross sectional SEM images confirmed columnar grain structure in all films (Fig. 4.2d).

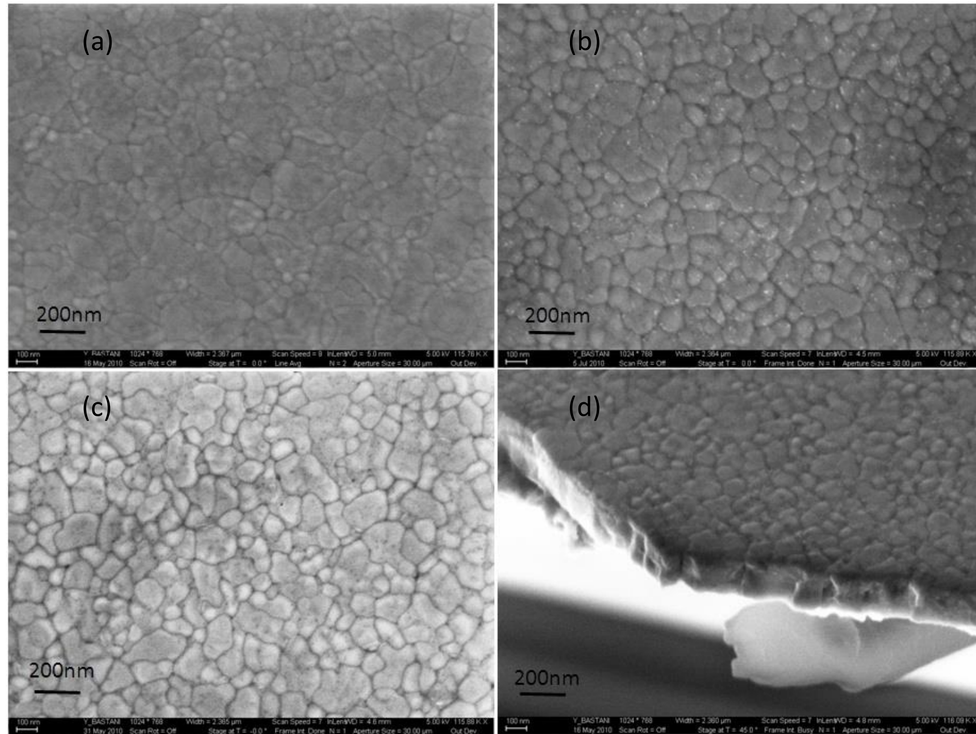

Figure 4.2. Surface topography of (a) 36 nm , (b) 160 nm, and (c) 260 nm thick PZT films. (d) Cross sectional view of a 260 nm thick PZT film, showing columnar grain microstructure.[26]

4.3.2 Dielectric and piezoelectric characterization

Figure 4.3 shows the polarization-electric field (P-E) hysteresis loops of representative samples of the processed films in series A.

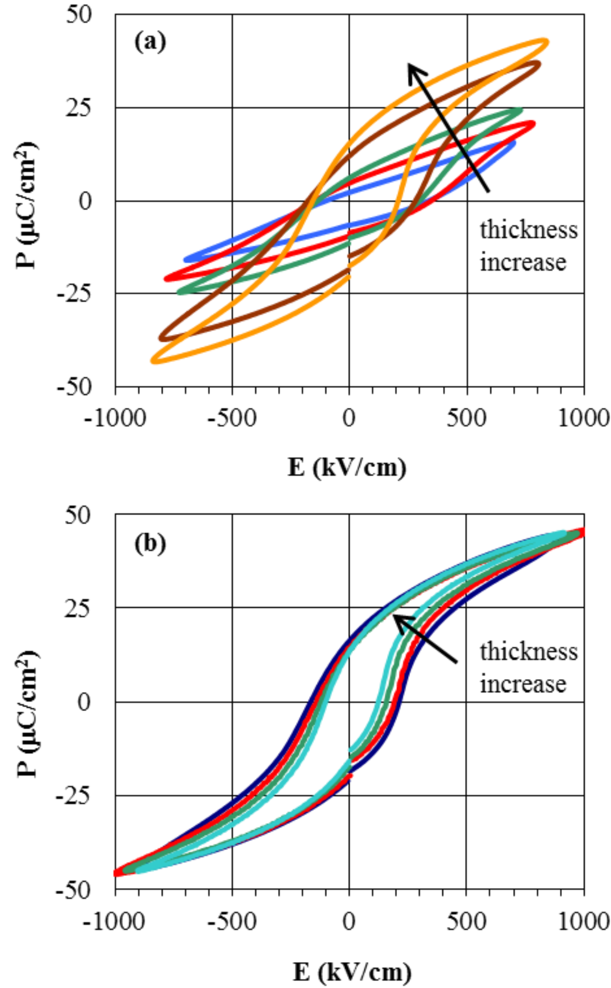

Figure 4.3. Polarization-electric field hysteresis loops for PZT films, with thicknesses of (a) 30, 37, 48, 62 and 107nm and (b) 107, 119, 161 and 207nm; the loops rotate counterclockwise with increasing thickness in (a) and coercive fields decrease with increasing film thickness in (b). Measurements performed at 1 kHz.[26]

A strong counterclockwise rotation of the P-E loops in addition to increased saturation polarization with increasing thickness is observed for films from 37 to 120 nm thick. However, PZT films thinner than ~50 nm did not show complete polarization saturation in their hysteresis loops. Hysteresis loops of films thicker than ~120 nm show a continuous decrease in the coercive field, but no significant other change. Overall, coercive field values ranged from ~250 kV/cm for the thinnest films and decreased with increasing film thickness down to ~90 kV/cm for the thickest films (Figure 4.4). These

values are close but slightly lower than those reported for 100 to 320 nm-thick, sputtered PZT films by Bouregba et al.[105] The difference may be due to the different film texture, PZT composition and processing method used in that work (highly (111)-oriented films with Zr/Ti ratio of 60/40). Considerable increase in coercive field along with clockwise rotation of the P-E hysteresis loop in Bouregba and coworker's work[105] is also noticeable for the 100nm thick film compared to the loops of 200nm or thicker films, indicating a similar trend for PZT films of rhombohedral composition.

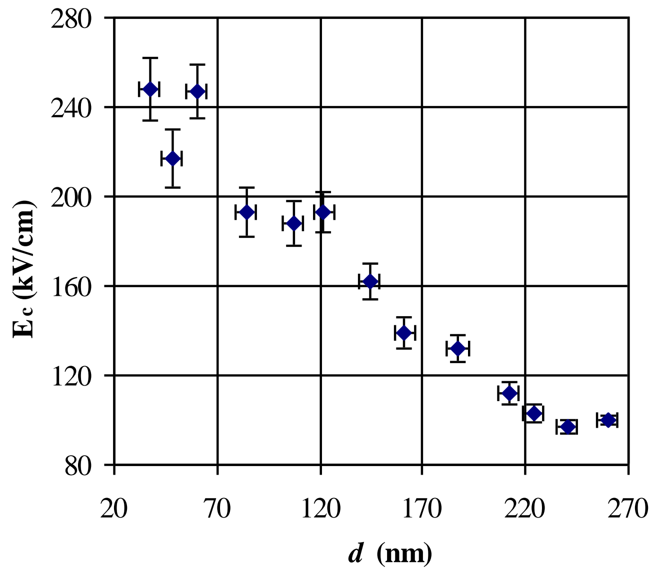

Figure 4.4. Coercive field values of PZT films as a function of thickness.[26]

Rotation of the P-E hysteresis loop as observed above suggests existence of significant biaxial tensile stress, especially in the thinner films, consistent with previous reports.[1,15] Thermal expansion coefficient and crystallographic lattice mismatch between PZT and Si, and PZT and Pt, in addition to the spontaneous strain developed at the ferroelectric transition, are the major sources of biaxial tensile stress development in ferroelectric thin films on platinized Si wafers.[1,104] A biaxial tensile stress is expected to

pull the polarization closer to the substrate plane.[15] This can in turn strongly affect ferroelectric properties, reportedly due to the extreme difficulty of rotation of the ferroelectric polarization (out of plane) and fast back-switching,[106,107] leading to low saturation values and a clockwise rotation of the hysteresis loops. Therefore, the observed counter-clockwise rotation with increasing film thickness indicates decreased average tensile stress in the films. Reduction of tensile residual stress with increasing film thickness for PZT films on platinized Si substrate has been reported previously.[108,109] The significant decrease in coercive field with increasing thickness implies also weaker and/or lower concentration of pinning centers, and in turn higher mobility of the domain walls.[1,71]

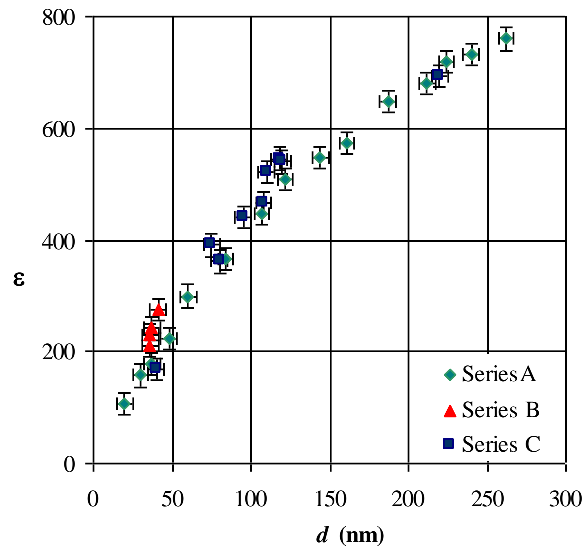

Figure 4.5. Relative permittivity of the films plotted as a function of film thickness at room temperature, measured at 20mVrms and 1kHz.[26]

Thickness dependence of the dielectric permittivity of the PZT films is shown in Figure 4.5. The plotted values are the average for measurement of at least 5 electrodes on each film. Dielectric loss values for all films shown in the graph are below 1.6% and have been omitted for simplicity. Two different regions with approximate linear drops of

permittivity with thickness, with sharper drop for thicknesses below 120 nm, can be observed. Among processing conditions, excess Pb content in the precursor solution has the strongest effect on permittivity values. Ultrathin films processed with higher excess Pb content (series B) show slightly higher dielectric permittivity compared to the other films. However, electrode yield in series B films thicker than 50nm was substantially lower than others. Excess Pb can also react with Pt[52] and create intermetallic phases that can cause reduced electrode yield (down to zero). It is possible that in this work, the two competing processes are both present: 20% excess Pb is leading mostly to reduced yield, but where the intermetallic phase formation is locally suppressed or reduced, improved dielectric response is observed.

All the dielectric permittivity values are substantially lower than what reported for thicker PZT films of similar composition. This is attributed to the presence of an interfacial "dead layer" between the ferroelectric and metallic electrode, similar to what reported for other ferroelectric thin films, such as PZT,[94] $Ba(Zr_{0.25}Ti_{0.75})O_3$ [89] and $(Ba,Sr)TiO_3$.[93,110] This in series capacitor model can be mathematically expressed as:

$$\frac{1}{C} = \frac{1}{C_b} + \frac{1}{C_i} \quad \rightarrow \quad \frac{d}{\varepsilon} = \frac{d-d_i}{\varepsilon_b} + \frac{d_i}{\varepsilon_i} \approx \frac{d}{\varepsilon_b} + \frac{d_i}{\varepsilon_i} \qquad \text{Equation 4.1}$$

Where C, C_i and C_b, are the measured, interfacial layer, and "bulk-like" ferroelectric capacitance, respectively; d and d_i are the total film and interfacial layer's thickness, respectively; ε, ε_i, and ε_b are the as measured permittivity of the whole sample, and the dielectric permittivity of the interface and "bulk-like" ferroelectric, respectively. In the derivation of this relationship, it is assumed that $d_i \ll d_m$ or $\varepsilon_b \gg \varepsilon_i$. Dead layer properties depend on the film-electrode interfaces and although they are

intrinsic, they are also affected by the processing conditions. Therefore, to minimize the processing conditions effects in this analysis, only the data from the films in the series A were used.

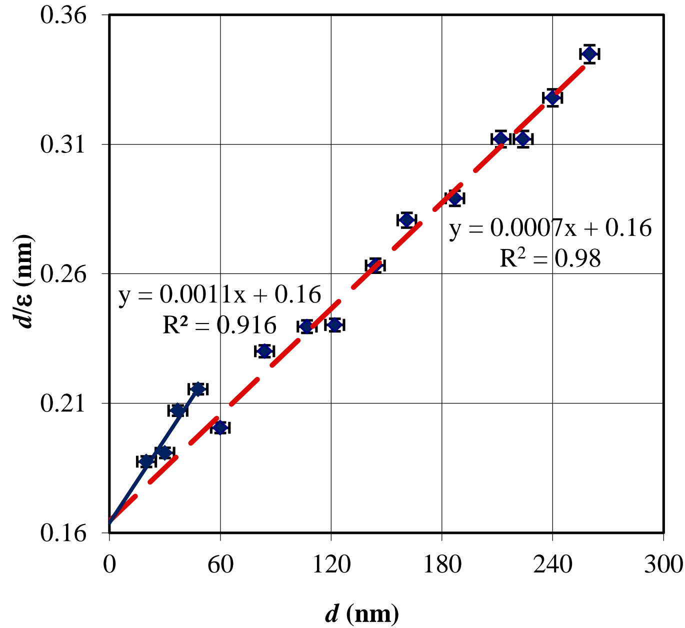

Figure 4.6. d/ε as a function of overall film thickness d for series A films .Dashed trendline is fitted to the data for films of d ≥60 nm, while the solid line is fitted to the thinner than 50nm films. The two trendlines have the same intercept with vertical axis, but different slopes. This suggests the existence of the same dead layer in all films, while the ferroelectric component has degraded dielectric response in the thinner samples.[26]

Figure 4.6 plots the d/ε ratio versus thickness of the films. While data from the films thicker than 50 nm successfully fit to the line associated with the "in-series capacitors" model ($R^2 \approx 0.99$), the thinner films deviate from the trend line, falling above it. This suggests that the measured dielectric permittivity in these films drops faster than in the thicker films. Based on this trend-line, the d_i/ε_i ratio was estimated at 0.16. It is intriguing to note that this is close to the previously reported value of 0.18 for the CSD-derived PZT (Zr/Ti=30/70) films in thickness range of 50 to 500 nm.[94] Thinner films' permittivity can be fit with another line, as also depicted in Figure 4.6. The obtained trend

line has (within experimental error) the same intercept value, but lower slope as shown in Figure 4.6. This suggests the existence of the same parasitic dead layer (same d_i/ε_i ratio) but lower "bulk-like" dielectric permittivity, ε_b with respect to the thicker films. It should be noted from equation 4.1, that change in the ε_b value, will be to some extent overshadowed by the dead layer d_i/ε_i constant term. As it is clear in Figure 4.6, the dead layer d_i/ε_i term contributes a large portion of the film's measured d/ε permittivity: approximately 50% for the thickest films and much more for thinner ones. This underlines the extreme sensitivity of the analysis to the dead layer characteristics and hence film processing conditions, especially for thinnest films.

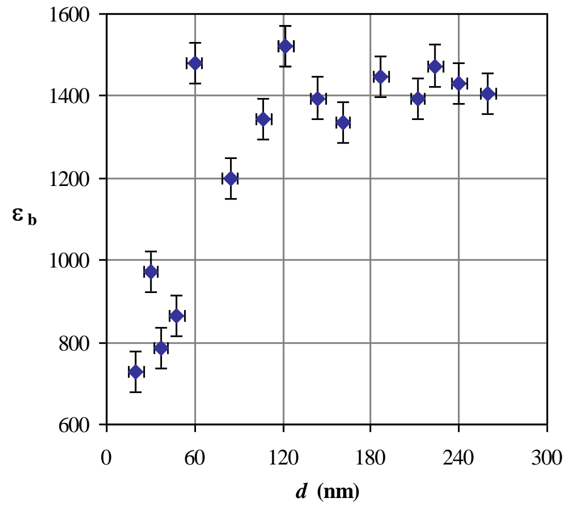

Figure 4.7. Calculated permittivity of "bulk-like" ferroelectric component, ε_b, based on invariant dead layer characteristics (d_i/ε_i =0.16).[26]

Figure 4.7 shows calculated "bulk-like" dielectric permittivity, ε_b, based on the d_i/ε_i ratio obtained from the trend-line in Figure 4.6. It is clear that the permittivity of the bulk-like portion of the film, ε_b, drops from the average value of 1400±100 for the thicker films, down to ~750 to 900 for films thinner than 50 nm. Such behavior indicates that below a critical thickness of ~50 nm, sources of size-effects are not limited to the

intrinsic dead layer, but include also components affecting the "core" ferroelectric material.

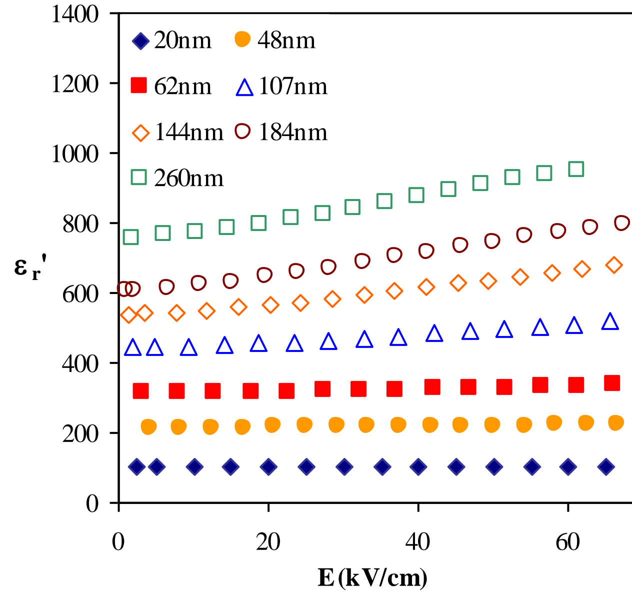

Figure 4.8. Field dependence of the real component of the dielectric permittivity for the PZT films of different thicknesses.[26]

To investigate the intrinsic or extrinsic origin of the permittivity suppression in the "core ferroelectric" component of ultrathin films, dielectric nonlinear measurements were performed. The ac electric field dependence of the real part of the dielectric permittivity, ε', measured at 1kHz, is shown in Figure 4.8. Rayleigh Law (as explained in chapter 1) was used to analyze the linear region in each curve.

Figure 4.9 shows the Rayleigh parameters: α', ε'_{init}, and $\alpha'/\varepsilon'_{init}$ for the PZT films of different thicknesses. The graphs also show the Rayleigh coefficients and their ratios reported by Bassiri-Gharb et al.[9] and Bintachitt et al.[111] for PZT (Zr/Ti=52/48) films with thicknesses ranging from 270 nm to 6 μm. The values for the 260 nm thickness film from series A ultrathin films seem to be very close and somewhat larger than the values for the

same thickness film reported by Bassiri-Gharb et al.[9]. Higher quality or higher (100) texture of our films might lead to higher nonlinear dielectric response parameters. While ε'_{init} seems to reach a plateau for higher film thicknesses, α' and $\alpha'/\varepsilon'_{init}$ continuously increase with the film thickness from 50 nm up to 6 μm. Furthermore, for films below 50 nm thickness, α' and $\alpha'/\varepsilon'_{init}$ are close to null, indicating that the irreversible extrinsic contributions are mostly suppressed. This suggests that the source of the critical thickness in the PZT ultrathin films is extrinsic.

In addition to grain size, residual stress resulting from strong clamping to the substrate and specifically its gradient across the film thickness can lead to reduced extrinsic contributions to the dielectric response. This will be discussed in detail in chapter 7. In fact, as highlighted earlier, strong suppression of polarization saturation was observed in the same thickness range. Local stress in thin films can act as pinning site for domain walls, as well as affect the equilibrium domain structure.[9,71] Additionally, stress gradient across film thickness has shown to have significant adverse effect on the dielectric response of ferroelectric thin films[112]. The residual stress in epitaxial PZT [113]/37 and barium strontium titanate [112] films has an exponential distribution through the film thickness, decaying from the film-substrate interface towards the film bulk. This implies a higher stress gradient average in the ultrathin films, and in turn more deteriorating effects on these films' dielectric response.

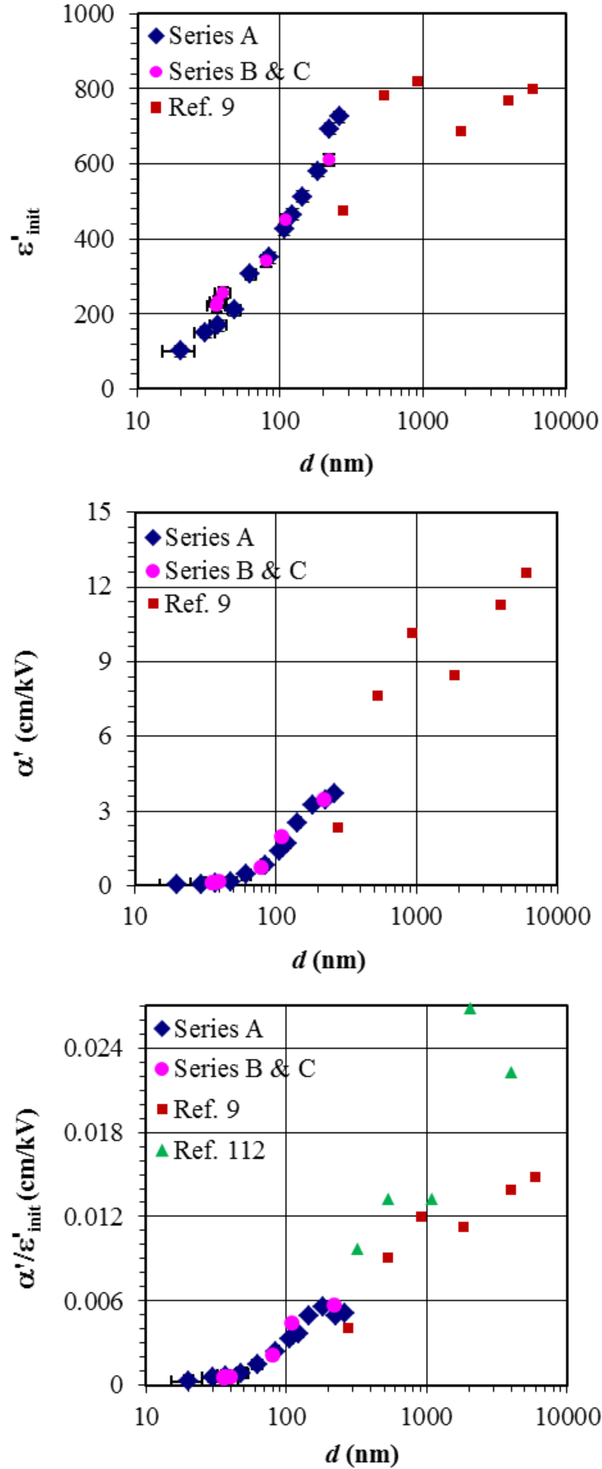

Figure 4.9. (Top) Reversible, ε'$_{init}$ and (Middle) irreversible, α' Rayeligh parameters, and (Down) α' /ε'$_{init}$ ratio as a fuction of film thickness. Data for thicker films (0.27 to 6 μm) are shown from Bassiri-Gharb et. al[9] and Bintachitt et al.[111] for comparison.[26]

The critical size reported here is within the range reported for epitaxial PZT films (Zr/Ti=20/80), where formation of ferroelastic domain walls are no longer energetically favorable. Based on theoretical and experimental observations, the critical grain size for PZT20/80 is expected to be in the range of 20 to 100 nm.[71,98,99,114] Disappearance or reduced population of domain walls also leads to significant increase in the coercive field,[71] which indeed was observed in our films at decreased thicknesses. However, further investigation such as higher harmonic piezoelectric nonlinear studies, is needed to verify this hypothesis as is further discussed in Chapter 8.

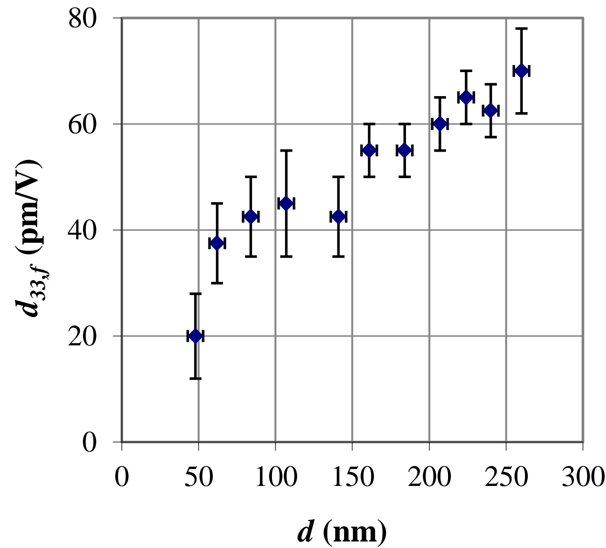

Figure 4.10. Effective longitudinal piezoelectric coefficient measured at 1kHz under dc electric bias fields of $2E_c$.[26]

Figure 4.10 shows the effective piezoelectric coefficient $d_{33,f}$ measured for different film thicknesses. No reliable measurement was possible for films of thickness ≤37 nm. The piezoelectric response of the films increased continuously with film thickness from ~20 pm/V to ~70 pm/V. However, a significant jump (~50%) in $d_{33,f}$ values is observed for 48 nm thick film with respect to 60nm and thicker films. This is consistent with the critical thickness observed in the dielectric responses of these films.

All the dielectric and piezoelectric measurements here reported indicate a change in the behavior of the ferroelectric component of the PZT films at a thickness close to 50 nm. From the Rayleigh measurements, it is clear that the origin of such variation has to be sought in the extrinsic response and more specifically in the domain wall population and/or mobility. As mentioned earlier, critical thickness for disappearance of ferroelastic domain walls has been previously reported; a grain size of ~21 nm was suggested by Madsen et al.[98] The authors did however suggest that this is an underestimated value and that in actual ceramics, where presence of multiple grains can lead to creation to additional stress, the actual critical grain size might be larger. In addition to the grain-to-grain constraints, it is also expected that the residual stresses in our films would contribute to the total energy of the system. Hence, a critical size of ~50 nm is quite in line with the previous theoretical work. It is also worth underlining that the transition at 50 nm thickness is mostly a continuous transition rather than an abrupt variation in most of our measurements. However, the change seems to be highlighted in the dead-layer model.

On a last note, piezoelectric nonlinear response of the films could potentially allow to confirm the source of the observed critical size. In fact, although both ferroelastic and ferroelectric domain wall motion can contribute to the piezoelectric nonlinearity of ferroelectric thin films, the higher order harmonic response of the films is different in each case.[11,115] Unfortunately, our attempts to study the ac electric field dependence of the d_{33} piezoelectric coefficient of the films were unsuccessful, mostly due to the quick aging after removal of the poling electric field (instability of the

polarization). Such quick aging is also consistent with the overall dielectric and piezoelectric response of these ultrathin films.

4.4 Summary and Conclusions

A CSD-derived, (100)-oriented thin PZT layer was successfully used as "homogeneous seed layer" to reliably create highly (100)-textured PZT ultrathin films with thickness ranging from 20 to 260 nm with consistent microstructural characteristics. Thickness dependence of the dielectric and piezoelectric response of the PZT films in this thickness range was studied.

Relative permittivity, saturated and remanent polarization and piezoelectric response drop as the film thickness decreases and shows a drastic drop at ~50 nm film thickness; critical thickness. The critical thickness (~50 nm) was observed in P-E hysteresis and nonlinear dielectric measurements due to the cut-off of the extrinsic contributions to the dielectric response of the films. The presence of this critical thickness leads to the deviation of the thickness dependence of the dielectric permittivity from the "in-series capacitors"/"dead layer" model. The critical size observed here is consistent with the thickness range reported for epitaxial PZT films, where ferroelastic domain walls are no longer present, due to energy reduction arguments.

Although piezoelectric measurements couldn't be completed for all of the films, a similar deviation from the trend was also observed at the same critical thickness in $d_{33,f}$ values. Presence of such a critical thickness is especially relevant considering the continuous drive towards miniaturization in the technological applications of ferroelectric thin films. In addition to the physical size, other factors such as global and local chemical

homogeneities and substrate-induced strain fields can also profoundly affect the functional properties of ferroelectric materials. These effects and the role of extrinsic contributions in them will be discussed in the coming chapters.

Chapter 5

Effects of Chemical Heterogeneity on the Dielectric and Piezoelectric Response of Highly (100)-Textured PZT Thin Films; Superlattice-like Structure

This chapter investigates the effects of chemical heterogeneity and in particular cation gradients on the dielectric and piezoelectric response of PZT ultrathin films. Spontaneous Zr/Ti gradient formation during crystallization in CSD processed PZT films was used to prepare superlattice-like (SL), highly (100)-oriented thin films on Pt/Ti/SiO_2/Si substrates. SLs with stacking periodicity ranging from 13 up to 60 nm were synthesized with compositional gradient normal to the film surface and composition centered at $x \approx 0.53$. XRD structural refinement, along with XPS depth profile chemical analysis, revealed that the crystal structure alternates between rhombohedral and in-plane polarized tetragonal phases, effectively corresponding to “artificially-created” phase boundaries. SL films have ~45% and ~20% higher $d_{33,f}$ piezoelectric coefficient and dielectric permittivity, respectively, with respect to compositional-gradient-free films of similar thickness, possibly due to enhanced reorientation of electrical dipoles and higher extrinsic contributions due to the motion of the “artificially-created” phase boundaries in SL films. This processing method provides a simple chemical route to create ultra-thin ferroelectric films with enhanced dielectric and piezoelectric properties suitable for a range of miniaturized applications.

5.1 Introduction [2]

As discussed in the previous chapter, extrinsic and intrinsic size effects (at specific ferroelectric/electrode material combinations) in ferroelectric thin films limit their dielectric and piezoelectric response at sub-micron sizes. However, with current advancements in MEMS technology, it is essential to process ultrathin ferroelectric films with maximized piezoelectric response for integration into high performance MEMS and NEMS devices. Chemical heterogeneity is among various factors affecting the piezoelectric response of the ferroelectric films. Chemical heterogeneities have been generally considered detrimental to the properties of PZT films, especially in the 1 micron or higher film thickness range.[68] This chapter discusses how to exploit spontaneous formation of chemical heterogeneities towards increasing the dielectric and piezoelectric response of ultrathin (~200nm thickness) PZT films via superlattice-like structures.

Superlattice (SL) or heterolayered ferroelectric thin films consist of alternate layers of ferroelectric materials, or phases, with a compositional gradient normal to the substrate. These type of structures have different and sometimes unusual physical properties than their homogeneous thin film counterparts.[116] For example, pulsed laser deposited $PbZrO_3/PbTiO_3$ epitaxial superlattices are reported to have enhanced dielectric permittivity with respect to $Pb(Zr_xTi_{1-x})O_3$ (PZT) solid solution thin films prepared under similar deposition conditions.[117] Similarly, dielectric permittivity and remnant polarization were enhanced in superlattice PZT40/PZT60 thin films compared to solid

---

[2] The content of this chapter is mainly based on work published in Acta Materialia.

solution PZT films.[118] Dielectric and piezoelectric properties can be tailored in ferroelectric SLs by having a dense and columnar crystal structure with coherent strain between heterolayers. This can be achieved by designing the single layers' thickness and material.[119] Ferroelectric superlattices offer opportunities for high-density, nonvolatile memories, [118] terahertz emitters and electro-optic applications, [120,121] and enhancement of the effective piezoelectric response for energy harvesting at nanometer scale.[122] Furthermore, they are of fundamental scientific importance in understanding ferroelectric phase transition and polarization switching behavior.[119,123]

PZT has strong dielectric and piezoelectric response, especially at the morphotropic phase boundary composition (MPB, $x \approx 0.53$). The alternating rhombohedral/tetragonal (centered around MPB) compositional configuration of PZT SLs has been theoretically shown to lead to enhanced electromechanical response, [124] and unusual thermodynamic properties and nonergodicity.[116] However, processing of the pure perovskite-phase, Pb-based ferroelectric oxide SLs has proved challenging, because lead is volatile at the high crystallization temperatures required. Additionally, cation diffusion at elevated processing temperatures can hinder required compositional gradient in artificial PZT heterolayers, resulting in poor crystal structure periodicity and compositional control.[125,126] To date, the most successful PZT SLs (with high order satellite peaks in X-ray diffraction patterns, as structural characteristics of a good superlattice) have been processed using constituent materials at two compositional extremes ($PbZrO_3$ and $PbTiO_3$), to partly compensate for cation interdiffusion at elevated processing temperatures.[126] The SLs have also been typically epitaxially-grown on single crystal substrates,[117,125-127] which limits their industrial applications. Conversely, in non-

epitaxial, sol-gel derived PZT heterolayers, superlattice characteristics have been mostly absent or very weak, as revealed from reported crystal structure characterizations.[118,128] We report chemical solution deposition of PZT SLs, with composition centered around MPB (x ≈ 0.53), on $Pt/Ti/SiO_2/Si$ substrates. The proposed processing method takes advantage of the kinetic drive for spontaneous B-site cation (Zr/Ti) gradient formation during crystallization of each deposited layer, [63,68] to process superlattice-like structures. Creation of a Zr/Ti gradient is favored in most $PbTiO_3$-solid solutions, due to the lower nucleation energy of the Ti-rich compositions: nucleation and growth of a $PbTiO_3$-rich phase is initiated at lower temperatures, leading to an enrichment of the non-crystallized material in Zr, i.e. a $PbZrO_3$-rich remnant phase.[63,68,129] As a result, in multilayer PZT films, each crystallized PZT layer is Ti-rich at the interface with the previous layer and Zr-rich at the surface. This kinetically-driven method ensures good compositional control, as well as crystalline and microstructural quality of the films processed at high temperatures. Furthermore, the cation diffusion is mostly limited to within layer variations, resulting in phase pure, dense PZT SL films, deposited on polycrystalline substrates.

5.2. Experimental Procedures

Precursor solutions were prepared as explained in chapter 2, with nominal compositions of $Pb_{1.2}Zr_{0.53}Ti_{0.47}O_3$ (PZT53), $Pb_{1.2}Zr_{0.43}Ti_{0.57}O_3$ (PZT43) and $Pb_{1.2}Zr_{0.63}Ti_{0.37}O_3$ (PZT63). Films were prepared using precursor solutions with 0.1M, 0.2M and 0.4M concentrations. The SLs were prepared using the PZT53 precursor solution. Reference PZT films were also prepared with a 2-annealing-step process: a first annealing was performed after the first layer of PZT precursor solution was deposited and

pyrolysed. This first layer acted as a seed layer for the (100)-orientation of the overall film as explained in chapter 3. Next, multiple layers were spin-coated onto the substrate and pyrolysed before the second and final crystallization was performed for all layers. Films processed with this method, which is similar to the traditional processing route used for sol-gel derived ferroelectric films,[26,28,68,130] are referred to as multi-layer annealed (MLA) films.

Additionally, PZT43 and PZT63 precursor solutions were used to create reference gradient-enhanced (GE) and gradient-free (GF) films. In order to enhance the Zr/Ti compositional gradient in the superlattice films, precursor solutions of PZT43 (first) and PZT63 (second) were spin coated onto the substrate and pyrolyzed separately. Each bilayer of PZT43/PZT63 was then crystallized in a single step. Similarly, to reduce the B-site cations' gradient and obtain "ideally" gradient-free films, three layers of PZT63, PZT53 and PZT43 were deposited and pyrolysed respectively and then crystallized together, following a route described by Calame at al.[68] Different processing configurations used for synthesis of PZT films in this work are schematically shown in Figure 5.1.

The Si (400) peak was used for peak position calibration in XRD structural analysis. Depth profile X-ray photoelectron spectroscopy (XPS) (K-Alpha, Thermo scientific) measurements using Ar+ ion sputtering (sputtering rate of ~3 nm/min) was performed on the samples for depth-profile chemical analysis.

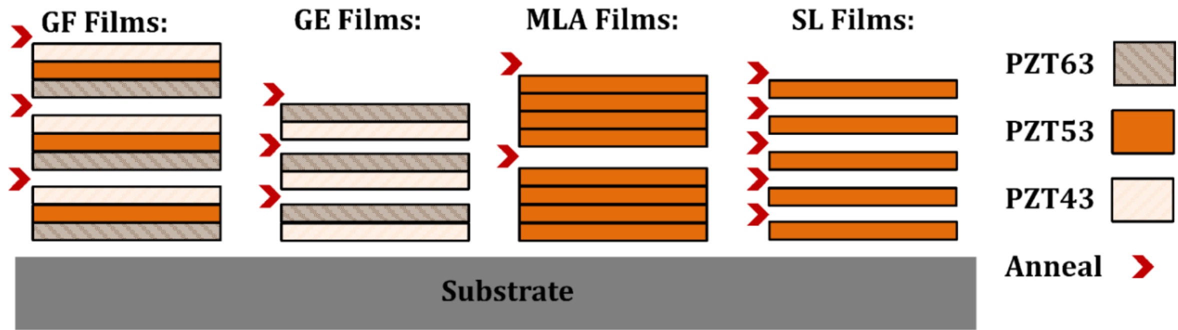

Figure 5.1. Schematic representation of the layers configuration for different PZT films used in this work with respect to the number and order of annealing steps through the film thickness and composition of the solution used for each layer.[36]

5.3 Structural and Chemical Microanalysis

Due to the Zr/Ti gradient formation, the thickness of each crystallized layer in SL films should determine and be equal to the periodicity of the superlattice, Λ. In general, the single layer thickness is determined by the precursor solution's concentration and the spin coating speed. PZT films with superlattice periodicities ranging from 13 to 60 nm were prepared mainly through modification of the precursor solution's concentration, as shown in Table 5.1.

Table 5.1. Stacking periodicity as a function of solution concentration for SL films spun coated at 3000 rpm.[36]

Solution Concentration	Λ, XRD analysis (nm)	Crystallized layers	Total film thickness, (nm)	Λ', Single layer thickness (nm)
0.4M	59.8± 0.5	11	665±15	60±1.5
0.2M	31.7± 0.5	6	190±10	32±1.5
0.1M	13± 0.5	11	140±10	13±1

The XRD patterns of representative superlattice-like, "gradient-free" (GF) and "gradient-enhanced" (GE) films are shown in Figure 5.2. All films show perovskite

structure with strong (100) preferential texturing. The lattice parameter for a pseudo-cubic unit cell, calculated based on the position of the main (100) Bragg reflection peak for SL films, a = 4.048±0.05 Å, is very close to the value reported for $Pb(Zr_{0.53}Ti_{0.47})O_3$ powder [131].

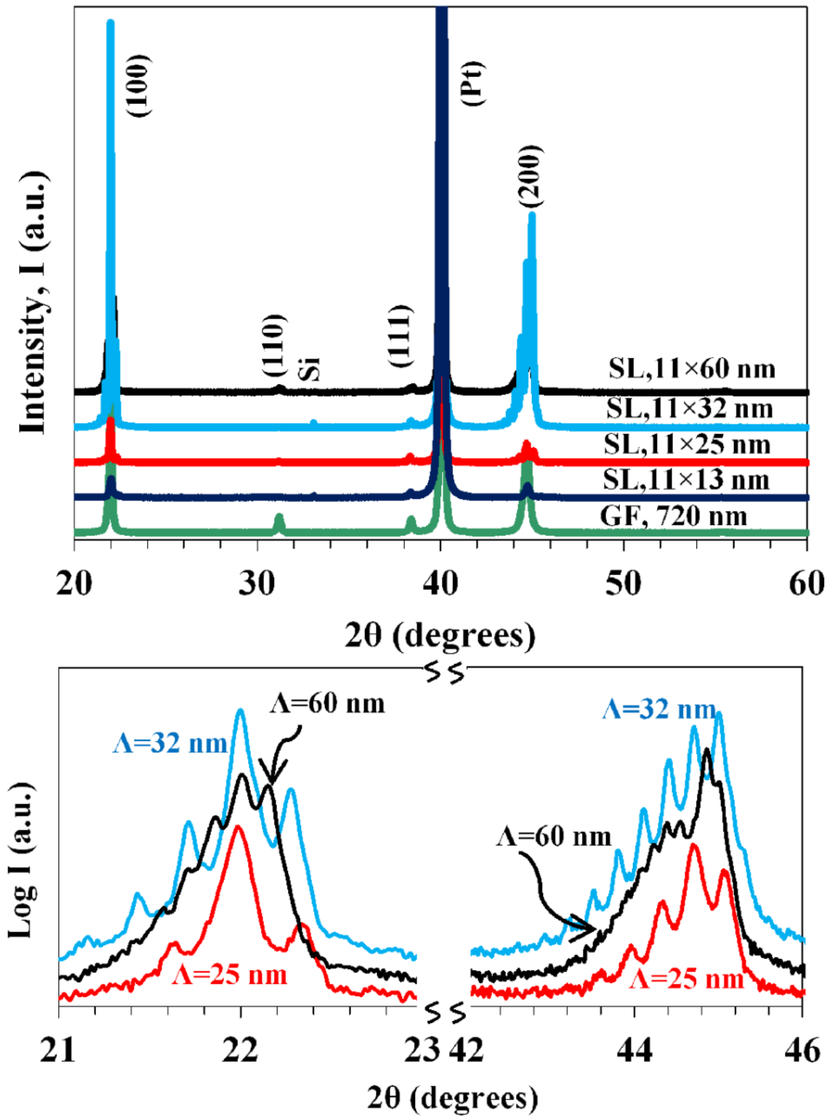

Figure 5.2. XRD patterns of superlattice-like (SL) and gradient enhanced superlattice (GE) PZT films with different numbers of crystallization steps and stacking periodicity reported for each pattern, along with the XRD pattern of an ideally gradient free (GF) PZT film with 5 crystallization steps, showing no satellite peaks (Top). Detailed views of

the SL satellite peaks around {100} and {200} Bragg reflection peaks as a function of stacking periodicity (Bottom).[36]

Satellite peaks, located around the main Bragg reflections, especially at {100} and {200}, are observed as characteristic for superlattice structures [132]. Stacking periodicity of the SL films was calculated from the position of the satellite peaks in the XRD pattern, based on the Schuller formula:[125,132]

$$\frac{2\sin\theta}{\lambda_x} = \frac{1}{\bar{d}} \pm \frac{n}{\Lambda} \qquad \text{Equation 5.1}$$

In this expression, θ is the x-ray diffraction angle, λ_x is the x-ray wavelength, $\bar{d}$ is the average atomic interplanar distance and n is the satellite peak order integer. The calculated periodicity of the superlattice films, Λ, was in excellent agreement with the calculated thickness of a single deposited layer, Λ', based on profilometer thickness measurements (Λ' ≅ d/n, where d and n are the measured film thickness and number of deposited layers respectively), as shown in Table 1. The observed evolution of the XRD patterns of the SLs with respect to the stacking periodicity (Figure 5.2) is also very similar to previously studied superlattice structures: at decreasing stacking thicknesses the XRD pattern evolves from two separate peaks associated to extreme constituents, respectively, to a series of satellite peaks around the two approaching peaks and later around a single peak, and finally a single peak corresponding to the average composition [126,132]. The presence of high order satellite peaks in the XRD patterns indicates a high quality superlattice structure formed by coherent (epitaxial-like), layer by layer growth of constituent materials in a dense assembly of grains. This is further supported by the plain and cross-sectional (field-emission) SEM views of the SL films (Figure 5.3): all films show a columnar grain growth with minimal defects. Furthermore, all films showed a

similar grain size distribution, with an average grain size of ~110 nm. No secondary phases were observed within XRD detection limits in the PZT films with SL periodicities as small as 13 nm (corresponding to about 32 unit cells).

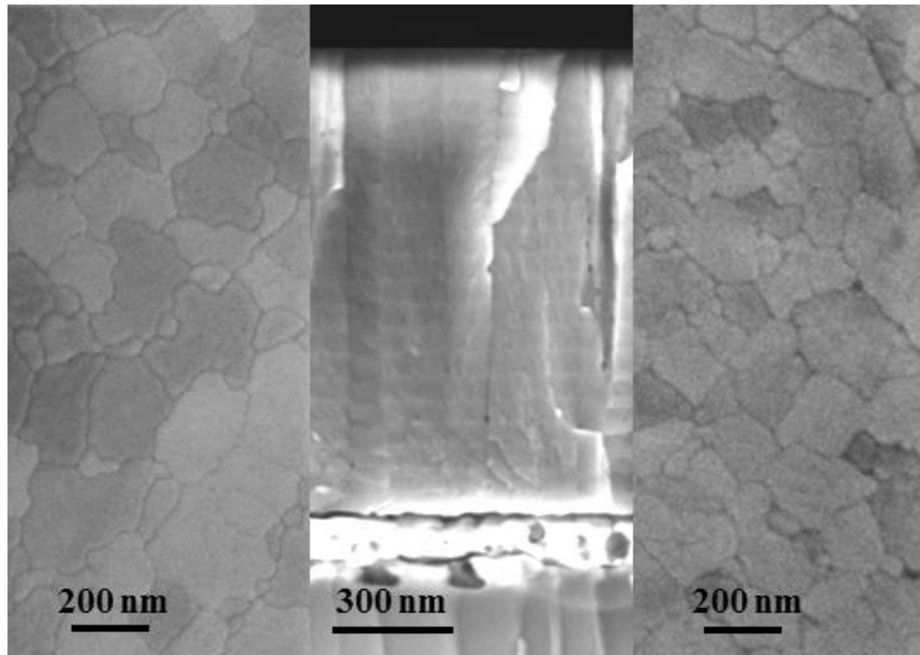

Figure 5.3. Field-emission, scanning electron micrographs of cross section and surface of a 1.2μm thick superlattice PZT film with Λ =60 nm (left and center), showing dense, layer by layer growth of columnar grains in the microatructure. Surface topography of a 190 nm thick (Λ =32 nm) superlattice PZT film (right).[36]

Figure 5.4a shows the atomic percentage variation through the thickness for all the constituent elements, as obtained by XPS depth profiling, in a PZT53 SL with stacking periodicity Λ =32 nm (6 annealed layers, 190 nm total thickness). Figure 5.4b shows a comparison between Zr and Ti content variations through the thickness for SL, GE, MLA and GF films. The atomic percentages were calculated based on the Scofield atomic sensitivity factors incorporated into the tool analysis software. Measured atomic percentages for all films are compared with nominal values based on $Pb(Zr_{0.53}Ti_{0.47})O_3$ composition in Table 5.2.

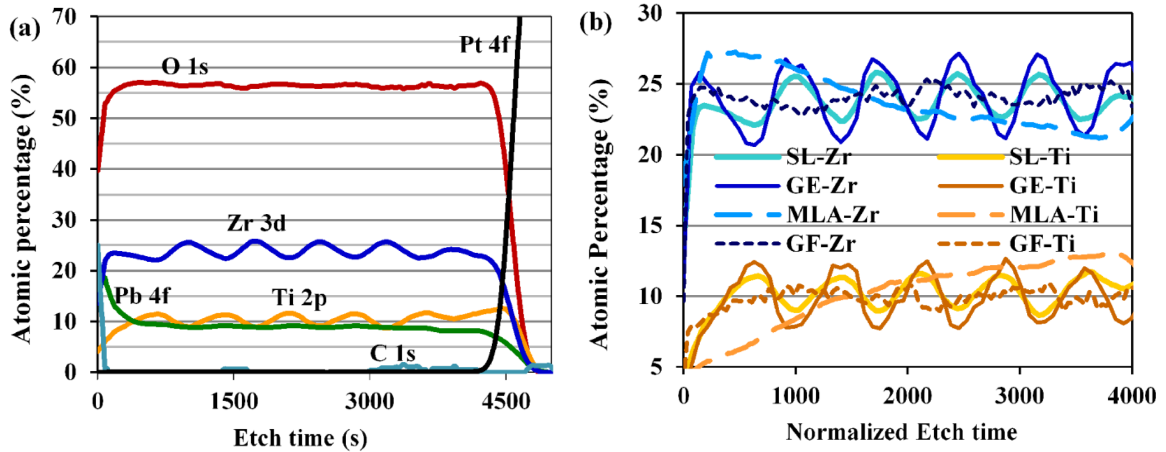

Figure 5.4. Atomic percentages, as measured by XPS depth profiling of the constituent elements in (a) PZT SL with stacking periodicity, Λ =32 nm (6 annealed layers, 190 nm total thickness), and (b) Zr and Ti atomic percentage variations in SL, gradient enhanced (GE), multiple layer annealed (MLA), and gradient free (GF) PZT films, as a function of normalized etch time.[36]

An overestimation of Zr and an underestimation of Pb content were observed in the quantitative XPS analysis results (Table 5.2). This could arise for example from the effect of Zr on the Pb ionization cross section, as previously reported by Habouti et al. [133] and references therein. Pb and O contents were almost constant through the film thickness for all samples. On the other hand, Zr and Ti atomic concentrations fluctuated as a function of the film deposition history: a Ti-rich composition was observed at the (bottom) interface with previous layers and a Zr-rich composition was observed at the surface (top) of each crystallized layer. This trend was observable in SL, GE, and MLA films, and has also been previously observed via energy dispersive x-ray analysis with transmission electron microscopy (EDX-TEM) for MLA-like PZT films.[68] The Zr content variation (25±3%) calculated in our XPS depth profiling for the 200 nm MLA PZT film is close to that reported (24±4%) by Calame et al.[68] for ~250 nm-thick PZT53 films measured via EDX-TEM.

Table 5.2. Atomic percentages of the constituent elements in the ~190nm-thick PZT films obtained from XPS quantitative depth profile analysis compared to nominal stoichiometric composition. All values are in (%), and XPS measured values are subject to ±2% instrumentation error.[36]

XPS spectra	SL	GE	MLA	GF	Nominal
Pb($4f_{7/2}$)	9	8.5	9	8.5	20
Zr($3d_{5/2}$)	22 to 26	20.7 to 27.2	21 to 27	23 to 25.2	10.6
Ti($2p_{3/2}$)	8.5 to 11.5	7.5 to 12.5	7 to13	8 to 12.2	9.4
O(1s)	56	56.5	56	56.5	60
Zr-var.(%)	16.6	27.1	25	9.1	-

The amplitude of the B-site cation variation increased with the thickness of the crystallized layer: therefore, Zr/Ti concentration gradients were better comparable between SL and GE films and, similarly, between GF and MLA films (Table 5.2). Zr content variation in "gradient-enhanced" films was increased by more than 60% compared to SL films. Conversely, "gradient-free" films had approximately 55% lower Zr content variation compared to MLA films. This underlines the versatility of chemical solution processing for tailoring the compositional variations in PZT films, or any other solid solution where one component is thermodynamically more stable.

The ~16% atomic percentage variation in Zr content within each layer of the SL PZT film with $\Lambda \cong 32$ nm (Table 5.2) corresponds to a compositional variation ranging from a Zr/Ti ratio of about 45/55 (tetragonal, lattice parameters: $a_0 = 0.402$ nm and $c_0 = 0.412$ nm) [134] to 61/39 (rhombohedral, close to 60/40, $a_R = 0.4070$ nm) [135] centered around the precursor solution's nominal composition of PZT53 (see Fig 5.5). It is

intriguing to note that the calculated lattice parameter (a = 0.405±0.05 nm) based on the main Bragg peak in the XRD pattern of the SL film lies between a_0 and a_R, and far from c_0. This indicates that the crystal structure in the superlattice changes alternatively from in-plane tetragonal (a-axis, in Ti-rich component) to rhombohedral (Zr-rich component) in each deposited layer. The in-plane polarization of the tetragonal phase has been reported previously for sol-gel PZT films on Si substrates and is mostly attributed to the residual tensile stress in the films caused by the large thermal expansion coefficient mismatch (and ferroelectric distortion) between PZT and Si [28,136].

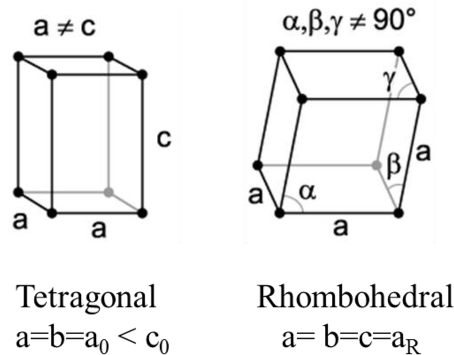

Figure 5.5 schematic representation of tetragonal and rhombohedral crystal lattice.

5.4 Dielectric and Piezoelectric Characterization

Table 5.3 shows the low-field dielectric response of the 190nm-thick PZT SL (Λ =32 nm) compared with that of MLA, GF and GE PZT films of similar thickness, as well as their nonlinear dielectric and piezoelectric Rayleigh parameters, and their piezoelectric, $d_{33,f}$ coefficients measured under a dc bias field close to the coercive value. The nonlinear piezoelectric measurements were carried out under the DC bias equivalent to $2E_c$ of the films. The low-field dielectric loss was below 1.7% for all films. The

dielectric permittivity of the gradient-enhanced films was inferior to the response of all other films. PZT SL films showed ~20% increase in the low-field dielectric permittivity compared to GF films and ~30% increase with respect to GE films. The dielectric response of our 190 nm-thick SL film is also higher than the value previously reported for 200 nm- and 480 nm-thick PZT superlattice films.[125,137] This could be also partially due to the different PZT compositions [125] or higher crystalline quality of the films in this work.

Table 5.3. Low field dielectric permittivity (at 1 kHz, 20 mV_{rms}), reversible and irreversible dielectric and piezoelectric Rayleigh parameters and their ratio for ~200 nm-thick superlattice (SL), gradient free (GF), and gradient enhanced (GE) PZT films. Low-field dielectric loss values are below 1.7% for all films and nolnilear dielectric and piezoelectric measurements were conducted at 1kHz.[36]

Sample	SL	GE	GF	MLA
ε_r	724 ± 22	560 ± 17	602 ± 13	590 ± 18
ε'_{init}	670	540	550	555
α' (cm kV^{-1})	2.2 ± 0.05	1.95 ± 0.03	1.35 ± 0.03	1.36 ± 0.03
$\alpha'/\varepsilon'_{init}$ (10^{-3} cm kV^{-1})	3.3 ± 0.1	3.6 ± 0.1	2.45 ± 0.1	2.45 ± 0.1
$d_{33,f}$ (pm/V)	95 ± 5	45 ± 5	65 ± 5	65 ± 5
d_{init} (pm/V)	77.6 ± 3.1	43.7 ± 3.3	57.7 ± 4.1	56 ± 3.9
α_d (10^{-19} m^2/V^2)	7.4 ± 0.5	4.8 ± 0.6	4.6 ± 0.6	4.5 ± 0.5
α_d / d_{init} (10^{-9} m/V)	9.5 ± 1.3	10.7 ± 1.5	7.9 ± 1	8 ± 0.9

The enhancement in the relative dielectric permittivity of the SL films is likely due to the interaction of electrical dipoles at the layer-to-layer interface between the rhombohedral phase and the tetragonal phase. This is effectively equivalent to “artificial creation” of phase boundaries throughout the film, which can lead to enhanced

reorientation of electric dipoles, [118,126,137] in a process similar to the dielectric enhancement at the MPB for many ferroelectric and relaxor-ferroelectric solid solutions.[22] Kornev, and Noheda et al. have also suggested possible formation of intermediate phases (such as monoclinic and triclinic) at the same interfaces,[116,138] leading to an enhancement of the dielectric response through the polarization rotation mechanism.[139] However, any peaks associated with such intermediate phases would overlap with the satellite pattern observed in XRD and were indistinguishable in our work.

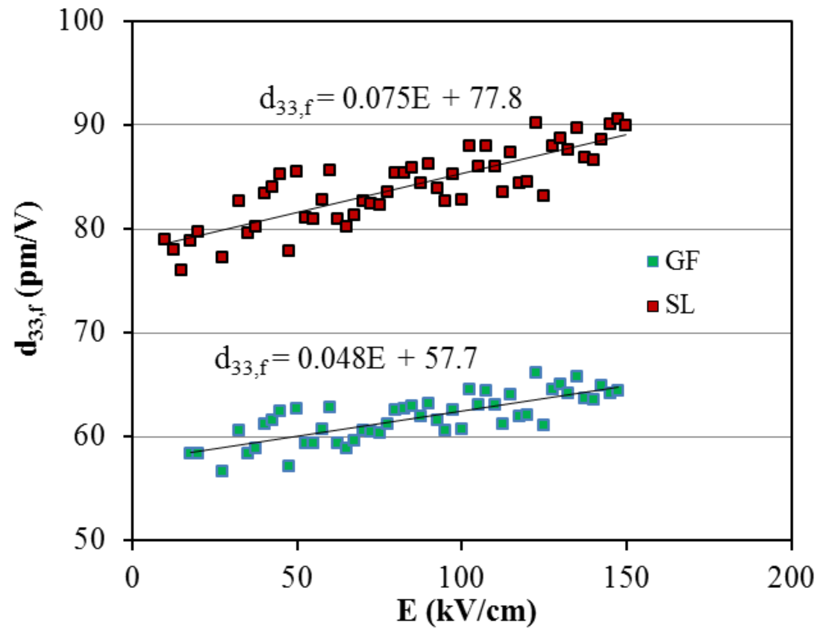

Figure 5.6. Ac electric field dependence of the piezoelectric coefficient for ~200 nm-thick SL and GF films. Capacitors were under constant $2E_c$ bias field during the measurements.

The extent of the enhancement of the dielectric response is also dependent upon the extent of the overall compositional gradient: compositional variations far away from the MPB might hinder constructive electrical dipole interactions, as in the case of the GE

films. Conversely, the GF and MLA films had no periodic tetragonal/rhombohedral interface, i.e. "artificially-created" phase boundaries, to offer an additional contribution to the dielectric response; however, the overall composition was maintained closer to the MPB for GF films, and therefore the dielectric permittivity was slightly higher in GF films than in MLA films.

To investigate the effect of the "artificially-created" phase boundaries in SL films on their dielectric and piezoelectric response, nonlinear studies in the framework of Rayleigh analysis were conducted as explained in chapter 1. The linear increase in the $d_{33,f}$ and dielectric permittivity, as a function of the applied AC field's amplitude, was analyzed in terms of the intercept, $\varepsilon'_{\mathrm{init}}$, d_{init}, and slope of the curve, α' and α_d. Figure 5.6 shows the dependence of the $d_{33,f}$ piezoelectric coefficient on the ac electric field amplitude and the fitted line to the experimental data points for SL and GF samples. The dielectric and piezoelectric Rayleigh parameters for all of the films are reported in Table 5.3.

SL and GE films exhibited higher irreversible extrinsic contributions—higher α', α_d and $\alpha'/\varepsilon'_{\mathrm{init}}$, α_d/d_{init} - compared to the GF and MLA films. Higher irreversible parameters have been previously observed for rhombohedral vs. MPB and tetragonal compositions in bulk PZT ceramics [140]. However, the deepest rhombohedral composition was observed in MLA films in XPS analysis. The ≥35% increase in $\alpha'/\varepsilon'_{\mathrm{init}}$ for the SL and GE films with respect to the MLA and GF therefore suggests that (rhombohedral) composition contributions to the Rayleigh parameters are not the primary source of such large values. Additionally, higher ratio of the irrversible to the reversible Rayleigh parameters was observed in the GE compared to the SL films. This might be due to the

higher intrinsic dielectric/piezoelectric contributions (leading to higher denominator in the ratio) in the SL films, as a result of having an overall composition closer to MPB, compared to the GE film. Furthermore, the extreme compositions in the GE films are further apart than in the SL films; therefore a higher interlayer stress, due to a larger lattice mismatch, can be expected in GE compared to SL film. A smaller amount of internal stress effectively translates into reduced pinning of the internal interfaces [9], leading to a larger extrinsic contributions at low-fields (larger $\varepsilon'_{\text{init}}$) and therefore an apparently reduced $\alpha'/\varepsilon'_{\text{init}}$. Similar trends are observed in the piezoelectric Rayleigh parameters shown in the table 5.3, suggesting that the same source contributes to the enhancement of the dielectric and piezoelectric response of the SL films.

A large degree of tensile stress was indeed observed in the polarization-electric field (P-E) hysteresis loops of SL and GE films as shown in Figure 5.7. Overall, the remnant polarization, ~12 μC/cm2 in 190 nm-thick SL film is relatively modest, while the coercive field is ~70 kV/cm, which is slightly inferior to other reports for PZT films of similar composition, although with partially lower degree of (100) orientation and larger thickness.[141] This can be due to a higher level of stress at the artificially created phase boundaries. Furthermore, the more pronounced clockwise rotation noticeable in the hysteresis loop of the GE films compared to that of the SL films can be an indication of higher residual stresses in the GE films.[28,136]

In addition to the enhanced dielectric response, SL films exhibited drastically increased piezoelectric response compared to MLA, GF or GE films of similar thickness. Effective $d_{33,f}$ piezoelectric coefficients are reported as averaged response of the films under ~E_c bias field (Table 5.3). The SL film shows ~45% higher $d_{33,f}$ (~95 pm/V)

compared to MLA and GF samples (~65 pm/V), which in turn have higher response than GE films (~45 pm/V). The piezoelectric responses of the MLA and GF films were very close to those previously reported for the ultrathin PZT53 films of similar thickness [26]. It is intriguing to note that the piezoelectric response of the 200nm-thick SL films is comparable to and higher than the literature reported values for submicron-thick polycrystalline PZT films.

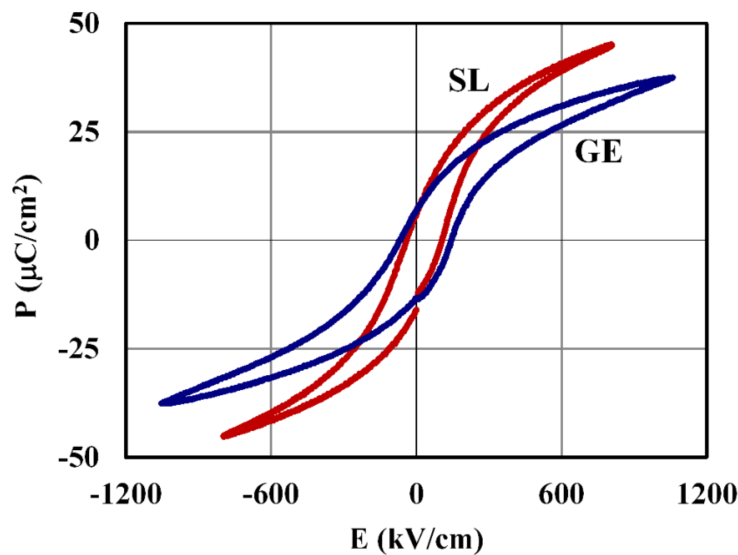

Figure 5.7 Polarization-electric field hysteresis loops for ~200 nm-thick SL (Λ=30nm) and GE films.[36]

Some of the best reported $d_{33,f}$ coefficients to date for ferroelectric thin films (≤1 μm) are those for the (100) and randomly oriented, 1 μm-thick PZT52 films with $d_{33,f}$ = 60-70 pm/V,[129,142] and for the 900 nm thick (100)-oriented PZT53 films with $d_{33,f}$ = 90 pm/V [143] (Figure 5.8). Indeed the $d_{33,f}$ of the SL films is comparable to that reported for the (100)-oriented PZT53, gradient-free films of an order of magnitude higher thickness (2 μm) with a $d_{33,f}$ = 100 pm/V.[144]

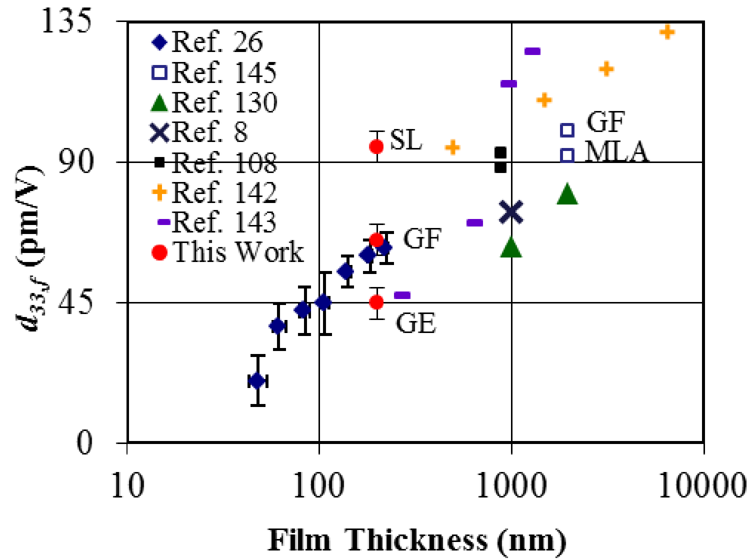

Figure 5.8. Comparison of the piezoelectric response of the ~200 nm-thick PZT films with literature reported values for polycrystalline PZT films, with composition close to MPB, deposited on platinized silicon wafers. PZT films from references 130, 26 and 142 are (100)-oriented, those from reference 143 and 8 are (111)- and partly (111)-oriented and those from reference 145 are almost randomly oriented. Reference 108 reports values for both (100)- and (111)-oriented films with (100)-oriented film having higher piezoelectric response at similar film thickness.[36]

Considering the strong size effects in ferroelectric thin films (reduced piezoelectric coefficients and dielectric permittivity with decreasing thickness)[26,145] the very large piezoelectric coefficients observed in these ultrathin films are another clear indication of an extrinsic, processing-induced contribution to the response of the SL films. The "artificially created" morphotropic phase boundaries are once again the most convincing candidate for such extrinsic contributions to both the dielectric and piezoelectric properties in SL films. In fact, the ferroelastic, non-180° domain walls' motion is very limited for film thicknesses below one micron, while the ferroelectric, 180° domain wall motion can contribute to the piezoelectric response only through a dynamic poling mechanism (high ac fields).[115,146]

5.5 Effects of Stacking Periodicity on the SL Films Properties

SL films with different stacking periodicities were processed and characterized to investigate the possible effect of this parameter on the functional properties of the film. Table 5.4 compares the dielectric permittivity and the polarization-electric field (P-E) hysteresis loops parameters of 150nm-thick SL films. The film with ~30nm periodicity shows higher dielectric permittivity, however, the one with ~60nm periodicity shows slightly higher remanent polarization. It should be mentioned that the extent of the chemical composition variation in the films with different stacking periodicities are not necessarily similar, as the cation gradient formation is a thermodynamically driven phenomenon. Therefore, more parameters should be considered to carefully interpret such data.

Table 5.4. Low field dielectric permittivity (at 1 kHz, 20 mV_{rms}), coercive field (E_c), remanent, and maximum polarization (P_r, P_{max}) values measured for ~150 nm-thick superlattice (SL), films with different stacking periodicities. Low-field dielectric loss values are below 1.7% for all films.

Sample	Λ=17±3nm	Λ=30±3nm	Λ=60±3nm
ε_r	658 ± 20	705 ± 15	602 ± 15
E_c (kV/cm)	104 ± 5	84 ± 4	88 ± 4
P_r (μC/cm^2)	15.7 ± 0.5	15.8 ± 0.6	17 ± 0.6
P_{max} (μC/cm^2)	52.3 ± 1	52.5 ± 1	56.6 ± 1
$d_{33,f}$ (pm/V)	-	-	-

5.6 Neutron Scattering Study

To verify the formation of the artificial phase boundaries across the film thickness and their extrinsic contributions to the films' properties, neutron scattering studies were performed on the SL films.[3] In general, neutron reflectometry experiments provide structural information over a large sample volume and are therefore preferred over local probes such as SEM or XPS.[36] In addition, since neutron scattering experiments are non-destructive, they can be used for in situ experiments, such as under applied electric fields. The use of neutrons to characterize the Zr/Ti composition gradient across the film thickness is justified because of the large difference in the coherent neutron scattering length of Zr (7.16 fm) and Ti (-3.438 fm).[36]

In this study, a 6 layer SL PZT film (200nm-thick) was probed and subsequently modeled with three different phases/compositions on each crystallized layer; [Zr45:Ti55(10nm)/ Zr53:Ti47(10nm) /Zr61:Ti39(10nm)]x6 on the Pt/Ti/SiO_2/Si substrate. The Zr/Ti compositions are chosen based on the XPS results presented previously in Figure 5.4. Modeling of the neutron scattering length density in PZT SL thin film is shown in Figure 5.9. There are six repeating crystallized layers and each one is consisting of three sub layers consistent with the Zr/Ti composition gradient.[36]

Neutron scattering length density, (NSLD) is proportional to the scattering length divided by the volume. The scattering length is proportional to the Zr/Ti ratio and the volume is proportional to the phase. A global gradient in NSLD over six layers of

---

[3] This study has been conducted at Oak Ridge National Laboratories, by Ms. Talia Field and in collaboration with Drs. Abhijit Pramanick and Valeria Lauter.

repeating structures indicates an underlying phase gradient in the multilayer structure, in addition to composition and phase gradients within each sublayer.

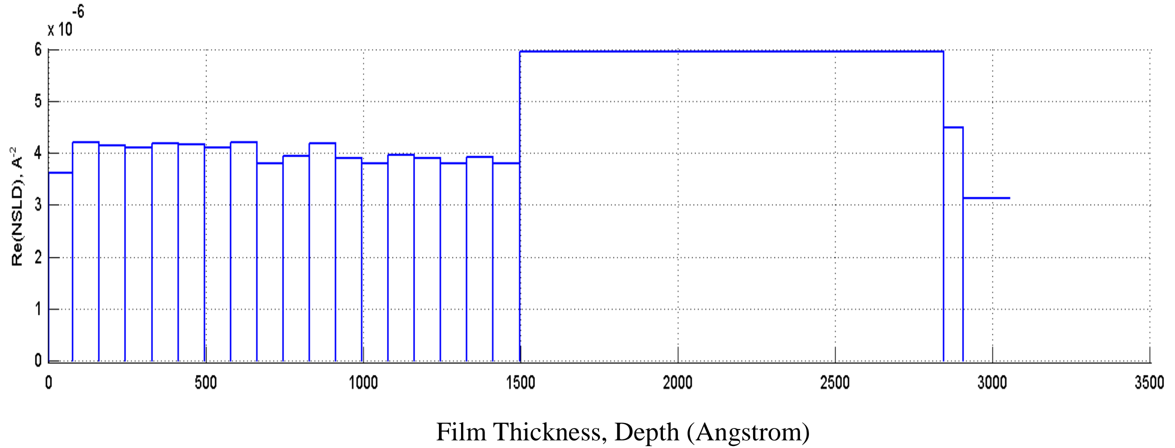

Film Thickness, Depth (Angstrom)

Figure 5.9. Modeling of the neutron scattering length density in PZT SL thin film. There are six repeating crystallized layers and each one is consisting of three sub layers based on Zr/Ti composition gradient.[147]

The calculations show that Zr/Ti distribution across the film thickness has a significant effect on the neutron reflectivity patterns and can be traced experimentally. The close match between the measured neutron reflectivity on the SL PZT thin film and the simulated values based on the model containing alternating tetragonal/MPB/rhombohebdral phases verifies existence of the phase boundaries across the thickness of the films.

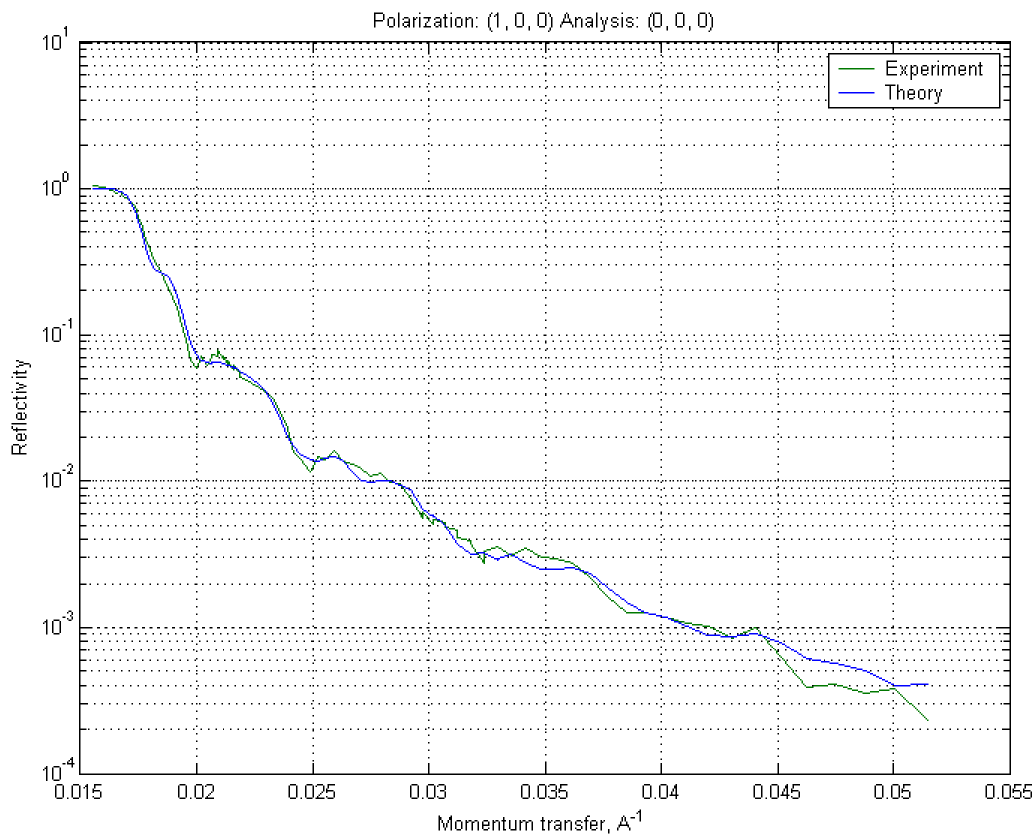

Figure 5.10. Comparison between the measured neutron reflectivity on the SL PZT thin film and the simulated values based on the model shown in figure 5.9.

5.7 Conclusions

Spontaneous Zr/Ti gradient formation during crystallization in CSD-derived PZT films was used to prepare superlattice-like, polycrystalline thin films, with stacking periodicity ranging from 13 to 60 nm. Careful control of processing steps resulted in perovskite-pure, dense films with a smooth surface due to the epitaxial-like, columnar grain growth. The presence of high order satellite peaks in the XRD underlined the quality of the superlattice structure. The superlattice periodicity, as calculated by XRD patterns, was in excellent agreement with the single layer thickness as measured by

profilometry and was considered as another index of the reliability of the proposed processing method. XRD structural refinement and neutron reflectometry studies of the SL films along with XPS depth profile chemical analysis, revealed that the crystal structure switches between in plane tetragonal and rhombohedral phases, creating “artificial” phase boundaries throughout the film thickness.

PZT SLs showed ~20% increase in the dielectric permittivity and ~45% increase in $d_{33,f}$ with respect to GF films. The enhancements were attributed to the extrinsic contributions from the motion of the “artificially-created” phase boundaries between the rhombohedral and tetragonal interfaces. Dielectric and piezoelectric nonlinear studies also confirmed higher amounts of extrinsic contributions to the response in SL and gradient-enhanced films compared to conventionally-processed films of similar average composition. The enhancement of the response clearly depends on the extent of the overall compositional gradient: compositional variations far away from the MPB might hinder constructive phase boundary motion through additional in-plane stresses.

The proposed method for enhancing the piezoelectric and dielectric response of ferroelectric ultrathin films should be applicable to any solid-solution with a polymorphic phase boundary, such as present in many lead-free ferroelectric compositions. Additionally, it might be a way to substantially increase dielectric and piezoelectric response of ferroelectric thin films, which is particularly of interest for NEMS and MEMS active sensors and actuators for miniaturized applications.

Chapter 6

Alternative Material System: lead magnesium niobate-lead titanate thin films

This chapter investigates an alternative material system to PZT for piezoelectric MEMS applications. Processing optimization and characterization of electromechanical properties of highly textured, $0.7Pb(Mg_{1/3}Nb_{2/3})O_3$-$0.3PbTiO_3$ (PMN-PT) films, processed via chemical solution deposition on platinized silicon substrates are the focus of this chapter. Textured perovskite seed layers, optimization of heat treatment conditions and Pb content control were studied to obtain pure-perovskite PMN-PT films with dense, columnar grains. Highly (100)- and (111)-oriented films, with Lotgering factors between 91 and 97%, and average grain size up to ~ 430 nm were synthesized on thin $PbTiO_3$ and $Pb(Zr,Ti)O_3$ seed layers. Dense, submicron-thick, (100)-oriented films showed low-field, relative dielectric permittivity of up to ~2850 and tanδ of 0.02 at 1 kHz, and remanent polarization values up to 17.5 μC/cm^2. The films showed saturated $d_{33,f}$ piezoelectric coefficients as high as 210 pm/V.

6.1 Introduction[4]

As discussed in the previous chapter, there are extrinsic and intrinsic size effects in ferroelectric thin films which limit the dielectric and piezoelectric response of the material at sub-micron sizes. However, with the current advancements in MEMS

[4] The content of this chapter is mainly based on a published work in the Journal of the American Ceramics Society.

technology, it is essential to process ultrathin ferroelectric films with maximized piezoelectric response to integrate into high performance MEMS and NEMS devices.

As discussed in previous chapters, ceramic $Pb(Zr_xTi_{1-x})O_3$ (PZT) thin films have been often the material of choice for piezoelectric MEMS applications, due to their large electromechanical response, especially at morphotropic phase boundary compositions (MPB at x~0.52). In bulk form, [001]-poled lead titanate-based relaxor-ferroelectric single crystals show several times higher piezoelectric response compared to PZT ceramics.[22,148] Therefore, integration of [001]-oriented relaxor-ferroelectric thin films, such as $Pb(Mg_{1/3}Nb_{2/3})O_3$-$PbTiO_3$ (PMN-PT), on Si promises enhancement of the sensing and actuating capabilities of the MEMS devices. The best piezoelectric responses to date have been reported for 1.5 μm-thick, (001)-textured 0.7PMN-0.3PT films on Si substrates, with piezoelectric coefficient $d_{33,f} \approx 180$ pC/N by Park et.al.[33] This is higher than the best $d_{33,f}$ values reported for up to 2 μm-thick, (001)-oriented PZT films (at MPB composition) on Si, ~100 pm/V.[143,144] However, the processing of high performance relaxor-ferroelectric thin films, in particular, has proved to-date extremely challenging.[15] Specifically, they require higher processing temperatures, than do PZT film; these higher temperatures, in connection with the high volatility of Pb, can lead to formation of secondary phases and porosity. Additionally, heterogeneous cation distribution can occur at relatively low growth temperatures of thin films and can lead to a deterioration of the final electromechanical properties of the films. Hence, to effectively use PMN-PT films in high performance piezoelectric MEMS devices, comprehensive processing optimization is required. Few reports in the literature discuss process optimization of oriented PMN-PT films.[24,149,150] Specifically, there has been no extensive study of defect

formation in oriented PMN-PT films' microstructure, such as inter- and intra-granular cracks and porosity, of remedial techniques to limit them, or of their effects on the films' dielectric and piezoelectric properties.

This chapter focuses on the control and optimization of the crystallographic texture and microstructure of 0.7PMN-0.3PT thin films prepared by chemical solution deposition on Si substrate. Perovskite seed layers, optimization of the processing heat treatment profile, and Pb content control were rigorously studied to achieve phase purity, texture control, and elimination of cracks and porosity in the films. Low field dielectric, polarization-electric field ferroelectric hysteresis, and piezoelectric response of the films were also studied as a function of crystallographic texture and microstructural properties.

6.2 Experimental Procedures

The precursor solution of $0.7Pb_{1.15}(Mg_{1/3}Nb_{2/3})O_3$-$0.3Pb_{1.15}TiO_3$ nominal composition (i.e. 15 mol% excess lead with respect to stoichiometry) was synthesized as explained in chapter 2, following a route based on 2methoxyethanol (2MOE) solvent, described by Park et al.[33] Films were deposited on platinized silicon wafer, substrate/SiO_2(1 μm)/Ti(20 nm)/Pt(150 nm). The polycrystalline Pt film was deposited using a Unifilm sputtering system, and was strongly (111)-oriented.[151] A thin (~30 nm) single layer sol-gel derived PT or PZT film was first deposited as a seed/buffer layer (see section 3.5.2). The PT or PZT 0.2M precursor solution was spun onto the substrate at 3000 rpm for 30 s as explained in chapter 2. Subsequently, the 0.4M PMN-PT precursor solution was dispensed through a 0.1μm filter onto the buffered substrate and spun at 3000 rpm for 30 s. The samples were pyrolysed after each deposition, on a hot plate at

360˚C for 1 to 3 min, and crystallized every four layers in a rapid thermal annealer for 2 minutes. Crystallization temperature varied from 750˚C to 850˚C as will be further discussed.

Standard θ-2θ x-ray diffraction with Cu Kα radiation was performed on the prepared samples for crystal structure and texture identification. The Lotgering factor[38] was used to characterize the degree of crystallographic texturing of the films, by comparing measured peak intensities from the films with powder PMN-PT diffraction data.[152]

6.3 Results and Discussion

6.3.1 Film texture and microstructure

A thin PT or PZT buffer layer enhances nucleation of PMN-PT at lower temperatures, due to a good match in lattice parameter and crystal structure,[33,153] stabilizing the perovskite phase in the PMN-PT film. If the PT/PZT films are textured, they can also induce a preferential orientation to the PMN-PT film. Additionally, the textured buffer layer, if of sufficiently dense microstructure, can also prevent excessive Pb diffusion into the substrate.[154,155] Previous studies have reported processing of highly (100)- and (111)-oriented PMN-PT films (around MPB composition) respectively using thin PZT/PbO [153] and PT [33] layers. Both (100)- and (111)-oriented PMN-PT films were processed indiscriminately on PZT and PT buffer layers.

Deposition of PMN-PT on substrates with a thin PT buffer layer, led to (111)-oriented PMN-PT films with Lotgering factors[38] ranging from 91 to 96%. To obtain

highly (100)-oriented PMN-PT films on PT buffer layer, a very thin PbO layer was deposited first. 0.02M PbO precursor solution was spin coated onto the substrate at 4000 rpm for 30 s, prior to PT deposition. The samples were then heat treated on a hot plate at 400°C for 10 min, but were not annealed separately from the PT film. PMN-PT films processed on PbO/PT buffer layer show (100) orientation, with Lotgering factors exceeding 94% (up to 97%).

Deposition of PMN-PT on samples with thin (100)-oriented PZT buffer layer led to (100)-oriented PMN-PT films having Lotgering factors of about 91%. Highly (111)-oriented PMN-PT films on PZT buffer layer were prepared by pre-heat treating the platinized silicon substrate at 500°C in oxygen environment for 5 min before any perovskite film deposition. Lotgering factors of these (111)-oriented PMN-PT films were ~91%. The substrate heat treatment has been previously been reported to lead to diffusion of Ti from the adhesion layer of the bottom electrode stack to the surface, leading to formation of TiO_x nuclei on the surface of the substrate.[156] Development of (111) textured perovskite ferroelectric films on thin TiO_x templates has also been previously reported in literature.[1]

Figure 6.1 shows the X-ray diffraction patterns of (100) and (111)-oriented PMN-PT films on both PT and PZT buffer layers. For reference, the XRD pattern of a PMN-PT film without any buffer layer is also shown. The absence of buffer layers led to secondary phase creation, as evidenced by a broad peak at 2θ=29°, tentatively associated with a fluorite type structure.

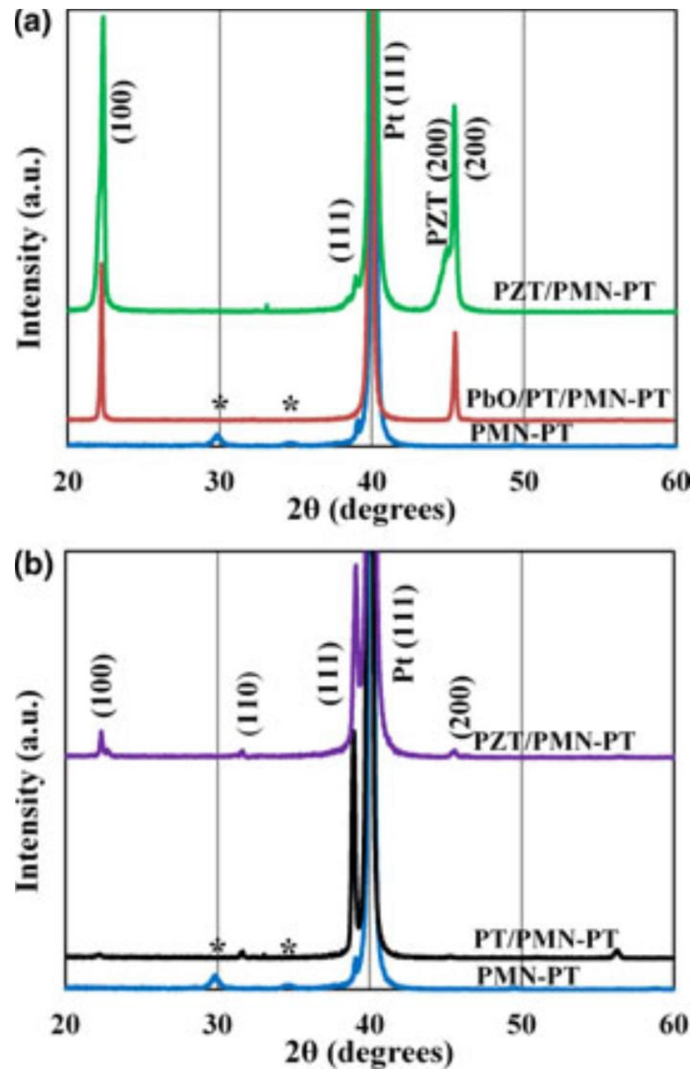

Figure 6.1. XRD patterns of (100)-oriented (a) and (111)-oriented (b), ~600 nm-thick PMN-PT films on both PT and PZT buffer layers compared to the diffraction pattern of a PMN-PT film, deposited without any buffer layer. Asterisk marks represent fluorite peaks in the PMN-PT film with no buffer layer.[61]

Creation of such secondary phases might indicate excessive Pb loss at the crystallization temperature, through evaporation or through diffusion into the substrate. No secondary phase-related peaks were visible in the patterns of PMN-PT films prepared on buffer layers, which confirms the reduction of Pb loss into the substrate through use of dense buffer/seed layers. In order to compensate for the excessive Pb loss, pyrolysed PMN-PT multilayers were covered with a dilute PbO layer (0.02M spun at 4000 rpm)

prior to crystallization. On the other hand, use of higher amounts of excess Pb in the precursor solution led to creation of PbO "pockets" within the film thickness, resulting in overall higher leakage currents. The "ruse" of the PbO film cover-coat allows compensation for the Pb loss only in the location of the highest Pb volatility, i.e. the film surface.[130] This processing technique led to pure perovskite phase formation with a dense columnar microstructure, in addition to an increase in grain size for films of thicknesses below 500 nm (Figure 6.2c). No PbO-associated peaks were observed in the XRD data from the films, nor were any secondary phases observed in the SEM images.

At increasing film thicknesses (above 600 nm), however, new microstructural defects appeared. Cracks and porosities, both at the inter- and intra-granular levels, were observed in the surface and cross-sectional SEM images (Figure 6.2(d)-(e)). Crack formation may be due to the residual stresses developed in the film. Tensile residual stress in lead-based perovskite ferroelectric films on Si substrate has been attributed to both the thermal expansion coefficient mismatch between the film and Si,[157] and the spontaneous strain due to ferroelectric distortion during cooling through the Curie temperature.[1] Similarly, different mechanisms can contribute to formation of pores in a thin film. The presence of residual organics after pyrolysis, followed by rapid crystallization or grain growth without sufficient time for densification, may result in inter-granular porosity (Figures 6.2(d)-(f)). Porosity formation within crystal grains has also been previously observed in sol-gel processed 0.9PMN-0.1PT thin films and attributed to insufficient densification caused by fast crystallization.[150]

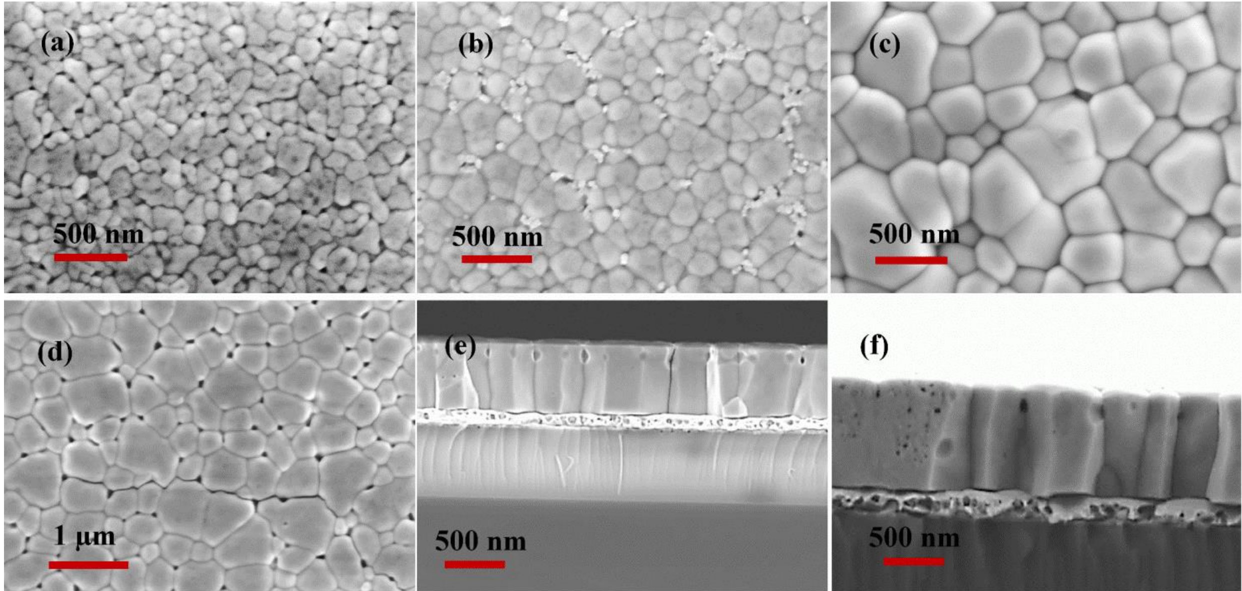

Figure 6.2. FE-SEM surface morphology of 300 nm thick, PMN-PT films, crystallized at (a) 750°C, (b) 800°C, and (c) 800°C with a PbO cover coat on the surface prior to each crystallization step. (d) At higher film thicknesses, >600 nm, cracks and porosity are observed on the surface of the films processed at 800°C. (e) Intra-granular pores formed between grains beyond a critical film thickness (≥600 nm), and (f) inter-granular pores inside the grains are shown in the cross sectional views of the thick PMN-PT films.[61]

Thicker PMN-PT films also developed a rough surface topography, consisting of dome-shaped, large grains (average size ~ 430 nm, based on average intercept length method[158]). Development of such microstructure might be directly correlated with the induced fiber texturing of the films and with different growth rates in different crystallographic directions. The symmetry-related <100> are the thermodynamically favored growth directions in many ferroelectric perovskite thin films.[63,159-161]

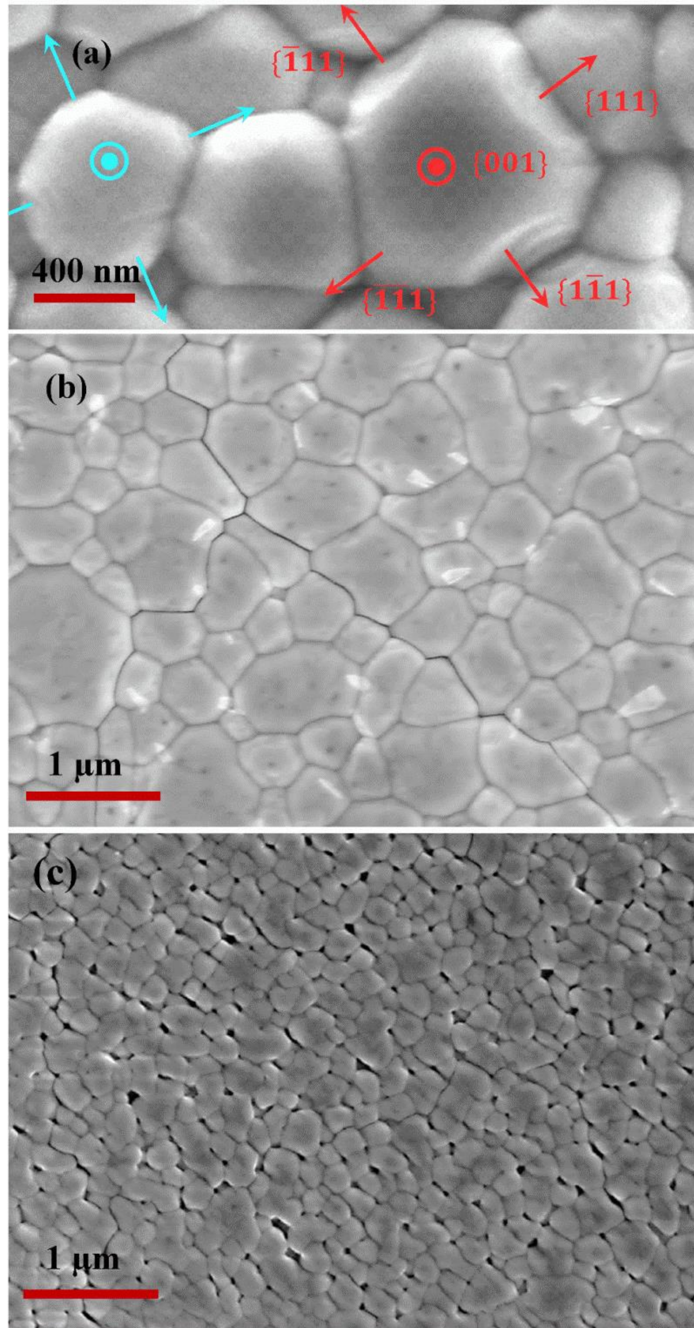

Figure 6.3. (a) Surface topography of a 600 nm thick, (100)-oriented PMN-PT film, consisting of dome-shaped grains. Slow growing (111) atomic planes surround small top (100) facets of the grains. (b) A 900 nm-thick, (001)-oriented PMN-PT film processed with faster annealing ramp rates (~100°C/s), longer pyrolysis time (3 minutes), crystallization at higher temperature (850°C), and use of PbO cover-coat prior to each crystallization, resulting in elimination of surface porosity. (c) Presence of a lower dwell temperature (700°C) in a multi-ramp annealing temperature profile led to an increase in the film porosity regardless of the 850°C final annealing temperature.[61]

The continuous heterogeneous nucleation of the successively deposited layers on the previous ones, ensured a columnar (100) growth of the grains. However, the {111} and {110} families of planes can still partially determine the final morphology of the crystals, in the same way as in the well-known rutile needles. This behavior is particularly noticeable in highly (100)-oriented PMN-PT films, as shown in Figure 6.3a. Such rough surface topography can also lead to void entrapment in the spaces between dome-shaped grains during crystallization of subsequent layers and therefore, formation of intra-granular porosity, as shown in Figure 6.2b. Indeed pores are observed in the cross sectional view of the thicker films, concentrated at specific film thicknesses, close to the interface between subsequent crystallization layers.

For films thicker than 600 nm, higher crystallization temperatures (850°C), extended pyrolysis time (3 min), and use of a PbO cover-coat led to extensive reduction of porosity and cracks (Figure 6.3b). Different annealing ramp rates were also examined, and best results were obtained with higher ramp rates, ~100°C/s, than were used for thinner films. Although lower ramp rates did not lead to the loss of preferential crystallographic orientation of the films, they were associated with a high number of volume and line defects throughout the film thickness. This observation suggests that the heterogeneous nucleation is not affected by the ramp rate, and that the observed reduction of defects at higher ramp rates is not associated with nucleation events. However, variations in ramp rates can induce different grain growth dynamics at different temperatures. Grain growth processes in ferroelectric thin films are reported to be extremely fast (a few seconds) at processing temperatures as low as 600-700°C.[63] However, lower diffusion and mobility of the atomic species can be expected during

grain growth at lower temperatures, which will lead to a lower density of the films processed with low ramp rates or at lower crystallization temperatures. Additionally, if the grain growth process is completed at lower temperatures, no densification is expected at yet higher temperature, within the range available for films processed on Si (typically below 850°C, as Si's melting temperature is ~1400°C). This was indeed confirmed in samples processed with a multi-ramp annealing temperature profile, where the presence of a low temperature dwell time (such as at 700°C) led to an increase in the film porosity regardless of the final dwell temperature for crystallization (Figure 6.3c). Higher annealing ramp rates allow for completion of the grain growth at higher temperatures, where the diffusion and mobility of the atomic species is also higher, leading to a denser microstructure with bigger grains (Figure 6.3b). Additionally, a longer pyrolysis time allows further organic removal prior to the crystallization. Increased Pb content as a flux agent,[162] resulting from a PbO cover-coat, can also improve the diffusion and material flow during grain growth. Especially 850°C crystallization temperature is higher that Pb solidus temperature of 833°C in $PbTiO_3$ phase. This enables formation of small amounts of liquid Pb-rich phase during crystallization, leading to elimination of porosity. However, some surface hairline cracks were still observed in our thickest films.

6.3.2 Dielectric and Piezoelectric Characterization

The low-field dielectric permittivity of the PMN-PT films is presented in Figure 6.4 as a function of preferential crystallographic orientation of the films and buffer layers. In general, the effect of buffer layer seems to be minimal. Films with PZT buffer layer had slightly higher dielectric permittivity, probably due to the higher permittivity of PZT

compared to PT. (100)-oriented PMN-PT films showed higher dielectric responses than the (111)-oriented ones. The anisotropic dielectric response in PMN-PT has been previously reported for bulk single crystals as well as polycrystalline thin films.[33,163] Additionally, (100)-textured films with denser microstructure exhibited higher dielectric permittivity (ε_r~2850, for 900 nm thick film). Porosity is indeed expected to dilute the dielectric permittivity due to the inclusion of the low-permittivity phase (air), effectively creating a ferroelectric/air composite with 3-0 connectivity.[164,165]

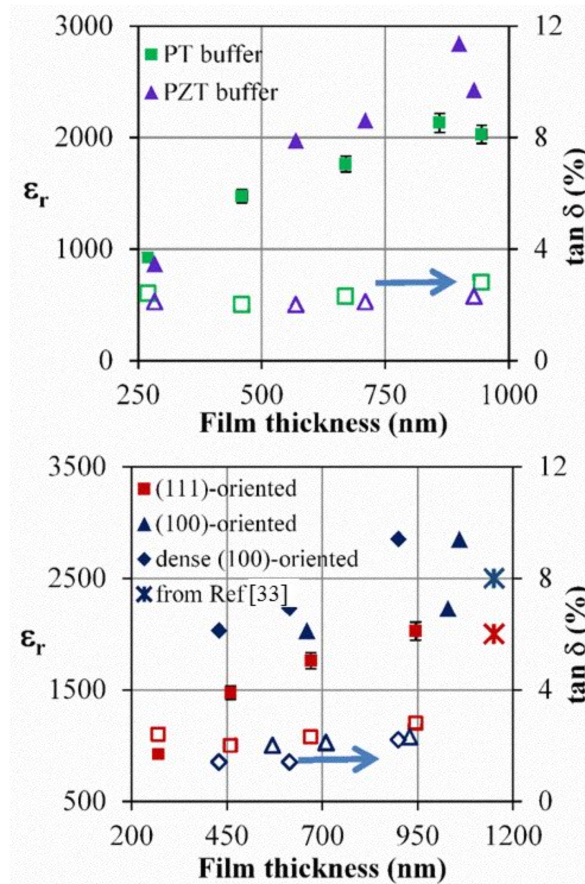

Figure 6.4. Low-field dielectric permittivity of the PMN-PT films as a function of thickness (Top) for PMN-PT films with thin (30 nm) PT or PZT buffer layers, and (Bottom) for different preferential crystallographic orientation, when processed on thin PT buffer layer. Hollow symbols represent tanδ values, while filled symbols represent the dielectric permittivity. The measurements were carried out at 1 kHz and 20 mV_{rms}.[61]

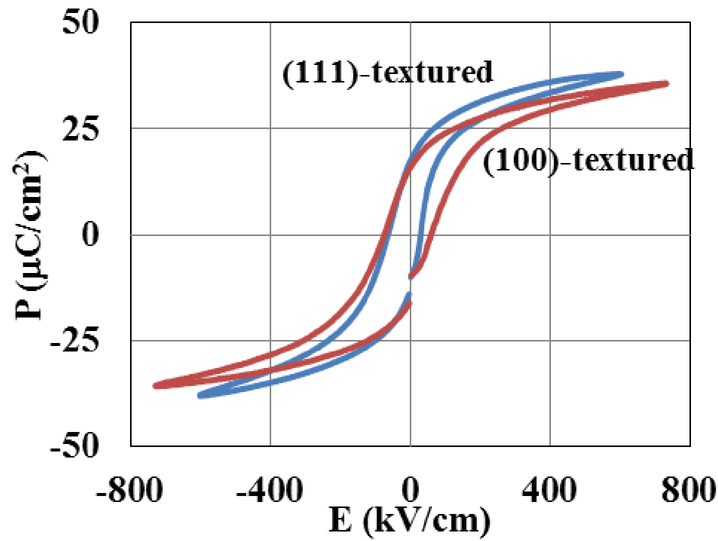

Figure 6.5. Polarization-electric field hysteresis loops for ~900nm-thick PMN-PT films on PT buffer layer, with different textures.[61]

Figure 6.5 shows the polarization-electric field (P-E) hysteresis loops for 900 nm-thick, PMN-PT films, processed on PT buffer layers, with (111) and (100) preferential orientations. The (111)-oriented films showed higher saturation polarization compared to the (100)-oriented one. Indeed in rhombohedral PMN-PT, the (polarization) measurement direction is parallel with the (111) crystallographic axis. Therefore, higher saturation and remanent polarization values are expected in (111)-oriented films with respect to (100)-oriented films. P_r values for (100)-oriented films of 0.5 to ~1 μm thickness ranged from ~13.5 to ~17.5 μC/cm^2. These are comparable to the best reported P_r values in literature, for epitaxial (001)-oriented PMN-PT films (1.5 to 2 μm thick) on $LaAlO_3$ (~13-19 μC/cm^2).[149]

PMN-PT films with PT buffer layers had overall higher P_r values, than those with PZT buffer layer. This might stem from a denser microstructure in PT, compared to PZT buffer layer, which might be due to nucleation and growth activation at lower temperatures in PT compared to PZT (Figure 6.6). It should also be noted that tetragonal

PT (a_0=3.90 Å)[166] has larger lattice mismatch with 0.7PMN-0.3PT (a_0=3.96 Å), compared to PZT 53/47 (a_0=3.99 Å).[167] Lattice mismatch between PT and PMN-PT layers could induce a compressive stress in PMN-PT film, leading to enhancement of remnant polarization in PMN-PT films. However, such an enhancement is expected to be minimal due to: 1) relative thicknesses of the seed layer vs. the PMN-PT film and the Si substrate; and 2) possible "absorption" of the PT seed layer into the ferroelectric-PT based solid solutions[38].

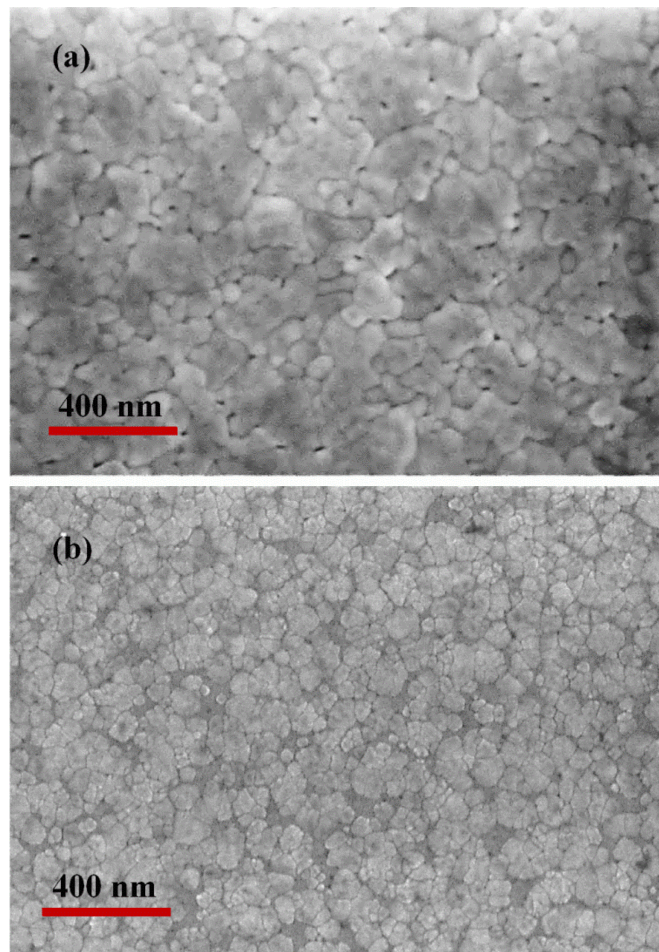

Figure 6.6. FE-SEM surface topography of the 30 nm-thick, sol-gel deposited (a) $PbTiO_3$, and (b) $Pb(Zr_{0.53}Ti_{0.47})O_3$ films used as seed/buffer layers for PMN-PT films.[61]

A decrease in the coercive field with increasing PMN-PT film thickness was observed as shown in Figure 6.7. Overall, coercive field values ranged from ~130 kV/cm for the thinnest films, decreasing with increasing film thickness, to saturating at ~20 kV/cm for films of above 500 nm thickness. This trend is typical in ferroelectric thin films[26] as was also shown in chapter 4 for PZT films, and is attributed to weaker and/or lower concentration of pinning centers, and in turn higher mobility of the domain walls, in thicker films. Such increase in the mobility of the internal interfaces is also associated with a reduction in the overall residual stresses in the films with their increasing thickness[12].

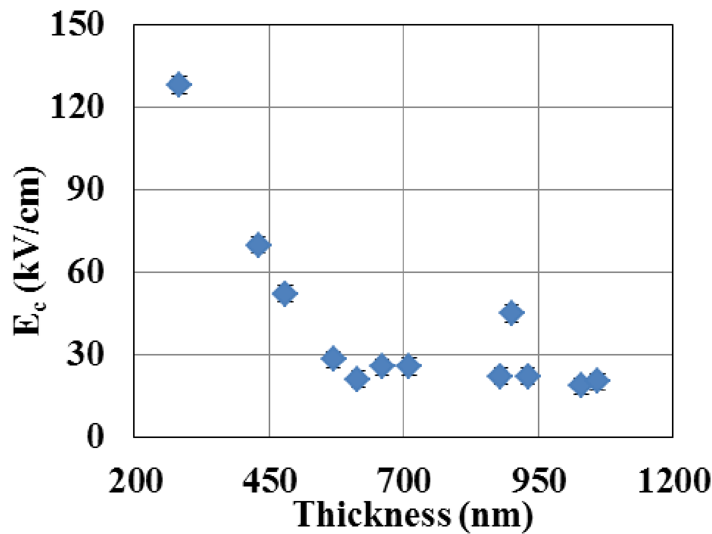

Figure 6.7 Thickness dependence of the coercive field for PMN-PT films on PT buffer layer.[61]

Pt and Cr/Au were used to create top electrodes, resulting in symmetric (Pt/PMN-PT/Pt) and asymmetric (Pt/PMN-PT/Cr/Au) metal-oxide-metal configurations. All samples showed negative imprints in their ε_r - E and $d_{33,f}$ – E measurements, as shown in

Figure 6.8. The negative imprint increased the positive P_r and remanent $d_{33,f}$ coefficients, while decreasing ε_r at zero field.

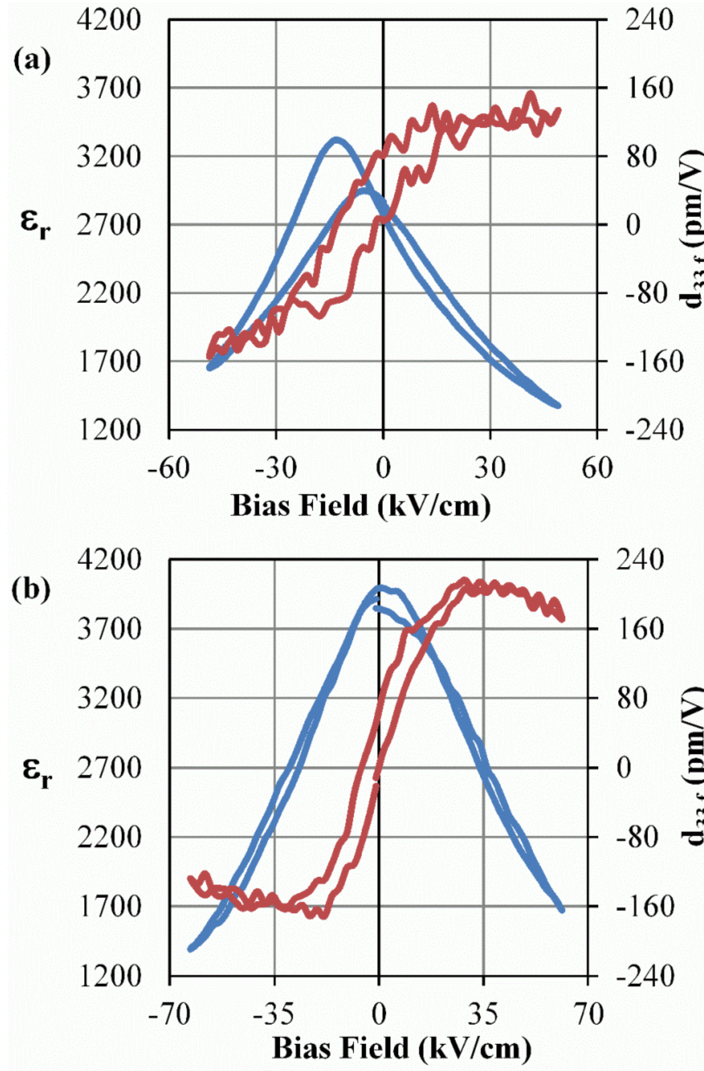

Figure 6.8. The relative dielectric permittivity (C-V measurements) as well as d33 piezoelectric coefficient as a function of bias electric fields, for (100) textured films for (a) 900 nm-thick PMN-PT film in, Pt/PZT/PMN-PT/Cr/Au configuration, and (b) 730 nm-thick PMN-PT film in, Pt/PZT/PMN-PT/Pt configuration. Piezoelectric measurements were conducted with $V_{ac} = 0.2V_c$ (coercive voltage) at 1 kHz under dc electric bias field of up to $2E_C$.[61]

Additionally, the thickness-dependent internal bias observed in the films with asymmetric electrode configuration was 2 to 4 times larger than in films with symmetric

electrode materials (Figure 6.9), confirming that electrode asymmetry enhances the built-in electric field in the films.[68,168] This is attributed mainly to the difference in work function between the electrodes and the ferroelectric layer, resulting in different built-in voltages at the film-electrode interface.[169,170] Other mechanisms reported to cause an internal bias in ferroelectric films are aligned V_O-V_{Pb} defect dipoles,[171,172] and strain gradient.[169,173] Due to the PbO cover-coat in the films' processing, low concentrations of surface Pb vacancies (and consequently defect dipoles) are expected. Therefore, strain gradients in the films, as well as the existence of an inhomogeneous ferroelectric buffer layer (PT or PZT) adjacent to the bottom electrode, are probably the major sources of the relatively small imprint in the samples with symmetric electrode configuration. It should be noted that B-site cation segregation in ferroelectric solid-solution films through the thickness of each crystallized layer[68] as discussed in chapter 5, could be another source of internal bias.

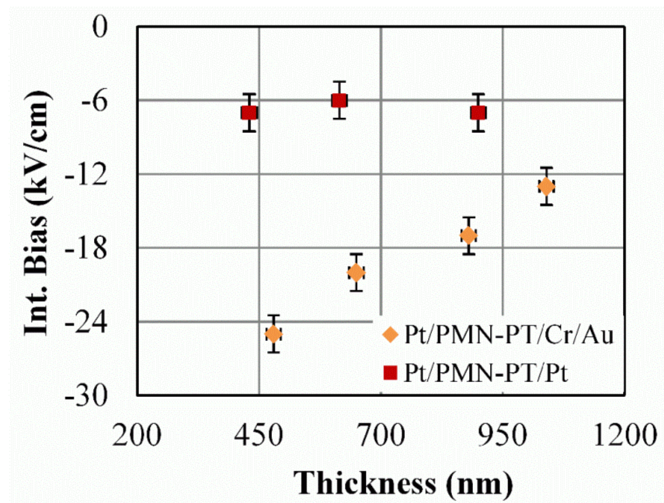

Figure 6.9. Thickness dependence of the built-in voltage (imprint) in (100)-oriented PMN-PT films on PT buffer layer with symmetric versus asymmetric electrode stack configurations. The values were calculated based on asymmetry in coercive fields in P-E hysteresis loops.[61]

Figure 6.10 shows the (positive) remanent and saturated effective piezoelectric coefficients, $d_{33,f}$, for PMN-PT films as a function of film thickness. Saturated $d_{33,f}$ values are the maximum averaged response under a bias field approximately equal to the coercive value, while remanent $d_{33,f}$ coefficients are measured after removal of the (positive) electrical bias at zero field. The saturated piezoelectric response of the (100) and (111)-oriented films increased with increasing thickness.

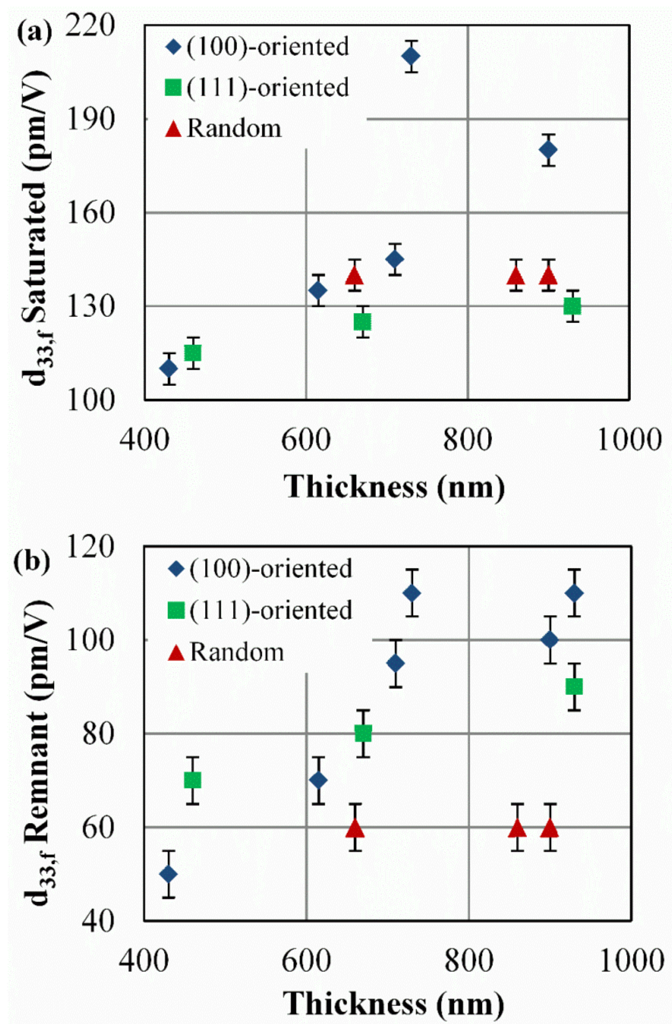

Figure 6.10. (a) Saturated, and (b) remanent effective d33,f piezoelectric coefficients of the PMN-PT films as a function of thickness and preferential crystallographic orientation of the films.[61]

Overall, films with (100) preferential orientation showed the highest saturated piezoelectric response. Effective piezoelectric $d_{33,f}$ as high as 180 to 210 pm/V were observed for PMN-PT films within 700 to 950 nm thickness range. These values are larger than the best results to date for polycrystalline PMN-PT films on Si: $d_{33,f} \approx 180$ pC/N for 1.5 μm-thick, (001) textured 0.7PMN-0.3PT films.[33] (100)-oriented films showed also higher remanent $d_{33,f}$ values, ~100 pm/V with respect to (111)-oriented and randomly oriented films. A direct comparison of the remanent and the saturated piezoelectric response shows a larger "retention" of the saturated $d_{33,f}$ to zero field (remanent) value in the case of the Cr/Au top electrode samples with respect to the Pt top electrode samples; this is consistent also with the higher positive remanent polarization in these films, resulting from built-in electric fields.

Porosity has been previously reported to adversely affect $e_{31,f}$ piezoelectric coefficient,[174] without substantial effects on $d_{33,f}$. In special cases, due to decreased in-plane mechanical stiffness, porosity can lead to increases in $d_{33,f}$.[1,129] However, in our observations, films with higher levels of porosity showed lower remanent polarization, dielectric permittivity and $d_{33,f}$. In fact, we observed that films with good microstructural characteristics -dense, columnar grains and minimal porosity- had up to 40% and 20% higher saturated piezoelectric coefficient and dielectric permittivity respectively, compared to samples of non-optimized microstructure. This indicates that, contrary to previous reports, an increase in porosity does not lead to an increase in the piezoelectric $d_{33,f}$ response of these samples.[1]

6.4. Summary and Conclusions

0.7PMN-0.3PT thin films with both (100) and (111) preferential crystallographic orientation were prepared by chemical solution deposition. Optimization of the thin film processing conditions was pursued, focusing on phase purity, texture control and films' microstructure. Highly oriented films with pure perovskite phase were synthesized, by using PZT and PT buffer layers, and Pb-content control was accomplished through the use of PbO cover-coats. Control of the crystallization kinetics and completion of the organic removal and densification, i.e. extended pyrolysis times and high crystallization temperatures with high ramp rates, played an important role in the films' final microstructure. The dense, crack-free microstructure, maintained through the film thickness in textured PMN-PT films, led to very large piezoelectric response as well as high dielectric permittivity, and remanent polarization. Metal-oxide-metal asymmetry led to an increased internal bias in P-E and piezoelectric hysteresis loops. This in turn, led to increased positive remanent polarization and piezoelectric response. Therefore, asymmetric electrodes can be utilized as a technique to enhance the remanent piezoelectric response for PMN-PT-based MEMS devices working in d_{33} mode.

Chapter 7

Effects of the Substrate Clamping on the Dielectric and Piezoelectric Response of the Ferroelectric Thin Films

As discussed in previous chapters long-range strain fields induced by the substrate profoundly affect the microstructural characteristics and domain structure of ferroelectric thin films. This in turn drastically influences their functional properties. This chapter investigates the effects of substrate clamping on the dielectric and piezoelectric response of the highly (100)-textured PZT and PMN-PT thin films on platinized Si substrate. This was implemented by progressively etching the Si substrate from the back-side in multiple steps, from the original 500 μm to a residual Si thickness of 10-20 μm.

Substrate-released, PZT films showed 4±1% higher low-field dielectric permittivity and 10±3% higher remanent polarization with respect to virgin samples, while the piezoelectric $d_{33,f}$ coefficient increased by at least one order of magnitude from ~75-200 pm/V(for different PZT film thicknesses ranging from 300 nm to 1 μm) to ≥4500 pm/V at reduced Si thickness. Additionally, nonlinear dielectric measurements revealed a 45 to 85% increase in the irreversible dielectric Rayleigh coefficient for substrate-released compared to substrate-constrained PZT films, while no substantial changes were observed in the reversible dielectric Rayleigh coefficient, indicating larger extrinsic contributions to the dielectric response of the films (partially) decoupled from the substrate. BE-PFM investigations revealed a change in the microscopic electromechanical activity between the released and clamped films; the large-scale

clusters of highly active versus not-active or less-active grains in the clamped samples were substituted with individually active grains in the released PZT film.

PMN-PT films also showed a modest increase in their dielectric permittivity and remanent polarization, but the enhancement was mostly limited to (≤2500 pm/V) which is lower compared its PZT counterpart. Different enhancement mechanisms could be active for PZT compared to PMN-PT samples. The increased mobility of ferroelastic interfaces, such as domain walls and phase boundaries, is expected to play an important role in the observed enhancement in the piezoelectric response.

7.1 Introduction

As discussed in detail in chapter 3 PZT thin films on Si substrate are usually subject to residual biaxial tensile stress. Shrinkage and densification during pyrolysis, lattice mismatch and thermal expansion coefficient mismatch with the underlying substrate, as well as the spontaneous strain developed at the Curie temperature transition are some of the sources of residual stress in ferroelectric oxide thin films.[55] The tensile residual stress in the polycrystalline films is usually on the order of a few hundreds of megaPascals.[58,67,104] B-site cation gradient formation during crystallization in chemical solution deposited (CSD) solid solution films can also contribute to the residual stresses in PZT films, as discussed in chapter 5.

Overall, it has been shown before that the long-range elastic interactions between the ferroelectric film and the substrate and within the film itself have drastic effects on the dielectric and piezoelectric responses of the film. To study these “substrate clamping”

effects, different approaches have been used to date. Zhu et al. investigated the effect of applied stress on the dielectric properties of PZT thin films on Pt-Si substrate and reported a decrease in saturated and remanent polarization (in P-E hysteresis loops) when films were subjected to compressive hysdrostatic pressure up to 1.5 GPa.[175] In another work, the wafer bending method has been used to exert biaxial tensile strain on PZT films on Ir-electroded Si wafers.[176] It was shown that biaxial tensile strains as low as 0.08% reversibly reduced the remanent polarization of PZT films by up to 14%, while the capacitance only changed by ~4%.[176] Others have reported a decrease in the film's dielectric permittivity in response to tensile residual stress.[104]

An alternative approach to study the effects of substrate clamping on the ferroelectric films' properties is to change the thickness of the film or the substrate. Effects of the residual stresses have been observed in the evolution of the shape of the polarization-electric field hysteresis loops as the thickness of the film decreases, especially below 100nm. Lower maximum and remanent polarization and larger coercive filed values exhibits a clock-wise rotation of the hysteresis loops of ultrathin PZT films as discussed in chapter 4 (Figure 4.3).[26] This manifestation is accompanied by severe degredation in the dielectric permittivity and the piezoelectric response of the films at lower film thicknesses, which is affected by strong clamping effects. Partal relaxation of the residual stresses in thicker films alleviates these effects.[112]

Suzuki et al. showed 400% and 18% increase in the $d_{33,f}$ and dielectric permittivity of CSD-derived PZT (Zr/Ti:30/70) films, respectively, when they were deposited on thinner Si substrate (Si thickness ranging from 500 to 50 μm).[177] Back-side etching of the Si substrate can also partially relax the residual stresses in the ferroelectric

film, resulting in variations in the properties. This approach mimics the final state of such films for MEMS applications, where the Si substrate is mostly removed in order to have a free-standing or semi-free standing ferroelectric cantilever or membrane. Ohno et al.[178] reported a 10% increase in the dielectric response of the back-side etched lead titanate films compared to virgin samples. However, PZT films have superior electromechanical response with respect to PT films (see Table 1.1) and therefore are strongly preferred for MEMS applications. In this study, we investigate the effects of substrate clamping via back-side Si etching on highly (100)-oriented polycrystalline PZT films' dielectric and piezoelectric response.

7.2 Experimental Procedures

Highly (100)-textured PZT and PMN-PT thin films with 1 μm final thickness were processed based on the routes described in Chapter 2 and 6, respectively. The Bosch Si etching process (chapter 2) was used to back-side etch the substrate in multiple steps, using an inductively coupled plasma etcher, STS-ICP. The etch rate was ~0.6±0.05 μm/cycle, where each cycle consisted of 8s of passivation and 10s of etching.

7.3 Results and Discussion; PZT Membranes

7.3.1 Macroscopic Dielectric Response

Table 7.1 shows the low field dielectric response, polarization-electric field (P-E) hysteresis loop and effective $d_{33,f}$ piezoelectric coefficient of the films measured at virgin (Si thickness=500μm) and substrate-released conditions (Si thickness=10-20μm), as a function of PZT film thickness. On average, low field dielectric permittivity and remanent polarization increased by 4±1% and 10±3%, respectively, while the piezoelectric coefficient showed more than an order of magnitude increase upon

reduction of the Si substrate's thickness (piezoelectric response will be discussed in next section).

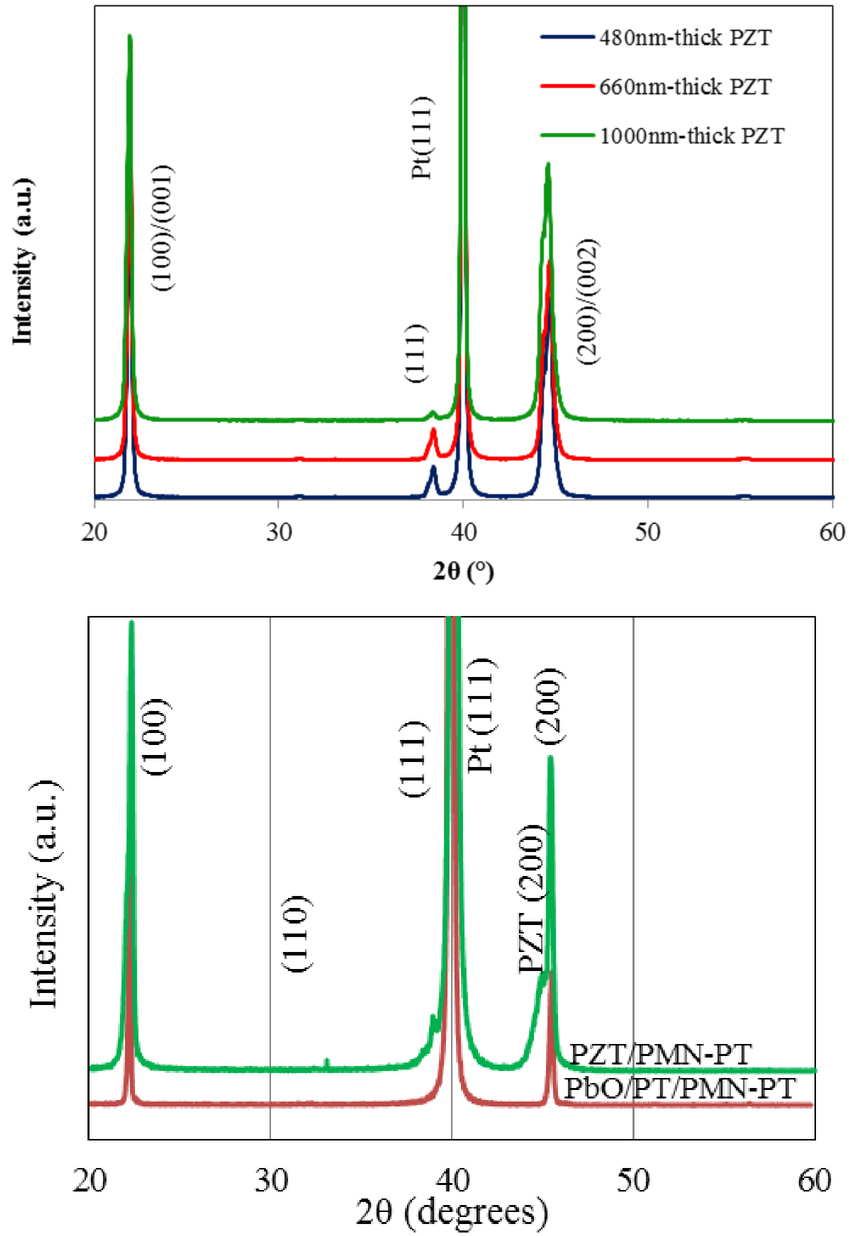

Figure 7.1. XRD patterns of (100)-oriented PZT (top) and PMN-PT (bottom) films used to prepare the membranes.

Table 7.1. Low field dielectric permittivity (ε_r @ 20mV_{rms} ,±3%), reversible (±3%) and irreversible (±5%) Rayleigh parameters, P-E ferroelectric hysteresis loop parameters (±5%) and effective piezoelectric coefficient (±10%) of clamped (substrate constrained, Virgin) vs. membrane (Released) PZT capacitors of different thicknesses.

PZT Thickness (nm)	Form	ε_r	tan δ (%)	α′ (cm/kV)	ε'_{init}	P_r (μC/cm^2)	P_{max} (μC/cm^2)	E_c (kV/cm)	$d_{33,f}$ (nm/V)
300	Virgin	830	1.6	4.1	802	12.5	41	84	0.075
480	Virgin	1015	1.6	14.5	900	24	60	92	0.1
660	Virgin	1178	1.3	19.8	1043	36.4	61.4	90	0.14
1000	Virgin	1160	1.8	32.0	1170	37	63	94	0.2
300	Released	840	1.6	5.9	796	13.8	42	84	2.2
480	Released	1063	1.6	20.1	901	25.8	60	88	3
660	Released	1230	1.3	35.7	1035	38.2	62	94	3.5
1000	Released	1230	1.8	51.1	1140	40	63	90	4.5

Figure 7.2 compares the relative dielectric permittivity (ε_r) as a function of the DC electric field, E_{DC}, for a 1090 nm-thick PZT film, before and after partial Si substrate removal. The shapes of the ε_r-E loops (C-V measurements) associated with virgin and substrate-released films (Figure 7.2b) can also be compared to obtain information on various switching processes in these two states. The ε_r of the virgin and the substrate-released samples are very close at high bias fields, where the domain walls are mostly removed or fixed under the high bias voltage. However, the released samples show higher ε_r at low bias fields, where domain walls and phase boundaries are still mobile.

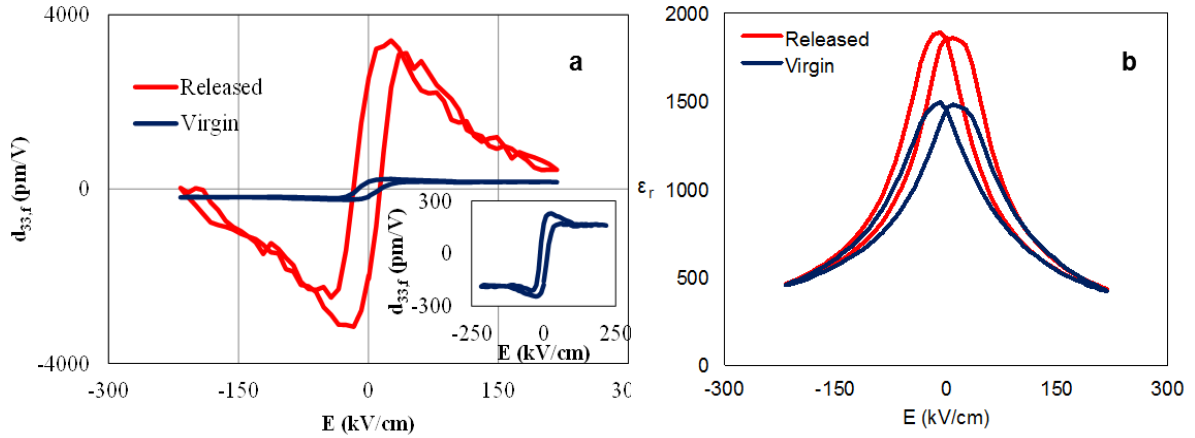

Figure 7.2. (a): $d_{33,f}$-E_{dc} hysteresis curves and (b): Capacitance-E_{dc} (C-E curve) for a 1 μm-thick PZT capacitor in clamped state (virgin) before Si etching, and after etch in membrane form (released). The inset in (a) shows a zoomed view of the $d_{33,f}$-E_{dc} hysteresis curve of the virgin capacitor.

Nonlinear dielectric studies in the framework of Rayleigh analysis[9] also confirmed a higher irreversible Rayleigh parameter, α', i.e. higher irreversible extrinsic contributions to the dielectric response in the substrate released compared to the contribution of virgin film, while the reversible Rayleigh parameter, ε'_{init}, remained fairly constant (Figure 7.3). On average, both α' and $\alpha'/\varepsilon'_{init}$ of the substrate released film increased by 45 to 85% compared the values found in virgin samples. This indicates higher density and/or mobility of the domain walls as an effect of removal of the substrate-induced constraint force. This observation is consistent with the conclusions drawn from the C-V curves about larger density and/or higher mobility of the domain walls in the back-side etched samples.

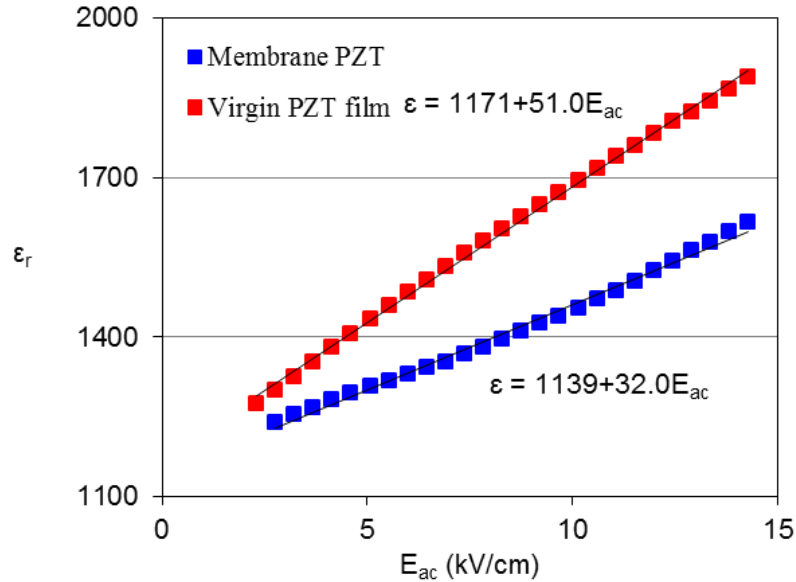

Figure 7.3 Field dependence of the real component of the dielectric permittivity for the 1 μm PZT films in virgin and released states. The slope and intercept of the fitted trend line represent the irreversible and reversible Rayleigh parameters.

7.3.2 Macroscopic Piezoelectric Response

Table 7.1 shows the piezoelectric coefficient to enhance more than an order of magnitude upon reduction of the Si substrate's thickness. $d_{33,f}$ values of 3 to 6 nm/V are superior by an order of magnitude to the best (undoped) bulk PZT ceramics. This suggests the presence of one or more mechanisms for enhancement of the electromechanical coupling with respect to the substrate-clamped thin film samples, which are either inactive or of much lower influence on the dielectric response of the films.

Figure 7.4 shows the evolution of the low field dielectric permittivity and $d_{33,f}$ piezoelectric coefficient of an 800 nm PZT film, under progressive reduction of Si substrate thickness. While a modest increase in the dielectric permittivity of the film is observed, a huge enhancement in the film's piezoelectric coefficient is measured for

residual Si thicknesses below ~100 μm. This is relatively consistent with results previously reported for back-side etched lead titanate thin films, where a modest increase in dielectric permittivity and a 4x increase in piezoelectric response were observed upon reduction of the thickness of the Si substrate.

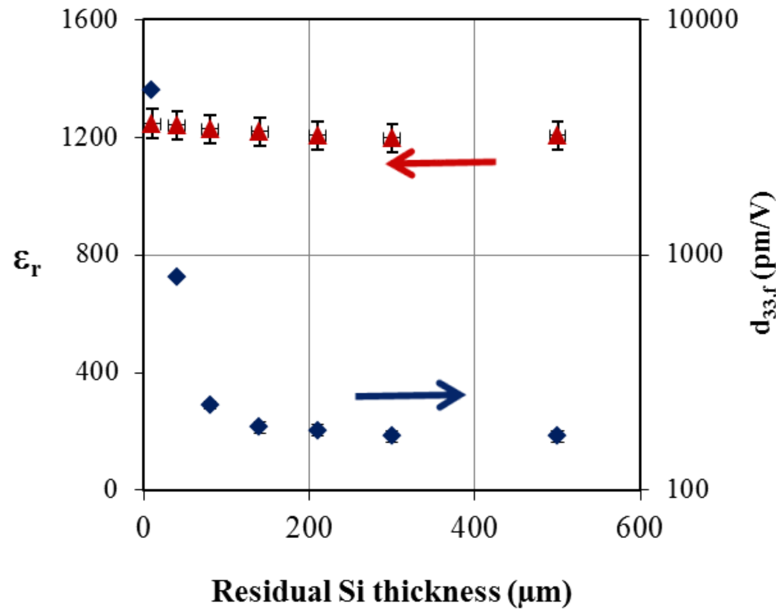

Figure 7.4 Variation of the dielectric permittivity (ε_r) and piezoelectric response $d_{33,f}$ as a function of the residual Si thickness.

Back to figure 7.2, $d_{33,f}$ as a function of the DC electric field, E_{DC}, has been compared before and after partial Si substrate removal for a 1090 nm-thick PZT film. The $d_{33,f}$ in this figure is shown after scaling of the (measured value)×0.7×0.86×0.85 due to the maximum possible measurement errors associated with the electrode size being larger than the film thickness (up to 30% overestimation)[179], potential misalignment between the two laser beams (10% to 14% error)[180] and tool laser readout error at large displacements (up to 15% error according to the tool manual). In addition to the huge enhancement of the piezoelectric response of the released film, some distinctive features in the shape of the piezoelectric loop of the released film should be noted. Specifically a

"hump", i.e. an increase in $d_{33,f}$ through a maximum with E_{DC} values decreasing from saturation, and a "nose", i.e. a self-crossing of the piezoelectric loop close to its tip, were observed.[181]

These features have been previously observed in bulk single crystals and in ceramic thin films in particular.[182,183] Tagantsev et al. used simple analytical calculations to explain such features in the piezoelectric hysteresis loop, only considering the non-ferroelastic, 180° polarization switching.[181] The same concept has been shown experimentally to be applicable to non-180° or ferroelastic polarization switching. It means that similar features - maximized piezoelectric activity at mid-range DC bias voltages, and its drastic reduction at increased bias fields – could be generated by ferroelastic domain wall motions or polarization switching.[184] In fact, hump and nose features (but less pronounced) have been also reported for the piezoelectric hysteresis loops of the laterally released PZT "islands" measured via piezoresponse force microscopy (PFM) by Nagarajan et al., while they were absent in the loops of the continuous films.[184] Hence, the pronounced appearance of the "nose" and "hump" in the piezoelectric hysteresis loop of the membrane samples and their absence in the virgin film may suggest an important role of domain switching in the enhancement of the films' piezoelectric response upon partial removal of the substrate.

The $d_{33,f}$-E_{dc} hysteresis curves were dependent on the ac field amplitude and frequency, as shown in Figure 7.5. The ac amplitude had a minor effect on the loop, but slightly decreased the remanent piezoelectric response of the membrane. This is possibly due to the earlier onset of switching of domains in the presence of a higher alternating field. Additionally, the piezoelectric response is invariant within an order of magnitude of

frequency range from 100 Hz to 1 KHz and at frequencies above 3kHz, with a large increase in the response observed at 2 kHz. The large increase in the response may be due to the presence of a resonance frequency of the membrane in proximity of the excitation at 2 kHz. Throughout this work, the reported $d_{33,f}$ curves and values are taken at frequencies far from such anomalies.

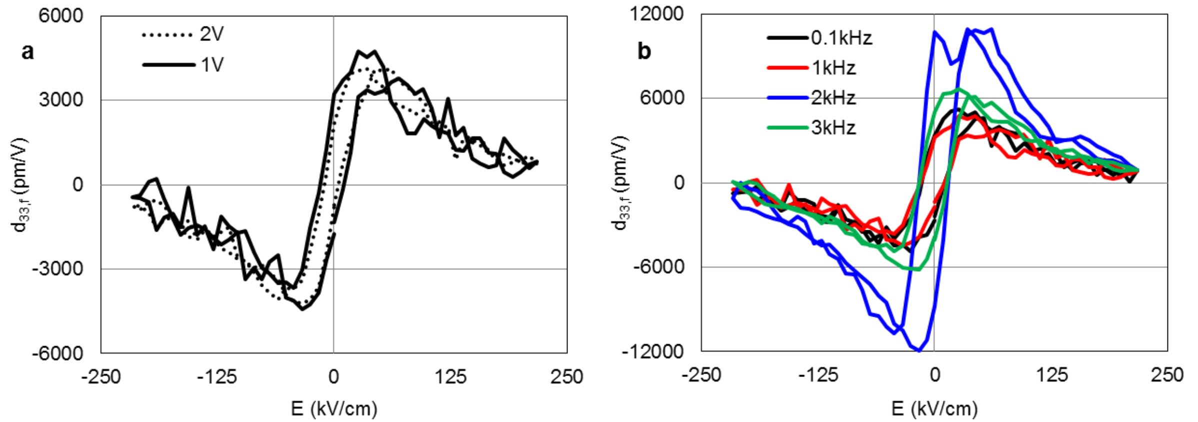

Figure 7.5 Ac field amplitude and frequency dependence of the piezoelectric response as measured via double beam laser interferometry. (a): Dependence of the $d_{33,f}$-E_{dc} hysteresis curves on the ac amplitude at 1kHz and (b): Dependence of the $d_{33,f}$-E_{dc} hysteresis curves on the frequency of the ac field at the amplitude of 1V measured on a 900 nm-thick PZT membrane.

This is an indication of presence of large number of domain walls and/or easier switching of domains in the substrate released films, which in turn contributes to the enhancement of the dielectric response of the film in this state. It is not far-fetched to imagine that the substrate mediates the switching or in general the motion of both the 180° and non-180° domain walls, and therefore that its partial removal eases their motion and in turn polarization switching. However, strong enhancement of the piezoelectric response seems to suggest a pivotal role for ferroelastic domain walls and their enhanced mobility. Higher dielectric permittivity and huge piezoelectric response at low bias fields

suggest that even other contributing factors to this enhancement – such as possibly flexoelectricity[5] – could be dependent on or related to the domain wall motion or switching.

7.3.3 Effects of Applied Stress on the Membrane

To better understand the role of the biaxial stresses on the dielectric properties of the PZT film, the changes in the dielectric response resulting from the inward deflection of the Si membrane, caused by the application of vacuum to the etched Si cavity (at the back of the sample), was studied. The downward deflection of the PZT membrane effectively translates into a compressive stress. Multiple challenges are associated with the analytical calculation of the new biaxial stress state: the structure is multilayered with an original residual stress state; the deflections created are large relative to the membrane thickness, resulting in nonlinear behavior; bending and stretching are coupled, and there is electromechanical coupling due to piezoelectricity and flexoelectricity. However, an estimation of the compressive stress can be made based on a static analysis, using the geometric parameters, maximum membrane deflection and mechanical properties of PZT and Si.

The maximum static deflection of an approximately 20 μm thick (97 % silicon, 0.5 μm PZT) membrane with the area of 1 cm^2 was measured to be ~200-500 μm at the center of the membrane. Based on simple linear elastic theory of a clamped membrane, the biaxial compressive strain at the center and top surface of the membrane (PZT film), is $\epsilon_{xx} = \epsilon_{yy}$ and is given by:

[5] Flexoelectricity describes an electromechanical coupling that is present in all dielectric materials when they are subjected to strain variations or electric field gradients, see section 7.3.4.

$$\epsilon_{xx} = \epsilon_{yy} = -\frac{pta^2}{32D}\ ,\ w = -\frac{pa^4}{64D},\ FR = \frac{t^3 E_{Si}}{12(1-v_{Si}^2)} \qquad \text{Equation 7.1}$$

where, *p, t, a* and *FR* are the applied differential pressure, thickness, radius, and flexural rigidity of the membrane, respectively, E_{Si} and v_{Si} are Young's modulus and Poisson's ratio of the Si, and *w* is the maximum deflection at the membrane center. In this simple approximation, the rigidity of the PZT film has been neglected compared to that of the much thicker Si layer. The resulting biaxial compressive stress at the surface of the PZT film can be calculated based on the plane-stress state:

$$\sigma_{xx} = \sigma_{yy} = \frac{E}{1-v^2}(\epsilon_{xx} + v\epsilon_{yy}) \qquad \text{Equation 7.2}$$

where *E* =101 GPa and *v* =0.3 are Young's modulus and Poisson's ratio of the PZT.[109] This results in a maximum compressive stress of ~46 to 115 MPa (corresponding to the maximum deflection of ~200 to 500 μm), which is expected to be relatively uniform through the PZT film thickness, due to the relatively small thickness of the film with respect to the residual Si thickness. The low field dielectric response and remanent polarization of the released PZT film further increased by ~4 and 10% as a result of this external compressive stress with respect to the relaxed state. This increase is very close to the amount of the increase in the dielectric permittivity and remanent polarization associated with back-side Si etching. The calculated compressive stress is also of the same order of magnitude as the tensile in-plane residual stress reported in PZT thin films on platinized Si substrate: ~100 to 140 MPa.[67,104] Therefore, the observed enhancement in the dielectric permittivity and remanent polarization of the PZT films as a result of applied compressive stress is analogous to enhancement that is obtained as a result of back-side Si etching. Additionally, the enhancements are consistent in magnitude with

the previously reported effect of tensile/compressive biaxial stress in PZT films on the ferroelectric properties. This can suggest that the back-side etching of the Si substrate might cause relaxation of most of the tensile residual stresses in the PZT films, or at least this suggests that this result reflects similar effects on the ferroelectric properties of the film.

7.3.4 Microscopic Piezoelectric Response

To get insight into the local mechanisms responsible for giant electromechanical responses, the local electromechanical activity of the clamped and released films was investigated using band excitation piezoresponse force microscopy (BE-PFM)[6]. The domain structure of the clamped film and its evolution with applied dc bias is shown in Figure 7.6. The clamped film shows the presence of clearly visible 50 to 100nm grains. However, electromechanical activity shows the presence of large-scale clusters, as reported in many previous studies for PZT films on solid Si substrate.[111] Switching proceeds through the gradual evolution of these domain clusters.

BE-PFM scans of the evolution of the electromechanical activity of the released film are shown in Figure 7.7. Surprisingly, very clear individual grains are discernible. The piezoresponse amplitude of the membrane electrodes shows huge enhancement, more than an order of magnitude with respect to the clamped sample (at lower dc bias fields); no long-range interactions are present, and switching is happening in a grain by grain paradigm.

---

[6] BE-PFM studies were conducted by Dr. Amit Kumar at the Center for Nanophase Materials Sciences, at Oak Ridge National Laboratory, U.S. Department of Energy.

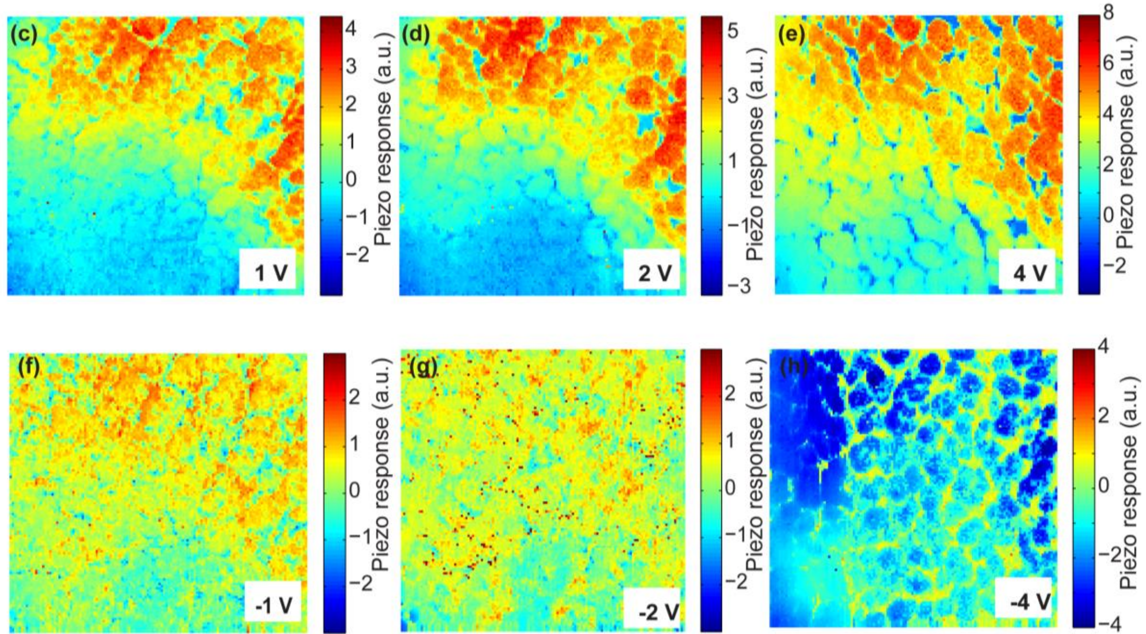

Figure 7.6 Local characterization of piezoresponse in PZT clamped capacitors when applied to the shown dc bias.[7]

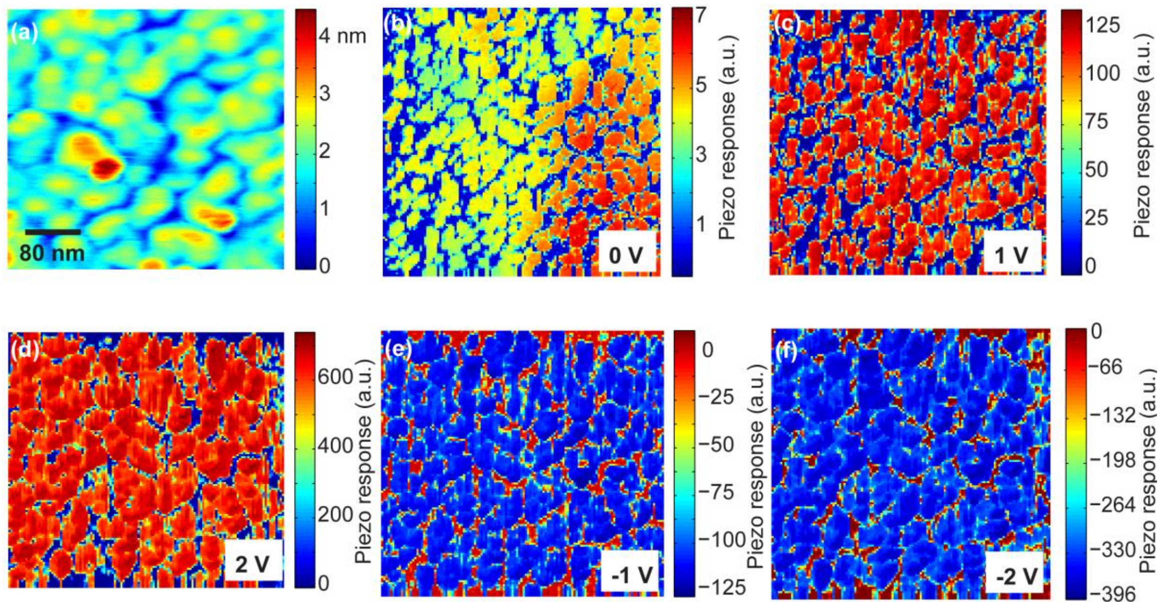

Figure 7.7 Topography and local characterization of piezoresponse in PZT membrane capacitors (on the Pt top electrode) when applied to the shown dc bias.

[7] BE-PFM studies were conducted by Dr. Amit Kumar at the Center for Nanophase Materials Sciences, at Oak Ridge National Laboratory, U.S. Department of Energy.

The combination of the dielectric and piezoelectric macroscopic measurements and PFM data indicate that long-range elastic interactions in the clamped ferroelectric films are the primary factors that limit the giant electromechanical responses, even at the MPB compositions, in such systems. However, further analysis and investigation are required to fully understand the possible origins of the giant piezoelectric response in the PZT membrane, and suppression mechanisms in clamped thin film.

In mechanically free PZT material at MPB composition, an extremely large piezoelectric response is expected due to the rhombohedral-tetragonal polarization rotation[139,185] and ferroelectric and ferroelastic domain dynamics. Here a relatively small enhancement of the dielectric response, compared to the huge enhancement in the piezoelectric response as a result of substrate removal, indicates that multiple mechanisms with different underpinning physics or effective length scales, contribute to a large extent only to the giant piezoresponse of PZT grains in membrane film configuration. Three extrinsic mechanisms can be hypothesized to contribute to such a phenomenon based on phase transition and domain dynamics. On the level of a single domain, an increased electromechanical response can be induced by flexoelectric coupling at the domain walls and by ferroelectric or ferroelastic wall motion. Flexoelectricity describes an electromechanical coupling that is present in all dielectric materials when they are subjected to strain variations or electric field gradients.[186,187] While this is negligible in most bulk materials, it can be enhanced by many orders of magnitude at sub-micron scales, especially in ferroelectric or incipient-ferroelectric materials, if boundary conditions lead to the creation of large stress or strain gradients.[187-189] Generally, a gradient in the substrate-induced residual stresses is also present in

clamped ferroelectric thin films.[112] However, removal of a big part of the substrate affects the residual stress magnitude and distribution in the film. Additionally augmented domain vibrations can generate high local stress gradients as well.

At the level of multiple domains, contributions from collective domain dynamics and domain reorientations are possible, and are expected to be strongly dependent on local mechanical boundary conditions. As illustrated in Figure 7.8, in mechanically free grains with a single family of domains, an avalanche type motion is possible, resulting in much bigger out of plane field-induced strains. In such a case, domain dynamics will be strongly suppressed by jamming and collective pinning effects in grains with more complex domain textures or strong clamping.

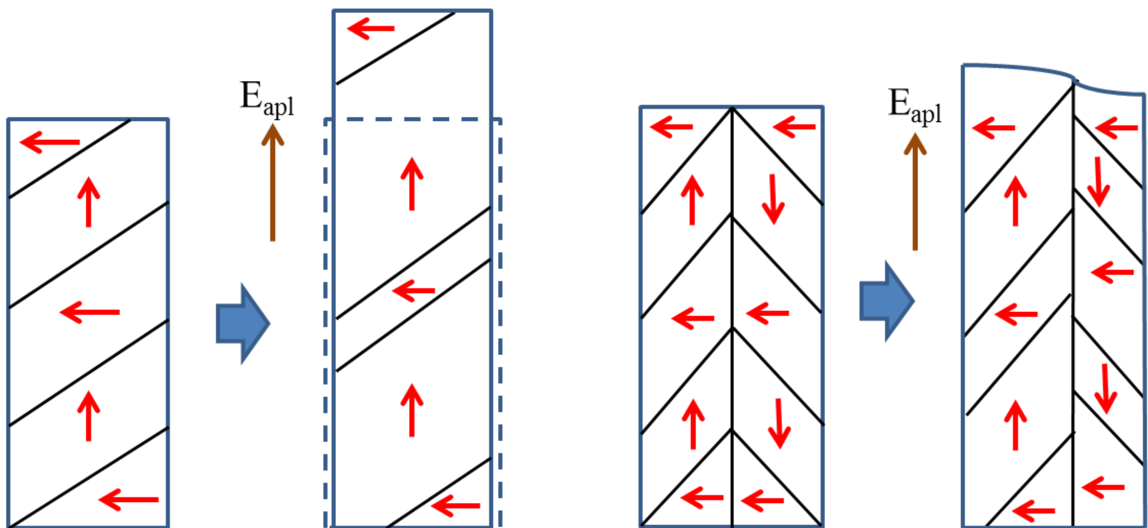

Figure 7.8 proposed avalanche mechanism in specific single domain wide grains (left) compared to jamming and suppression in comlex domain configuration (right).

Finally, the PFM observations suggest that the breakdown of electromechanical clustering of grains, observed at the micron length scale can be either an additional mechanism or a manifestation of the previous two mechanisms leading to enhancement of responses. The specific microstructure and texture of PZT films might play an

important role in generating these effects leading to the observed giant piezoelectric response.

The very high degree of texturing of the films (>95% Lotgering factor) added to the very small lateral dimensions (50-100 nm) can indeed lead to creation of specific domain patterns. Theoretical and experimental work by Khatchaturian et al.[190,191] and recent reports by Tyunina et al.[192] suggest in fact that in (coherent) crystallites of very small dimensions (≤~100nm), the domain configuration can change from a multiple population of tweed-like structures, to a single family of domains (Figure 7.8). The presence of a single family of domains is consistent with PFM observations on PZT membrane as shown in Figure 7.7. The co-presence of multiple families of domains can lead to creation of internal stresses, which would hinder the motion of domain walls in adjacent domain families. The presence of a single family of domains can conversely facilitate an avalanche motion effect, where single interface motion events translate into the motion of multiple domain walls over a much larger scale, comparable to the full length of a grain (Figure 7.8).[193] In the clamped locations, such large scale motion of the domain walls is hindered by the boundary conditions and constrained to adjacent grains, as clearly shown in the PFM response. This leads to a collaborative electromechanical activity over a larger length scale representing cluster effects shown in Figure 7.6. In the membrane samples, on the other hand, grains are allowed to respond (at least partially) decoupled from each other, and therefore a large motion of domain walls within a grain naturally results in a very large enhancement of the electromechanical coupling of each such grain. The very large enhancement of the piezoelectric response, unmatched by a similar increase in the dielectric response, further suggests that such a single family of

domains should be ferroelastic (non-180°domains), rather than simply ferroelectric (180°domains).

7.4 Results and Discussion; PMN-PT Membranes

Figure 7.9 compares $d_{33,f}$ and relative dielectric permittivity (ε_r) as a function of the DC electric field, E_{DC} for a 1μm-thick 0.7PMN-0.3PT (PMN-PT) film, before and after partial Si substrate removal. A great enhancement in the piezoelectric response accompanied by a slight increase in the dielectric response of the released capacitor with respect to the virgin one was observed. The enhancement of the piezoelectric response in released PMN-PT capacitors is not as remarkable as its PZT counterpart. The membrane electromechanical response in PMN-PT film is just comparable to the literature-reported values for PMN-PT single crystals with similar chemical composition (70/30). Additionally, unlike PZT, the distinctive "hump and nose" features are absent in the piezoelectric loops of PMN-PT membrane capacitors. This implies that some of the enhancement mechanisms in a PZT system are absent in PMN-PT. In particular, contributions from enhanced domain dynamics might not be as strong in PMN-PT systems, as they are associated with the presence of "nose and hump" features in the $d_{33,f}$ –E_{DC} loop. This is also consistent with the observations from comparing the C-V loops in PZT and PMN-PT samples. Unlike in PZT, PMN-PT membranes do not show a strong enhancement in the capacitance as a result of the substrate removal, especially at low bias fields.

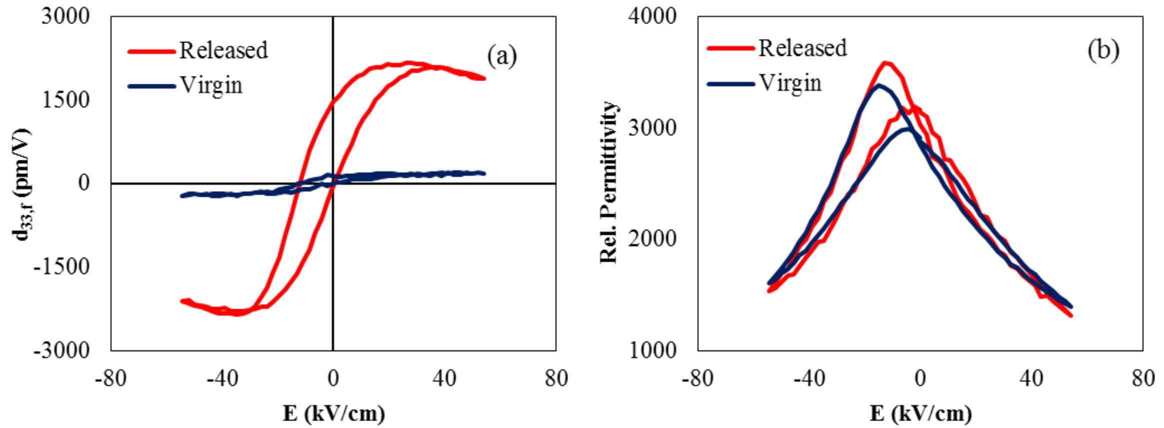

Figure 7.9. (a): $d_{33,f}$-E_{dc} hysteresis curves and (b): Capacitance-E_{dc} (C-E curve) for a 1 μm-thick 0.7PMN-0.3PT capacitor in clamped state (virgin) before Si etching, and after etch in membrane form (released). The inset in (a) shows a zoomed view of the $d_{33,f}$-E_{dc} hysteresis curve of the virgin capacitor.

7.5 Summary and Conclusions

To summarize, we observed massive enhancement in the piezoelectric response of the nano-polycrystalline, highly (100)-textured PZT films after (partial) removal of the Si substrate. This enhancement is accompanied by the breakdown of the elastic and electromechanical clustering among the grains, which is present in the substrate clamped films. Increased mobility of ferroelastic interfaces, such as domain walls and phase boundaries, as well as possible flexoelectric effects in this specific length scales can play an important role in the observed enhancement of the piezoelectric response. A remarkable enhancement in the electromechanical response of the substrate released capacitors was also observed in PMN-PT films; however, the enhancement was not as large as that of the PZT counterpart. This suggest that the effects of the residual stresses resulting from substrate clamping on the electromechanical activity of the MPB relaxor ferroelectrics is very different than that for MPB ferroelectrics. Extrinsic contributions

such as domain dynamics in relaxor ferroelectrics are not as significant as they are in some ferroelectric systems such as PZT.[61] This might manifest itself in the lower enhancement in piezoelectric response observed in PMN-PT membrane as a result of substrate removal. The experimental observations from piezoelectric and C-E loops are consistent with as well. Further investigation of the difference in the behavior of the released PZT and PMN-PT films can illustrate some fundamental differences between the ferroelectric and relaxor-ferroelectric material systems and their potential applications in piezo-MEMS applications.

A breakdown of the clustered pattern in the electromechanical activity of the grains indicates a new pathway for greatly improved properties which has a huge potential to enable high performance future device applications. The enhanced electromechanical response observed in the membranes should provide a new paradigm for creation of ultra-high sensitivity MEMS sensors, where the piezoelectric coefficient is the critical parameter determining the final device performance. Similarly, such PZT membranes should provide orders of magnitude enhancement to the power densities achievable in piezo-MEMS vibration energy harvesters, which strongly improves with the electromechanical coupling and mechanical flexibility of the piezoelectric device.

Chapter 8

CONCLUSIONS AND FUTURE WORK

This chapter briefly summarizes the major findings in this investigation. Based on the outcomes and experimental observations, some directions for future work are recommended.

8.1 Summary and Conclusions

The advent of ferroelectric thin films with strong piezoelectric response has enabled the development of new nano- and micro-electromechanical systems (NEMS/MEMS) capable of large displacements at low voltage levels, aiming to be compatible with complementary metal oxide semiconductor industry. Key to all of these applications is the ability to process ferroelectric materials with maximized electromechanical coupling and to integrate them into the devices. With the continuous drive towards miniaturization of devices for piezoelectric and electronic applications, processing of ultrathin ferroelectric films with maintained large electromechanical coupling is essential to the development of high performance NEMS and MEMS.

The piezoelectric response of ferroelectric thin films is profoundly affected by the texture and microstructural characteristics of the material and is severely reduced at sub-micron thickness ranges. For the first time, reproducible synthesis of dense, highly textured and phase-pure PZT thin films was achieved via chemical solution deposition.

The consistent processing of ferroelectric thin films resulted in the elimination of the coupling effects of crystallographic anisotropy, porosity and in general microstructural characteristics on the functional properties of the films. This enabled effective study of the key parameters influencing the electromechanical response of the ferroelectric thin films, such as crystallite size (thickness dependence), chemical heterogeneities and substrate clamping.

Reproducible synthesis of highly (100)-textured PZT ultrathin films enabled the study of the size effects on the dielectric and piezoelectric response of these films in the thicknesses ranging from 20 up to 260nm. Dielectric and piezoelectric responses of the films monotonically decreased in thinner films. For PZT films at MPB, a critical thickness, ~50nm was observed below which the extrinsic contributions to the dielectric responses of the films are heavily suppressed.

After the study and acknowledgment of the severe reduction of the piezoelectric response in ferroelectric ultrathin film, several factors affecting piezoelectric response of ferroelectric films were studied in order to maximize the response especially at low film thickness ranges: chemical homogeneity, residual stresses and substrate clamping as well as using alternative material systems; relaxor ferroelectrics. In particular, a major part of the piezoelectric (and dielectric) response of the PZT has extrinsic sources such as domain or phase boundary motion and vibrations. Special attention was paid throughout this investigation into understanding extrinsic origins in PZT thin films and different approaches was utilized to further activate and enhance their contributions.

Focusing on the chemical homogeneity of the ferroelectric films, Different routes were used to process ultrathin films (<200nm) with maintained functional properties, with a focus on the extrinsic sources of the material response. Superior piezoelectric properties - 40% higher piezoelectric response than in conventionally processed films - were achieved in highly (100)-oriented PZT superlattice-like films with controlled compositional gradient centered around MPB composition on Si substrates. Superlattice (SL) or heterolayered ferroelectric thin films consist of alternate layers of ferroelectric materials, or phases, with a compositional gradient normal to the substrate. The dynamic motion of “artificially created” phase boundaries between layer to layer tetragonal and rhombohedral phases participated in the extrinsic contributions to the films’ dielectric and piezoelectric response. This approach led to processing of 200 nm SL films with $d_{33,f}$ values as high as some of the best previously reported data for 1 to 2 μm-thick PZT films.[107,142,143]

Furthermore, comprehensive processing optimization was carried out on relaxor-ferroelectric PMN-PT thin films. Dense, highly (100)-textured PMN-PT films were synthesized exhibiting the highest $d_{33,f}$ coefficients reported so far in the literature (210pm/V) for corresponding thickness ranges. Control of the microstructural characteristics -texture and density– throughout the whole film thickness was necessary to obtain films with maximized functional properties.

To study the effect of substrate clamping on the piezoelectric performance of the films, the Si substrate in PZT and PMN-PT films were back-side etched via dry etching in an inductively coupled plasma reactor. This approach is similar the final state of the films for MEMS applications, where the Si substrate is mostly removed in order to have a

free-standing or semi-free standing ferroelectric membrane or cantilever. A giant enhancement in the piezoelectric $d_{33,f}$ coefficient of the substrate-released samples was observed with respect to the films on the virgin substrate. The response increased by at least one order of magnitude from ~75-200 pm/V (for different PZT film thicknesses ranging from 300nm to 1μm) to ~1500 to 3000 pm/V at reduced Si thickness. Experimental observations in macroscopic dielectric and piezoelectric characterization of the membrane indicate larger extrinsic contributions, -possibly with domain dynamic source- to the functional responses of the films in back-side etched samples. Further investigations based on band-excitation piezo-force microscopy revealed a change in the pattern of the electromechanical activity of the grains between the released and clamped films. A breakdown of the clustered pattern in the electromechanical activity of the grains indicates a new pathway for greatly improved properties which has a huge potential to enable high performance future device applications. The enhanced electromechanical response observed in the membranes as shown in figure 8.1 should provide a new paradigm for creation of ultra-high performance MEMS sensors and actuators.

PMN-PT films did not exhibit such a giant enhancement in their piezoelectric response as PZT films; final effective piezoelectric coefficient of ~2000 pm/V. This suggests fundamentally different sources of reduced piezoelectric response in ferroelectric versus relaxor-ferroelectric thin films.

To summarize, it was shown that extrinsic sources profoundly affect the functional properties of ferroelectric thin films and therefore can be effectively utilized via different approaches to maximize the films' piezoelectric (and dielectric) response. These sources include defect densities and microstructural characteristics, chemical

homogeneities and long range elastic interactions between the substrate and the film. Effectiveness of these approaches in maximizing the piezoelectric response of the thin and ultrathin ferroelectric films was shown.

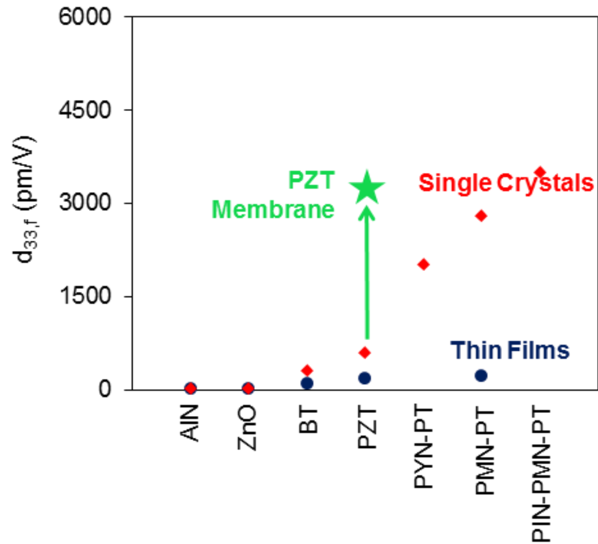

Figure 8.1 Huge enhancement of the piezoelectric response in substrate-released highly (100)-textured PZT thin films compared to the piezoelectric response of some other piezoelectric materials in thin film and single crystal form.

8.2 Future Work

The following sections discusses suggested future work for the advancement of the scientific understanding and processing optimization of ferroelectric thin film and piezo-MEMS device applications.

8.2.1 Piezo-MEMS Applications: Integration of Optimized Ferroelectric Thin Films in MEMS Transducers.

Piezoelectric microelectromechanical systems (MEMS) offer the opportunity for fabrication of sensors with high sensitivity and actuators with large displacement and low-voltage requirements. Most piezoelectric MEMS devices are based on flexural structures, which exploit piezoelectric stress generated in the film plane through either the 31 mode (transverse coefficient $e_{31,f}$) by using top and bottom electrodes, or the 33 mode (longitudinal coefficient $d_{33,f}$) for films with interdigitated electrodes (Figure 8.2).[174]

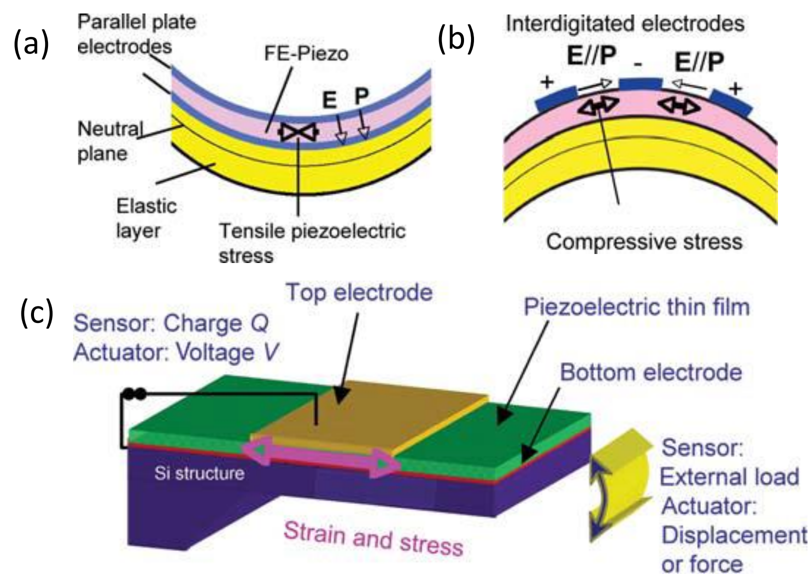

Figure 8.2 Schematic drawing of generic structures in bending actuators or sensors: (a) and (b) show bending actuation for parallel-plate and interdigitated electrodes, respectively; (c) visualize actuator and sensor modes for cantilevers and bridges, respectively. FE, ferroelectric; E, electric field; P, polarization.[174]

In particular, recent Advances in the deposition of high-piezoelectric response, ferroelectric thin films point towards a generation of MEMS devices capable of large displacements at voltages compatible with complementary metal oxide semiconductors. Piezoelectric materials that are not ferroelectrically active, such as ZnO and AlN, have

also been used for MEMS applications. However, their low piezoelectric coefficient limits their use for high displacement actuators (Table 1.1).

The key characteristic for enabling high performance device applications is the use of materials with large piezoelectric coefficients that are retained after the microfabrication processes. For example, a flexural bending structure based on piezoelectric thin films can be used as a force or displacement sensor. A larger piezoelectric coefficient will result in increased sensitivity of the sensor at the same displacement, or application of the same level of stress will result in a larger charge development. Likewise, for actuators made with the same geometrical definition, higher piezoelectric coefficients result in larger displacement excursions under the same applied electric fields. Alternatively, with higher piezoelectric response, the same displacements can be obtained at much lower applied voltages or smaller piezoelectric film thickness.

The huge enhancement in the electromechanical coupling of the PZT thin films, and also the ability to process PZT ultrathin films with retained strong piezoelectric response achieved in this work can be used in specific applications where this strong response provides a critical advantage. Examples include integration of the optimized PZT films into energy harvesters, mass detection resonators with ultra-high sensitivity and active AFM tips for fast and effective metrology of biological samples.

The PZT membranes fabricated via the back-side etching of the Si substrate in this work showed that the piezoelectric response of the ferroelectric thin film is not only retained, but also drastically enhances as a result of the substrate removal. Energy harvester devices can be fabricated using such PZT membranes. Energy harvesters are

MEMS devices that are aimed to be used to produce electrical energy when mounted in mechanically “noisy” environments. This electrical energy can be stored and used to power electronic devices with low power requirements. Higher piezoelectric response in the PZT film integrated in them reflects into higher power generation capacity, which is the key performance parameter for this application. Therefore, Huge piezoelectric response in PZT membranes (chapter 7) enables harvesting of considerably higher amount of energy, suitable for practical applications.

Superlattice-like PZT films with maintained strong piezoelectric response at small thicknesses as presented in chapter 5, are very good candidates for use in the latter type of the applications. An example could be high sensitivity mass detection resonator sensors. Lower mass of the piezoelectrically-active resonating cantilever along with a large quality factor facilitates a detectable change in the resonating frequency of the device as a result of the smallest change in its mass.

Ultrathin PZT films with strong piezoelectric response can also be used in active AFM tips for fast and effective metrology of biological samples. Having an active tip with a large displacement range enabled by the PZT ultrathin film can enhance the scanning speed of this characterization method, while simultaneously keeping the tip light and soft enough not to damage the sensitive biological sample.

8.2.2 Supperlattice-like Thin Films; Study of the Effects of Film Thickness and Stacking Periodicity

As discussed in Chapter 5, control of the cation gradients through the film thickness can strongly affect the final properties of solid solution ferroelectric thin films.

In PZT, especially at MPB composition, small deviations from the nominal composition can lead to phase change between the rhombohedral and tetragonal crystal structures. Careful control of processing conditions results in a coherent crystal structure, which, in turn, results in coherent interlayer stresses between artificially created alternating phases.

However, big deviations from the MPB drop the functional properties, as these properties are very anisotropic and peak at MPB composition, and excessive interlayer stresses might have adverse effects as well. A comprehensive study could specify the optimized stacking periodicity and the extent of the chemical variations to maximize the piezoelectric and dielectric response of ultrathin films. Additionally, further investigation is required to determine the effectiveness of such processing route at higher film thickness ranges.

The superlattice-like structures shown in this work can be leveraged to enhance the piezoelectric and dielectric response of any solid-solution with polymorphic phase boundary, such as present in many lead-free ferroelectric thin films, especially at lower thicknesses. Pb-free ferroelectrics are attractive piezoelectric material systems due to the environmental concerns, however their weak electromechanical coupling compared to Pb-based counterparts limits their applications. With the continuous drive towards miniaturization of devices for piezoelectric and electronic applications, the use of such superlattices might become increasingly relevant for significant performance enhancement through additional extrinsic contributions in such compositions.

8.2.3 Study of the Effects of Substrate Clamping on Relaxor-Ferroelectric Thin films

As discussed in Chapter 7, an enhancement in the electromechanical response of the substrate released capacitors was observed in PMN-PT films; however, the enhancement was not as large as that of the PZT counterparts. Unlike PZT, The electromechanical response of the PMN-PT membranes is just comparable to the literature-reported values for PMN-PT single crystals with similar chemical composition (70/30). Additionally, some of the experimental observations, indicating a drastic enhancement in the extrinsic contributions were evident for PZT membranes, and absent in the PMN-PT ones. This implies that substrate-induced long range elastic interactions affect the ferroelectrics very differently than the relaxor ferroelectrics. In the other words, some of the enhancement mechanisms in the PZT membranes as a result of substrate removal are absent in PMN-PT.

Further investigation of the difference in the behavior of the released PZT and PMN-PT films can illustrate some fundamental differences between the ferroelectric and relaxor-ferroelectric material systems and their potential applications in piezo-MEMS applications. Band excitation piezoresponse force microscopy can be utilized to study the local electromechanical activity of the grains and the domain dynamics associated with it. Additionally study of the field dependence of the dielectric and piezoelectric response of the PMN-PT films in virgin and released states can shed some light on the sources of the present enhancement of the piezoelectric response in membrane samples.

References:

[1] S. Trolier-McKinstry and P. Muralt, Journal of Electroceramics **12,** 7 (2004).

[2] M. J. Madou, *Fundamentals of microfabrication : the science of miniaturization*, 2nd ed. ed. (CRC Press, Boca Raton :, 2002).

[3] D. Damjanovic, Reports on Progress in Physics **61,** 1267 (1998).

[4] ANSI/IEEE Std 180-1986**,** 0_1 (1986).

[5] M. E. Lines, *Principles and applications of ferroelectrics and related materials* (Clarendon Press, Oxford [Eng.] :, 1977).

[6] J. F. Nye, *Physical properties of crystals : their representation by tensors and matrices* (Clarendon Press, Oxford :, 1979).

[7] G. Bertotti and I. D. Mayergoyz, *The Science of Hysteresis* (Academic Press, 2005).

[8] D. V. Taylor and D. Damjanovic, Applied Physics Letters **76,** 1615 (2000).

[9] N. Bassiri-Gharb, I. Fujii, E. Hong, S. Trolier-McKinstry, D. V. Taylor, and D. Damjanovic, Journal of Electroceramics **19,** 47 (2007).

[10] N. Bassiri-Gharb, (10-27-2005).

[11] S. Trolier-McKinstry, N. B. Gharb, and D. Damjanovic, Applied Physics Letters **88,** 202901 (2006).

[12] L. Rayleigh, Philosophy Magazine **23** (1887).

[13] D. Damjanovic and M. Demartin, Journal of Physics D-Applied Physics **29,** 2057 (1996).

[14] N. Bassiri-Gharb, Thesis, The Pennsylvania State University, 2005.

[15] P. Muralt, Journal of the American Ceramic Society **91,** 1385 (2008).

[16] S. A. Wilson, R. P. J. Jourdain, Q. Zhang, R. A. Dorey, C. R. Bowen, M. Willander, Q. U. Wahab, M. A. H. Safaa, O. Nur, E. Quandt, C. Johansson, E. Pagounis, M. Kohl, J. Matovic, B. Samel, W. van der Wijngaart, E. W. H. Jager, D. Carlsson, Z. Djinovic, M. Wegener, C. Moldovan, R. Iosub, E. Abad, M. Wendlandt, C. Rusu, and K. Persson, Materials Science & Engineering R-Reports **56,** 1 (2007).

[17] B. Noheda, J. A. Gonzalo, L. E. Cross, R. Guo, S. E. Park, D. E. Cox, and G. Shirane, Physical Review B **61,** 8687 (2000).

[18] A. Bernal, Thesis, Georgia Institute of Technology, 2011.

[19] A. Bernal and N. Bassiri-Gharb, Journal of Applied Physics **112,** 052012 (2012).

[20] A. Pramanick, D. Damjanovic, J. E. Daniels, J. C. Nino, and J. L. Jones, Journal of the American Ceramic Society **94,** 293 (2011).

[21] M. J. Haun, E. Furman, S. J. Jang, and L. E. Cross, Ferroelectrics **99,** 13 (1989).

[22] S.-E. Park and T. R. Shrout, Journal of Applied Physics **82,** 1804 (1997).

[23] B. Noheda, D. E. Cox, G. Shirane, R. Guo, B. Jones, and L. E. Cross, Physical Review B **63** (2001).

[24] M. Alguero, M. Stewart, M. G. Cain, P. Ramos, J. Ricote, and M. L. Calzada, Journal of Physics D-Applied Physics **43** (2010).

[25] N. B. Gharb and S. Trolier-McKinstry, Journal of Applied Physics **97,** 064106 (2005).

[26] Y. Bastani, T. Schmitz-Kempen, A. Roelofs, and N. Bassiri-Gharb, Journal of Applied Physics **109,** 014115 (2011).

[27] R. A. Wolf and S. Trolier-McKinstry, Journal of Applied Physics **95,** 1397 (2004).

[28] F. Griggio and S. Trolier-McKinstry, Journal of Applied Physics **107,** 024105 (2010).

[29] T. Horikawa, N. Mikami, T. Makita, J. Tanimura, M. Kataoka, K. Sato, and M. Nunoshita, Japanese Journal of Applied Physics Part 1-Regular Papers Short Notes & Review Papers **32,** 4126 (1993).

[30] L. P. Wang, Thesis, Pennsylvania State University, 2001.

[31] R. A. Assink and R. W. Schwartz, Chemistry of Materials **5,** 511 (1993).

[32] Y. Bastani, A. Bernal, and N. Bassiri-Gharb, Chemical Society Reviews **In Press** (2013).

[33] J. H. Park, F. Xu, and S. Trolier-McKinstry, Journal of Applied Physics **89,** 568 (2001).

[34] S. Didari, Z. Y. Ahmad, J. D. Veldhorst, and T. A. Harris, Journal of Coatings Technology and Research**,** 1 (2013).

[35] K. L. Bhamidipati, S. Didari, and T. A. Harris, Journal of Power Sources (2013).

[36] Y. Bastani and N. Bassiri-Gharb, Acta Materialia **60,** 1346 (2012).

[37] Y. Bastani, A. Y. Cortes-Pena, A. D. Wilson, S. Gerardin, M. Bagatin, A. Paccagnella, and N. Bassiri-Gharb, Applied Physics Letters **102,** 192906 (2013).

[38] F. K. Lotgering, Journal of Inorganic & Nuclear Chemistry **9,** 113 (1959).

[39] K. H. Brosnan, Thesis, The Pennsylvania State University, 2007.

[40] Z. Zhao, V. Buscaglia, M. Viviani, M. T. Buscaglia, L. Mitoseriu, A. Testino, M. Nygren, M. Johnsson, and P. Nanni, Physical Review B **70,** 024107 (2004).

[41] P. Gerber, A. Roelofs, O. Lohse, and R. Waser, edited by R. Waser (2013).

[42] P. Gerber, A. Roelofs, O. Lohse, C. Kugeler, S. Tiedke, U. Bottger, and R. Waser, Review of Scientific Instruments **74,** 2613 (2003).

[43] A. Roelofs and R. Waser, edited by R. Waser (2013).

[44] S. Jesse, S. V. Kalinin, R. Proksch, A. P. Baddorf, and B. J. Rodriguez, Nanotechnology **18** (2007).

[45] G. Findler and H. Muenzel, (Google Patents, 1991).

[46] R. Abdolvand and F. Ayazi, Sensors and Actuators A: Physical **144,** 109 (2008).

[47] L. W. Martin, Y. H. Chu, and R. Ramesh, Materials Science and Engineering: R: Reports **68,** 89 (2010).

[48] R. H. T. Wilke, R. L. Johnson-Wilke, V. Cotroneo, W. N. Davis, P. B. Reid, D. A. Schwartz, and S. Trolier-McKinstry, Appl. Opt. **52,** 3412 (2013).

[49] G. L. Brennecka, J. F. Ihlefeld, J.-P. Maria, B. A. Tuttle, and P. G. Clem, Journal of the American Ceramic Society **93,** 3935 (2010).

[50] K.-H. Xue, C. A. P. d. Araujo, and J. Celinska, Journal of Applied Physics **107,** 104123 (2010).

[51] R. W. Schwartz, T. Schneller, and R. Waser, Comptes Rendus Chimie **7,** 433 (2004).

[52] G. L. Brennecka and B. A. Tuttle, Journal of Materials Research **22,** 2868 (2007).

[53] M. D. Losego, J. F. Ihlefeld, and J.-P. Maria, Chemistry of Materials **20,** 303 (2007).

[54] J. H. Kim and F. F. Lange, Journal of Materials Research **14,** 1626 (1999).

[55] G. L. Brennecka, W. Huebner, B. A. Tuttle, and P. G. Clem, Journal of the American Ceramic Society **87,** 1459 (2004).

[56] Y. Chen and P. C. McIntyre, Applied Physics Letters **91,** 232906 (2007).

[57] I. Stolichnov, A. Tagantsev, N. Setter, J. S. Cross, and M. Tsukada, Applied Physics Letters **74,** 3552 (1999).

[58] R. J. Ong, D. A. Payne, and N. R. Sottos, Journal of the American Ceramic Society **88,** 2839 (2005).

[59] C. T. Shelton, P. G. Kotula, G. L. Brennecka, P. G. Lam, K. E. Meyer, J.-P. Maria, B. J. Gibbons, and J. F. Ihlefeld, Advanced Functional Materials **22,** 2295 (2012).

[60] J. F. Ihlefeld, W. J. Borland, and J. P. Maria, Advanced Functional Materials **17,** 1199 (2007).

[61] Y. Bastani and N. Bassiri-Gharb, Journal of the American Ceramic Society **95,** 1269 (2012).

[62] S. W. Mhin, C. Cozzan, J. Jones, K. Nittala, P. Wanninkhof, J. F. Ihlefeld, and G. L. Brennecka, Journal of the American Ceramic Society **In Press** (2013).

[63] K. G. Brooks, I. M. Reaney, R. Klissurska, Y. Huang, L. Bursill, and N. Setter, Journal of Materials Research **9,** 2540 (1994).

[64] K. Nittala, S. Mhin, K. M. Dunnigan, D. S. Robinson, J. F. Ihlefeld, P. G. Kotula, G. L. Brennecka, and J. L. Jones, Journal of Applied Physics **113,** 244101 (2013).

[65] M. H. Frey, Z. Xu, P. Han, and D. A. Payne, Ferroelectrics **206,** 337 (1998).

[66] S. Y. Chen and I. W. Chen, Journal of the American Ceramic Society **77,** 2332 (1994).

[67] S. Yagnamurthy, I. Chasiotis, J. Lambros, R. G. Polcawich, J. S. Pulskamp, and M. Dubey, Microelectromechanical Systems, Journal of **20,** 1250 (2011).

[68] F. Calame and P. Muralt, Applied Physics Letters **90,** 62907 (2007).

[69] B. Malic, I. Arcon, A. Kodre, and M. Kosec, Journal of Applied Physics **100,** 051612 (2006).

[70] P. Muralt, R. G. Polcawich, and S. Trolier-McKinstry, Mrs Bulletin **34,** 658 (2009).

[71] T. M. Shaw, S. Trolier-McKinstry, and P. C. McIntyre, Annual Review of Materials Science **30,** 263 (2000).

[72] Y. Takeshima, K. Tanaka, and Y. Sakabe, Japanese Journal of Applied Physics Part 1-Regular Papers Short Notes & Review Papers **39,** 5389 (2000).

[73] W. J. Lee, H. G. Kim, and S. G. Yoon, Journal of Applied Physics **80,** 5891 (1996).

[74] M. C. Werner, I. Banerjee, P. C. McIntyre, N. Tani, and M. Tanimura, Applied Physics Letters **77,** 1209 (2000).

[75] J. Q. He, E. Vasco, C. L. Jia, and R. H. Wang, Applied Physics Letters **87,** 062901 (2005).

[76] J. McAneney, L. J. Sinnamon, R. M. Bowman, and J. M. Gregg, Journal of Applied Physics **94,** 4566 (2003).

[77] C. Zhou and D. M. Newns, Journal of Applied Physics **82,** 3081 (1997).

[78] C. B. Parker, J. P. Maria, and A. I. Kingon, Applied Physics Letters **81,** 340 (2002).

[79] A. Lookman, R. M. Bowman, J. M. Gregg, J. Kut, S. Rios, M. Dawber, A. Ruediger, and J. F. Scott, Journal of Applied Physics **96,** 555 (2004).

[80] W. Y. Park and C. S. Hwang, Applied Physics Letters **85,** 5313 (2004).

[81] R. Waser, Integrated Ferroelectrics **15,** 39 (1997).

[82] S. K. Streiffer, C. Basceri, C. B. Parker, S. E. Lash, and A. I. Kingon, Journal of Applied Physics **86,** 4565 (1999).

[83] Partially due to spontaneous strain developed at the transition temperature, and partially due to crystallization at higher than room temperature and subsequent cooling of the ferroelectric material that has mismatched thermal expansion coefficient with the substrate

[84] S. Rios, J. F. Scott, A. Lookman, J. McAneney, R. M. Bowman, and J. M. Gregg, Journal of Applied Physics **99,** 024107 (2006).

[85] Z. G. Ban and S. P. Alpay, Journal of Applied Physics **93,** 504 (2003).

[86] H. Li, A. L. Roytburd, S. P. Alpay, T. D. Tran, L. Salamanca-Riba, and R. Ramesh, Applied Physics Letters **78,** 2354 (2001).

[87] H. Fujisawa, M. Shimizu, T. Horiuchi, T. Shiosaki, and K. Matsushige, Japanese Journal of Applied Physics Part 1-Regular Papers Short Notes & Review Papers **35,** 4913 (1996).

[88] G. F. Huang and S. Berger, Journal of Applied Physics **93,** 2855 (2003).

[89] T. M. Doan, L. Lu, and M. O. Lai, Journal of Physics D-Applied Physics **43,** 035402 (2010).

[90] D. D. Fong, G. B. Stephenson, S. K. Streiffer, J. A. Eastman, O. Auciello, P. H. Fuoss, and C. Thompson, Science **304,** 1650 (2004).

[91] L. W. Chang, M. Alexe, J. F. Scott, and J. M. Gregg, Advanced Materials **21,** 4911 (2009).

[92] C. A. Mead, Physical Review Letters **6,** 545 (1961).

[93] M. M. Saad, P. Baxter, J. McAneney, A. Lookman, L. J. Sinnamon, P. Evans, A. Schilling, T. Adams, X. H. Zhu, R. J. Pollard, R. M. Bowman, J. M. Gregg, D. J. Jung, F. D. Morrison, and J. F. Scott, Ieee Transactions on Ultrasonics Ferroelectrics and Frequency Control **53,** 2208 (2006).

[94] X. J. Lou and J. Wang, Journal of Physics-Condensed Matter **22,** 055901 (2010).

[95] M. Stengel and N. A. Spaldin, Nature **443,** 679 (2006).

[96] W. W. Cao and C. A. Randall, Journal of Physics and Chemistry of Solids **57,** 1499 (1996).

[97] G. Arlt, Journal of Materials Science **25,** 2655 (1990).

[98] L. D. Madsen, E. M. Griswold, and L. Weaver, Journal of Materials Research **12,** 2612 (1997).

[99] V. Nagarajan, I. G. Jenkins, S. P. Alpay, H. Li, S. Aggarwal, L. Salamanca-Riba, A. L. Roytburd, and R. Ramesh, Journal of Applied Physics **86,** 595 (1999).

[100] D. V. Taylor and D. Damjanovic, Applied Physics Letters **73,** 2045 (1998).

[101] S. Kalpat and K. Uchino, Journal of Applied Physics **90,** 2703 (2001).

[102] S. A. Impey, Z. Huang, A. Patel, R. Beanland, N. M. Shorrocks, R. Watton, and R. W. Whatmore, Journal of Applied Physics **83,** 2202 (1998).

[103] G. L. Brennecka, C. M. Parish, J. Jones, B. A. Tuttle, J. S. Wheeler, and J. G. Ekerdt, in *14th US-Japan Seminar on Dielectric and Piezoelectric Materials* (Portland, OR, 2009), p. 136.

[104] J. F. Shepard, Trolier-McKinstry, S., Hendrickson, M., Zeto, R., in *The Effects of Biaxial Stress on the Ferroelectric Characteristics of PZT Thin Films*, 1997, p. 47.

[105] R. Bouregba, G. Le Rhun, G. Poullain, and G. Leclerc, Journal of Applied Physics **99,** 034102 (2006).

[106] P. Muralt, A. Kholkin, M. Kohli, and T. Maeder, Sensors and Actuators a-Physical **53,** 398 (1996).

[107] F. Xu, S. Trolier-McKinstry, W. Ren, B. M. Xu, Z. L. Xie, and K. J. Hemker, Journal of Applied Physics **89,** 1336 (2001).

[108] W. H. Xu, D. X. Lu, and T. Y. Zhang, Applied Physics Letters **79,** 4112 (2001).

[109] E. Hong, R. Smith, S. V. Krishnaswamy, C. B. Freidhoff, and S. Trolier-McKinstry, Thin Solid Films **510,** 213 (2006).

[110] B. T. Lee and C. S. Hwang, Applied Physics Letters **77,** 124 (2000).

[111] P. Bintachitt, S. Jesse, D. Damjanovic, Y. Han, I. M. Reaney, S. Trolier-McKinstry, and S. V. Kalinin, Proceedings of the National Academy of Sciences of the United States of America **107,** 7219 (2010).

[112] G. Catalan, B. Noheda, J. McAneney, L. J. Sinnamon, and J. M. Gregg, Physical Review B **72,** 020102 (2005).

[113] H. J. Kim, S. H. Oh, and H. M. Jang, Applied Physics Letters **75,** 3195 (1999).

[114] S. K. Streiffer and D. D. Fong, Mrs Bulletin **34,** 832 (2009).

[115] N. B. Gharb, S. Trolier-McKinstry, and D. Damjanovic, Journal of Applied Physics **100,** 044107 (2006).

[116] I. A. Kornev and L. Bellaiche, Physical Review Letters **91,** 116103 (2003).

[117] T. Choi and J. Lee, Thin Solid Films **475,** 283 (2005).

[118] F. M. Pontes, E. Longo, E. R. Leite, and J. A. Varela, Applied Physics Letters **84,** 5470 (2004).

[119] E. Bousquet, M. Dawber, N. Stucki, C. Lichtensteiger, P. Hermet, S. Gariglio, J.-M. Triscone, and P. Ghosez, Nature **452,** 732 (2008).

[120] Y. Shimada, K. Hirakawa, and S.-W. Lee, Applied Physics Letters **81,** 1642 (2002).

[121] J. Hiltunen, D. Seneviratne, R. Sun, M. Stolfi, H. L. Tuller, J. Lappalainen, and V. Lantto, Applied Physics Letters **89,** 242904 (2006).

[122] N. D. Sharma, C. M. Landis, and P. Sharma, Journal of Applied Physics **108,** 024304 (2010).

[123] M. Dawber, N. Stucki, C. Lichtensteiger, S. Gariglio, P. Ghosez, and J. M. Triscone, Advanced Materials **19,** 4153 (2007).

[124] N. Huang, Z. Liu, Z. Wu, J. Wu, W. Duan, B.-L. Gu, and X.-W. Zhang, Physical Review Letters **91,** 067602 (2003).

[125] D. Bao, R. Scholz, M. Alexe, and D. Hesse, Journal of Applied Physics **101,** 054118 (2007).

[126] I. Kanno, S. Hayashi, R. Takayama, and T. Hirao, Applied Physics Letters **68,** 328 (1996).

[127] I. Vrejoiu, Y. Zhu, G. L. Rhun, M. A. Schubert, D. Hesse, and M. Alexe, Applied Physics Letters **90,** 072909 (2007).

[128] J. H. Jang and K. H. Yoon, Applied Physics Letters **75,** 130 (1999).

[129] N. Ledermann, P. Muralt, J. Baborowski, S. Gentil, K. Mukati, M. Cantoni, A. Seifert, and N. Setter, Sensors and Actuators A: Physical **105,** 162 (2003).

[130] G. L. Brennecka, C. M. Parish, B. A. Tuttle, L. N. Brewer, and M. A. Rodriguez, Advanced Materials **20,** 1407 (2008).

[131] ICDD PDF card number 01-070-4264.

[132] I. K. Schuller, Physical Review Letters **44,** 1597 (1980).

[133] S. Habouti, A. Lahmar, M. Dietze, C.-H. Solterbeck, V. Zaporojtchenko, and M. Es-Souni, Acta Materialia **57,** 2328 (2009).

[134] ICDD PDF card number 01-073-8128.

[135] ICDD PDF card number 01-073-2022.

[136] J. F. Shepard, Trolier-McKinstry, S., Hendrickson, M., Zeto, R., 1997, p. 47.

[137] C. Wang, Q. F. Fang, Z. G. Zhu, A. Q. Jiang, S. Y. Wang, B. L. Cheng, and Z. H. Chen, Applied Physics Letters **82,** 2880 (2003).

[138] B. Noheda, D. E. Cox, G. Shirane, R. Guo, B. Jones, and L. E. Cross, Physical Review B **63,** 014103 (2000).

[139] H. Fu and R. E. Cohen, Nature **403,** 281 (2000).

[140] A. Pramanick, D. Damjanovic, J. C. Nino, and J. L. Jones, Journal of the American Ceramic Society **92,** 2291 (2009).

[141] F. Xu, Thesis, Pennsylvania state university, 1999.

[142] S.-H. Kim, Yang, J-S, Koo, C. Y, Yeom, J-H, Yoon, E, Hwang, C. S, Park, J-S, kang, S-G, Kim, D-J, Ha J, Japanese Journal of Applied Physics **42,** 5952 (2003).

[143] D. V. Taylor and D. Damjanovic, Applied Physics Letters **76,** 1615 (2000).

[144] F. Calame, Thesis, Ecole polytechnique federale de lusanne, 2007.

[145] F. Xu, S. Trolier-McKinstry, W. Ren, B. Xu, Z.-L. Xie, and K. J. Hemker, Journal of Applied Physics **89,** 1336 (2001).

[146] S. Trolier-McKinstry, N. B. Gharb, and D. Damjanovic, Applied Physics Letters **88,** 202901 (2006).

[147] This study has been conducted at Oak Ridge National Laboratories, by Ms. Talia Field and in collaboration with Drs. Abhijit Pramanick and Valeria Lauter.

[148] S. Kwon, E. M. Sabolsky, G. L. Messing, and S. Trolier-McKinstry, Journal of the American Ceramic Society **88,** 312 (2005).

[149] J.-P. Maria, W. Hackenberger, and S. Trolier-McKinstry, Journal of Applied Physics **84,** 5147 (1998).

[150] Z. Kighelman, D. Damjanovic, and N. Setter, Journal of Applied Physics **90,** 4682 (2001).

[151] The FWHM of the Pt-(111) peak is 0.17°±0.02°

[152] PDF card number 01-076-9082

[153] J. L. Zhu, X. H. Zhu, M. Jiang, X. H. Li, J. G. Zhu, and D. Q. Xiao, Journal of Applied Physics **104** (2008).

[154] P. Muralt, Journal of Micromechanics and Microengineering **10,** 136 (2000).

[155] K. Aoki, Y. Fukuda, K. Kumata, and A. Nishimura, Japanese Journal of Applied Physics **34,** 192 (1995).

[156] G. J. Willems, D. J. Wouters, H. E. Maes, and R. Nouwen, Integrated Ferroelectrics **15,** 19 (1997).

[157] J. H. Park and S. Trolier-McKinstry, Journal of Materials Research **16,** 268 (2001).

[158] Z. Zhao, V. Buscaglia, M. Viviani, M. T. Buscaglia, L. Mitoseriu, A. Testino, M. Nygren, M. Johnsson, and P. Nanni, Physical Review B **70,** 024107 (2004).

[159] J. H. Park, D. H. Kang, and K. H. Yoon, Journal of the American Ceramic Society **82,** 2116 (1999).

[160] Y. Liu and P. P. Phulé, Journal of the American Ceramic Society **79,** 495 (1996).

[161] Z. X. T. Tani, and D. A. Payne, , in *Preferred Orientations for Sol-Gel-Derived PLZT Thin Layers*, 1993, p. 269.

[162] W. D. Kingery, H. K. Bowen, and D. R. Uhlmann, *Introduction to Ceramics* (John Wiley & Sons, New York, 1976).

[163] X. Zhao, B. Fang, H. Cao, Y. Guo, and H. Luo, Materials Science and Engineering B **96,** 254 (2002).

[164] A. J. Moulson and J. M. Herbert, *Electroceramics* (Chapman & Hall, London, 1990).

[165] R. E. Newnham, J. F. Fernandez, K. A. Markowski, J. T. Fielding, A. Dogan, and J. Wallis, in *Composite Piezoelectric Sensors and Actuators*, 1995 (Materials Research Society), p. 33.

[166] PDF Card no.01-070-9456 & 00-003-0721

[167] L. Bellaiche and D. Vanderbilt, Physical Review Letters **83,** 1347 (1999).

[168] S. Aggarwal, A. M. Dhote, R. Ramesh, W. L. Warren, G. E. Pike, D. Dimos, M. V. Raymond, B. A. Tuttle, and J. J. T. Evans, Applied Physics Letters **69,** 2540 (1996).

[169] F. Chen, X. Tan, Z. Huang, X. Xuan, and W. Wu, Applied Physics Letters **96,** 262902 (2010).

[170] S. Sadashivan, S. Aggarwal, T. K. Song, R. Ramesh, J. T. Evans, B. A. Tuttle, W. L. Warren, and D. Dimos, *Evaluation of imprint in fully integrated (La,Sr)CoO3/Pb(Nb,Zr,Ti)O3/(La,Sr)CoO3 ferroelectric capacitors*, Vol. 83 (AIP, 1998).

[171] G. E. Pike, W. L. Warren, D. Dimos, B. A. Tuttle, R. Ramesh, J. Lee, V. G. Keramidas, and J. J. T. Evans, Applied Physics Letters **66,** 484 (1995).

[172] J. Lee, R. Ramesh, V. G. Keramidas, W. L. Warren, G. E. Pike, and J. T. Evans, *Imprint and oxygen deficiency in (Pb,La)(Zr,Ti)O3 thin?film capacitors with La?Sr?Co?O electrodes*, Vol. 66 (AIP, 1995).

[173] K. Abe, N. Yanase, T. Yasumoto, and T. Kawakubo, Journal of Applied Physics **91,** 323 (2002).

[174] P. Muralt, R. G. Polcawich, and S. Trolier-McKinstry, MRS Bulletin **34,** 658 (2009).

[175] H. Zhu, D. Chu, N. Fleck, S. Rowley, and S. Saxena, Journal of Applied Physics **105,** 061609 (2009).

[176] M. B. Kelman, P. C. McIntyre, B. C. Hendrix, S. M. Bilodeau, and J. F. Roeder, Journal of Applied Physics **93,** 9231 (2003).

[177] H. Suzuki, T. Ohno, D. Fu, and N. Sakamoto, in *14th US-Japan Seminar on Dielectric and Piezoelectric Materials* (2009), p. A9.

[178] T. Ohno, H. Suzuki, H. Masui, K. Ishikawa, and M. Fujimoto, Japanese Journal of Applied Physics **43,** 6549 (2004).

[179] P. Gerber, A. Roelofs, C. Kügeler, U. Böttger, R. Waser, and K. Prume, Journal of Applied Physics **96,** 2800 (2004).

[180] Y. Bastani, A. Kumar, S. V. Kalinin, and N. Bassiri-Gharb, Unpublished (2013).

[181] A. K. Tagantsev, P. Muralt, and J. Fouzek, MRS Proceedings **784,** C.10.6 (2004).

[182] G. Schmidt, G. Borchhardt, J. Von Cieminski, D. Grützmann, E. Purinsch, and V. Isupov, Ferroelectrics **42,** 3 (1982).

[183] J. V. Cieminski, C. Kleint, H. Beige, and R. Höche, Ferroelectrics **109,** 95 (1990).

[184] V. Nagarajan, A. Roytburd, A. Stanishevsky, S. Prasertchoung, T. Zhao, L. Chen, J. Melngailis, O. Auciello, and R. Ramesh, Nature materials **2,** 43 (2002).

[185] R. E. Cohen, Nature **441,** 941 (2006).

[186] A. Tagantsev, Physical Review B **34,** 5883 (1986).

[187] L. E. Cross, Journal of Materials Science **41,** 53 (2006).

[188] B. Chu, W. Zhu, N. Li, and L. E. Cross, Journal of Applied Physics **106,** 104109 (2009).

[189] B. Chu, W. Zhu, N. Li, and L. E. Cross, Functional Materials Letters **3,** 79 (2010).

[190] Y. M. Jin, Y. U. Wang, A. G. Khachaturyan, J. F. Li, and D. Viehland, Journal of Applied Physics **94,** 3629 (2003).

[191] J. G. A. Rossetti, A. G. Khachaturyan, G. Akcay, and Y. Ni, Journal of Applied Physics **103,** 114113 (2008).

[192] M. Tyunina, L. Yao, M. Plekh, J. Levoska, and S. van Dijken, Advanced Functional Materials (2012).

[193] P. Bintachitt, S. Jesse, D. Damjanovic, Y. Han, I. M. Reaney, S. Trolier-McKinstry, and S. V. Kalinin, Proceedings of the National Academy of Sciences **107,** 7219 (2010).